Constructal Vascularized Structures for Cooling and Mechanical Strength

by

Erdal Cetkin

Department of Mechanical Engineering
and Materials Science
Duke University

Date:_____

Approved:

_____
Adrian Bejan, Co-Supervisor

_____
Sylvie Lorente, Co-Supervisor

_____
Josiah Knight

_____
Nico Hotz

A dissertation submitted in partial fulfillment of
the requirements for the degree of Doctor
of Philosophy in the Department of
Mechanical Engineering and Materials
Science in the Graduate School
of Duke University

2013

ABSTRACT

Constructal Vascularized Structures for Cooling and Mechanical Strength

by

Erdal Cetkin

Department of Mechanical Engineering
and Materials Science
Duke University

Date:_____

Approved:

_____
Adrian Bejan, Co-Supervisor

_____
Sylvie Lorente, Co-Supervisor

_____
Josiah Knight

_____
Nico Hotz

An abstract of a dissertation submitted in partial
fulfillment of the requirements for the degree
of Doctor of Philosophy in the Department of
Mechanical Engineering and Materials
Science in the Graduate School of
Duke University

2013

Abstract

This dissertation shows how to use Constructal theory in order to design vascular structures with high cooling performance and mechanical strength. The vascular structures consist of grid, tree and hybrid (grid + tree) designs. The four chapters show how the cooling performance and mechanical strength can be increased by varying the vascular structure embedded in a plate for different models and boundary conditions. Chapter 2 shows that the fastest spreading or collecting flow (i.e. the steepest S curve) is discovered by allowing the tree architecture to morph freely. The angles between the lines of the invading tree architecture can be morphed (changed, selected) such that the overall flow proceeds along the fastest route, covering the greatest territory at any moment. Chapter 3 shows development of vascular designs that provide cooling and mechanical strength at the same time. This concept is illustrated with a circular plate vascularized with embedded channels. Chapter 4 shows how vascular design controls the cooling and mechanical performance of a solid slab heated uniformly and loaded with uniform pressure. Chapter 5 shows that a plate heated by a randomly moving beam can be cooled effectively by fluid that flows through a vasculature of channels embedded in the plate. In sum, constructal design governs the evolution of flow structures that offer flow access and mechanical strength at the same time.

To my wife, Ozlen Cetkin

Contents

List of Figures

Abbreviation

A area, m^2

C laminar flow pressure drop constant

C laminar flow resistance constant, $m^2\ s^{-1}$

C_T turbulent flow pressure drop constant

C_{ijkl} elasticity tensor, Eq. (3.15)

c_P specific heat at constant pressure, $J\ kg^{-1}\ K^{-1}$

D channel diameter, m

D_1, D_2 duct diameter, Eq. (3.2)

d diameter of main distributing (collecting) channel, m

d_1 diameter of cooling channels, m

d_m diameter of the cooling ducts, m

E elasticity modulus

f volume forces, N

H plate thickness, m

k thermal conductivity, $W\ m^{-1}\ K^{-1}$

K second order tensor, Eq. (3.19)

L duct length, m

L plate length, m

L_1 length, m, Fig. 2.2

L_d length of the main distributing (collecting) channel, m

l	length of one grid cooling channel, $l = L / 4$, m
$\dot{m}$	mass flow rate, kg s^{-1}
$\tilde{m}$	volumetric flow rate, m^3 s^{-1}
n	number of the cooling ducts
n	number of bifurcation levels
n	normal direction
n_c	number of the channels of diameter d_1
P	pressure, N m^{-2}
Pe	Peclet number
Pr	Prandtl number
q"	heat flux, W m^{-2}
q"'	heat source, W m^{-3}
R	plate radius, m, Figs. 3.1, 3.5 and 3.7
Re	Reynolds number, Ud/ν
r, r_1, r_2	the distance from the center of the plate to the pairing junctions, m
r_x, r_y, r_z	displacement, m
T	temperature, K
T_0	initial temperature, K
T_1	temperature of invading lines, K
t	time, s
u, v, w	velocity components, m s^{-1}

U mean fluid velocity in d_1 channels, m s^{-1}

V velocity of the moving beam, m s^{-1}, Ch. 5

V normal velocity, m s^{-1}, Ch. 4

V speed of invasion, m s^{-1}, Ch. 2

V volume, Ch. 3

W normal velocity of fluid enters from the inlet or leaves from the outlet, m s^{-1}

x, y, z coordinates, m

x, y coordinates, m

Greek symbols

α thermal diffusivity, m^2 s^{-1}

β branching angle

γ Poisson ratio

ΔP pressure difference

ε strain

ε_{kl} strain tensor

θ dimensionless temperature

μ dynamic viscosity, kg m^{-1} s^{-1}

ν kinematic viscosity, m^2 s^{-1}

ρ density, kg m^{-3}

σ normal stress, N m^{-2}

σ_{ij} stress tensor

τ shear stress, N m^{-2}

φ shear strain

Subscripts

avg average

b moving beam

c conduction

co consolidation

f fluid

g grid

i invasion

i rank of ducts

in end of invasion

in inlet

m cooling duct pattern

max maximum

me mean

mech mechanical

out outlet

r radial

ref reference

s	solid
st	mechanical
tot	total
x, y, z	coordinates

Superscript

~	dimensionless

Acknowledgements

First of all, I would like to thank my advisors Professors Sylvie Lorente and Adrian Bejan. They are my mentors but also my role models. Their involvement made my journey truly “constructal”, and I owe them a lot.

I also would like to thank Professors Josiah Knight and Nico Hotz for being on my committee and for their valuable involvement in this dissertation.

I would like to thank my family and especially to my wife for their support throughout this experience. They always believed in me and supported me during my graduate education.

I acknowledge the financial support from the Republic of Turkey and the Air Force Office of Scientific Research. Their support made this dissertation real.

1. Introduction

Advanced technologies require capabilities such as self-healing and self-cooling in addition to the requirements of being light, durable and robust. The literature shows that embedding vascular flow structures into a system makes them capable of self-healing and self-cooling [1-5]. This dissertation focuses on how the vascular design should be made so that in addition to cooling the structure also has strength, i.e. it facilitates the flow of stresses. The results of the search for better design under the guidance of the constructal law show how a system with advanced capabilities can be made lighter, more durable and more robust.

Constructal law is a law of physics and it uncovers the evolution of any system in time. The constructal law is [6, 7] "For a finite-size flow system to persist in time (to live), its configuration must evolve in such a way that provides greater and greater access to the currents that flow through it." This law of physics has created new research areas in different fields of science such as engineering, geophysics, biology, economics and social dynamics [7-15]. The broad application of the constructal law shows how it governs the evolution of design in both animate and inanimate systems.

Throughout this dissertation, the vascular structures are designed by using the constructal law. The systems were morphed freely (i.e., without any design restrictions or generic algorithms) to find the frames of the evolution movie of the design. Constructal law emphasizes the importance of the evolution of the design, which is routinely overlooked in thermal sciences.

2. The steepest S curve: discovering the invading tree, not assuming it

Many natural and engineered flow systems are of the spreading or collecting kind. Examples of spreading flows are the river deltas, air during inhaling, and the spreading of technology. Collecting flows are river basins, air during exhaling, mining and oil extraction (the Hubbert peak).

Spreading and collecting flows are united by two features. The first feature is their tree-shaped structure. It was shown based on the constructral law that the tree flow architecture is necessary and predictable as the design that facilitates flow access between a point and an area or volume [7, 15].

The second feature is equally prevalent but less obvious. It is the S-shaped curve of the history of how the spreading or collecting flow fills or empties its area or volume. This feature has been noted in many fields where it has been studied as local (isolated) phenomena, for example, the spreading of populations [16, 17], chemical reactions [18], technologies [19-20], TVs and radios [21], and the collecting of oil, metals and minerals from the ground [22-23]. We showed recently [24] that just like the tree architecture, the S-curve is necessary and predictable as a feature that facilitates the access to flow between discrete points and finite areas and volumes. Five examples of S-curve phenomena are shown in Fig. 2.1 [16, 22, 27, 28].

In Ref. 13, we used a convection-conduction model to demonstrate how the S-curve can be predicted analytically. This model is shown in Fig. 2.2. Lines of constant temperature invade at constant speed an isothermal conducting medium. After this first

phase of “invasion”, the heating of the medium is “consolidated” by thermal diffusion perpendicular to the invading lines.

Unlike in Ref. 26, where the invading line pattern was rigid (one straight line, or a rigid tree with T-shaped bifurcations and no more than three levels of bifurcations) in the present article the invading pattern is free to change. We use this freedom in order to discover the tree design features that underpin the steepest S-curve, i.e. the fastest spreading from point to area, and the fastest collecting from area to point. The tree architecture discovered in this manner is efficient, robust, and natural-looking.

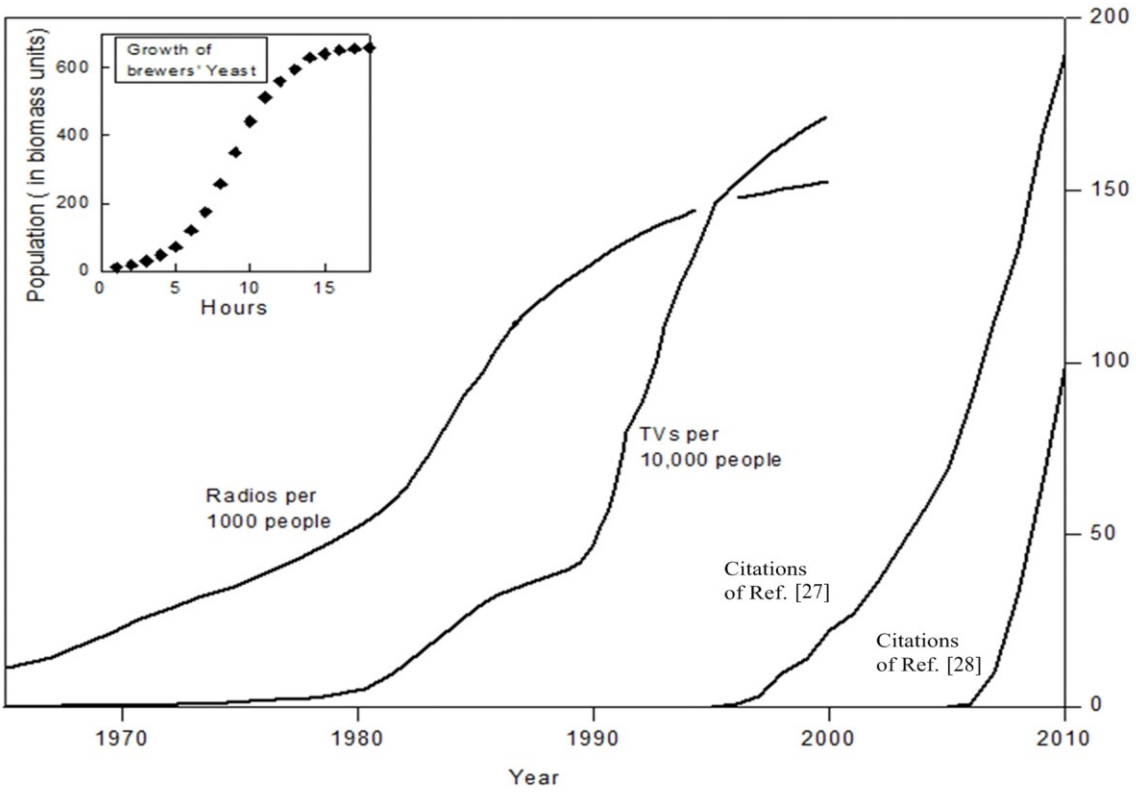

Figure 2.1: Examples of S-curve phenomena: the growth of brewers yeast (Ref. 16), the spreading of radios and TVs (Ref. 22), and the growth of the readership of scientific publications (Refs. 27 and 28).

2.1 Conduction model with a tree invading at constant speed

The two phases of the S curve phenomenon (invasion, followed by consolidation) are visualized by the thermal diffusion model presented in Fig. 2.2. The square $(2\ L_1) \times (2\ L_1)$ is a two dimensional conducting domain with uniform initial temperature (T_0), conductivity (k) and thermal diffusivity (α). The square boundary is insulated.

Beginning with the time t = 0, lines of uniform temperature (T_1) invade the conducting domain. Their tips advance with the constant speed V. Heat is transferred by

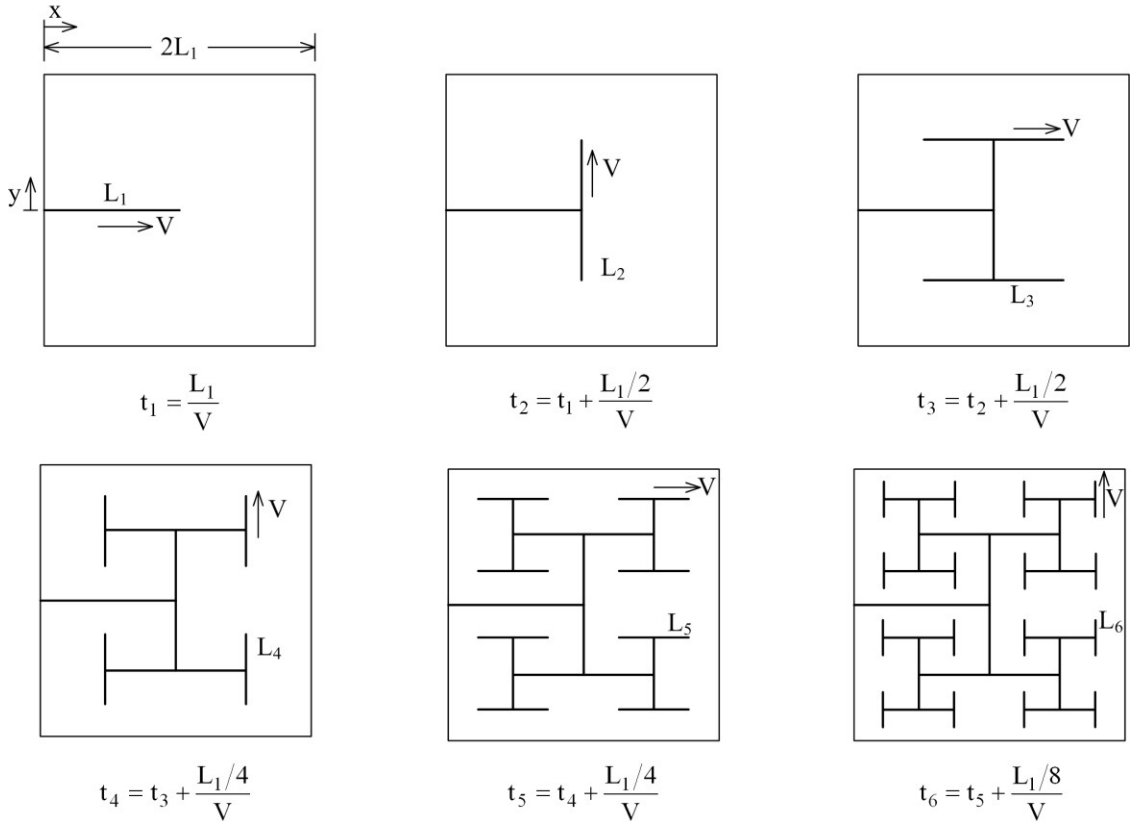

Figure 2.2: Tree-shaped line invasion of a conducting domain, with assumed T-shaped bifurcations.

thermal diffusion from the invading lines to the conducting material of temperature T(x, y, t). In time, the temperature averaged over the square area $A = 4\,L_1^2$,

$$T_{avg} = \frac{1}{A}\iint_A T\,dx\,dy \tag{2.1}$$

rises from T_0 to T_1. Of interest is the shape of the curve $T_{avg}(t)$, and how the design of the invading tree influences this shape.

In the model of Fig. 2.2 it was assumed that the tree is dichotomous with T-shaped bifurcations. The tree lines have zero thickness. Their lengths decrease in the sequence $L_1,\ L_2 = L_1/2,\ L_3 = L_2,\ L_4 = L_3/2$, etc. The times when the invading lines reach the sequential bifurcation levels are indicated as t_1, t_2, t_3, ...

The dimensionless formulation of the time-dependent heat conduction problem consists of the energy conservation equation

$$\frac{\partial\theta}{\partial\tilde{t}} = \frac{\partial^2\theta}{\partial\tilde{x}^2} + \frac{\partial^2\theta}{\partial\tilde{y}^2} \tag{2.2}$$

the boundary conditions

$$\frac{\partial\theta}{\partial\tilde{x}} = 0 \qquad \text{at} \qquad \tilde{x} = 0, 2 \tag{2.3}$$

$$\frac{\partial\theta}{\partial\tilde{y}} = 0 \qquad \text{at} \qquad \tilde{y} = \pm 1 \tag{2.4}$$

and the initial condition $\theta = 0$ at $\tilde{t} = 0$. The dimensionless variables are

$$(\tilde{x}, \tilde{y}) = (x, y)/L_1 \qquad \tilde{t} = \alpha t/L_1^2 \qquad \theta = \frac{T - T_0}{T_1 - T_0} \tag{2.5}$$

The dimensionless time-dependent heat conduction problem was solved by using a finite element software [29]. The mesh was refined after each solution, and the problem was solved again to see whether the solution is mesh dependent. This was repeated by increasing the number of mesh elements in steps of 50% until the solution changed by less than 1%.

The lone dimensionless group that characterizes this phenomenon is the ratio of the time of thermal diffusion perpendicular to the invading line (L_1^2/α) divided by the time of line invasion (L_1/V). This ratio is the Peclet number

$$\mathrm{Pe} = \frac{L_1 V}{\alpha} \tag{2.6}$$

where (unlike in convection [30]) the thermal diffusivity α belongs to the nonmoving conducting medium. Trees with larger Pe values invade the conducting body faster. This effect is illustrated in Fig. 2.3, which shows the temperature field in the square domain at the same moment $(\tilde{t} = 0.2)$ for two speeds, Pe = 10 and 50. The time $\tilde{t} = 0.2$ corresponds to $\tilde{t}_3$ when Pe = 10, and it is five times longer than $\tilde{t}_3$ when Pe = 50.

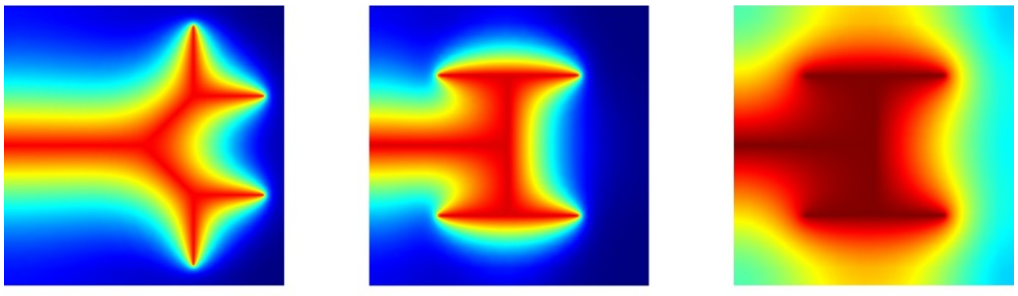

Figure 2.3: The effect of the line invasion speed (Pe) on the temperature field at the time $\tilde{t} = 0.2$ (note that $\tilde{t} = 0.2$ is equal to $\tilde{t}_2$ when Pe = 10).

The dimensionless average temperature $\theta_{avg} = (T_{avg} - T_0)/(T_1 - T_0)$ is a function of time $(\tilde{t})$ and invasion speed (Pe). This function is displayed in Fig. 2.4a,b. The $\theta_{avg}(\tilde{t})$ curves are S-shaped and become steeper as Pe increases. This effect is understandable, because the approach to the final uniform temperature $(\theta = 1)$ should faster when the tree invasion is faster. The question is whether the approach to final uniform temperature can be accelerated further even when the invasion speed (Pe) is fixed.

2.2 Free bifurcation angles

In accord with earlier design applications of the constructal law [28, 31-33], the path to greater flow access consists of endowing the flow configuration with greater freedom to morph. Here we explore the benefits of allowing the bifurcation angles to vary freely. In the first model (Fig. 2.2), the two branches were colinear, i.e. the branches formed 180° angles, which were fixed.

In Fig. 2.5 the branching angle β_1 is free to vary. We consider the full development of the first bifurcation, which lasts until the time t_2 defined in Fig. 2.2, i.e. until the first branches grow to their final length (L_2). The angle β_1 is the only feature that varies because the time $(\tilde{t}_2)$ and the invasion speed (Pe = 10) are fixed. We find that the average temperature of the heated domain exhibits a maximum at $\beta_1 = 90^\circ$, as shown in Fig. 2.5. This maximum is significant because the θ_{avg} value at $\beta_1 = 90^\circ$ is greater by 4.5 % than the θ_{avg} value found for $\beta_1 = 180^\circ$. The optimal bifurcation from L_1 to L_2 is

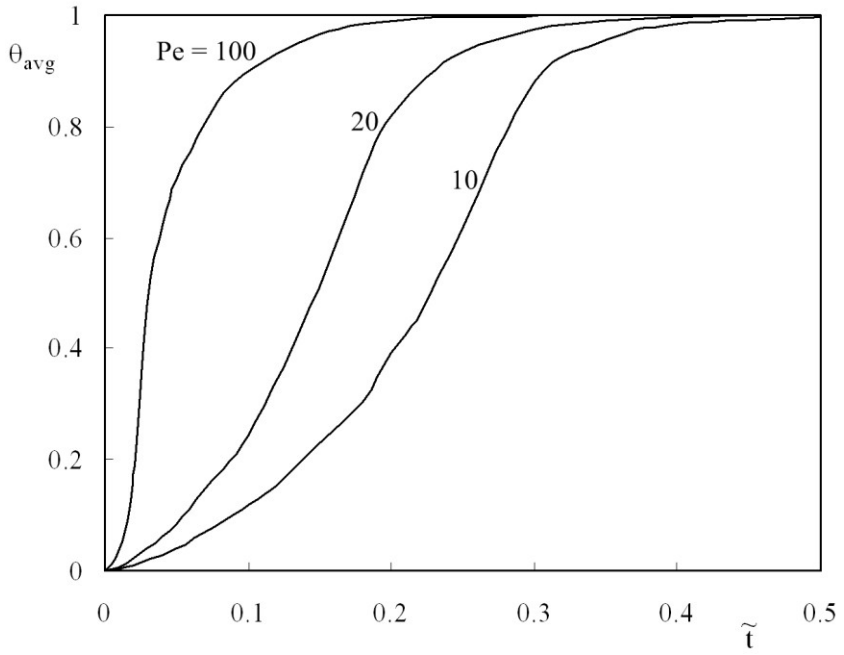

Figure 2.4a: The S-shaped history of the average temperature of the square domain in Fig. 2.2.

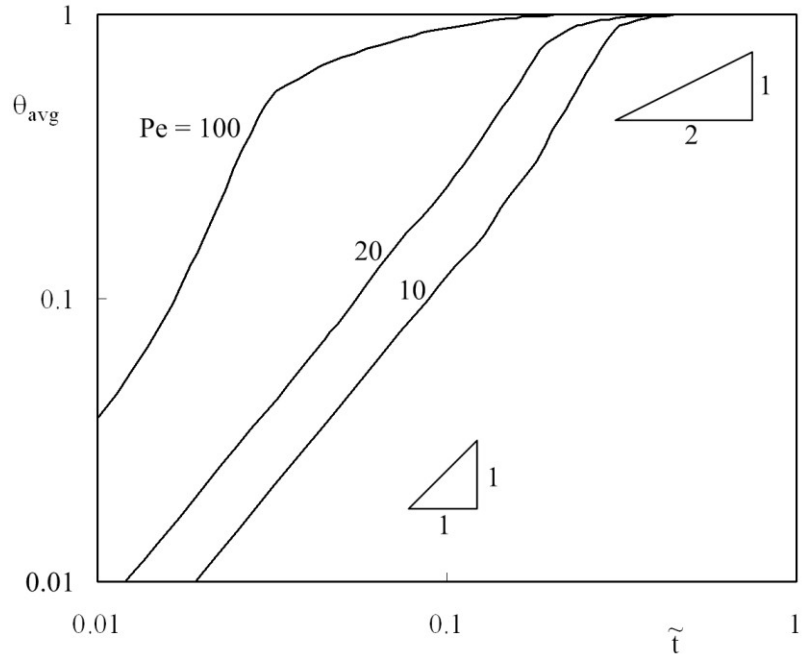

Figure 2.4b: The S-shaped history of the average temperature of the square domain in Fig. 2.2 (logarithmic scale).

drawn in Fig. 1.5 for Pe = 10.

At the next bifurcation time $(\tilde{t}_3)$, the L_3 branches have grown to their full lengths, Fig. 2.6. The angle β_2 between the L_3 branches is free to vary, while the first bifurcation angle is set at its value optimized at the time t_2, namely $\beta_1 = 90^\circ$. In Fig. 2.6 we found that $\theta_{avg}(\tilde{t}_3)$ has a maximum with respect to β_2, which is located at $\beta_2 = 90^\circ$. The value of $\theta_{avg}(90^\circ)$ exceeds by 13.4 % its corresponding value at $\tilde{t}_3$ in the rigid design of Fig. 2.2.

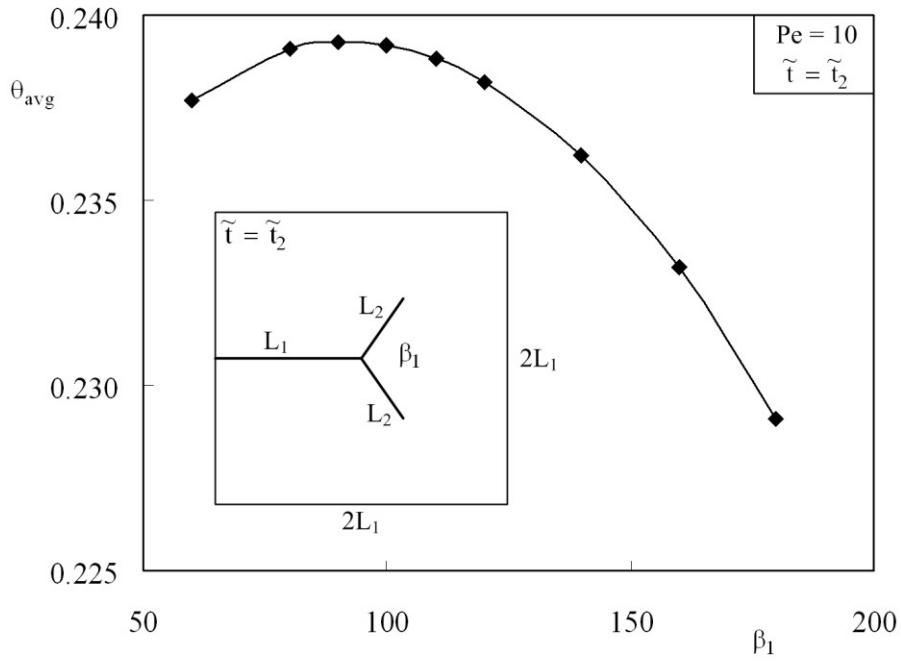

Figure 2.5: Freely varying angle of bifurcation β_1 at $\tilde{t} = \tilde{t}_2$, when Pe and the conducting space are fixed.

The tree with freely changing angles invades the square domain as shown in Fig. 2.6. The tree cannot grow freely beyond its L_3 branches, because the L_4 branches would

interfere with the square boundary. The S curve that corresponds to this tree design is plotted in Fig. 2.7 next to the corresponding curve of the rigid tree design (Fig. 2.2). Figure 2.7 shows that the average temperature of the conducting domain is greater when the bifurcation angles are free to vary and are chosen in order to heat the domain the fastest possible.

2.3 Freely morphing tree in a large domain

In order to postpone the interference between the invading tree and the boundaries of the domain, we enlarged by a factor of 5 the side of the conducting square. Now the area of the domain is 10 L_1 × 10 L_1, while the length of the trunk of the tree (at $\tilde{t} = \tilde{t}_1$) continues to be L_1, Fig. 2.8. Unlike in sections 2.1 and 2.2, where the lengths of the invading lines decreased in the sequence demanded by the T-shaped bifurcations in Fig.

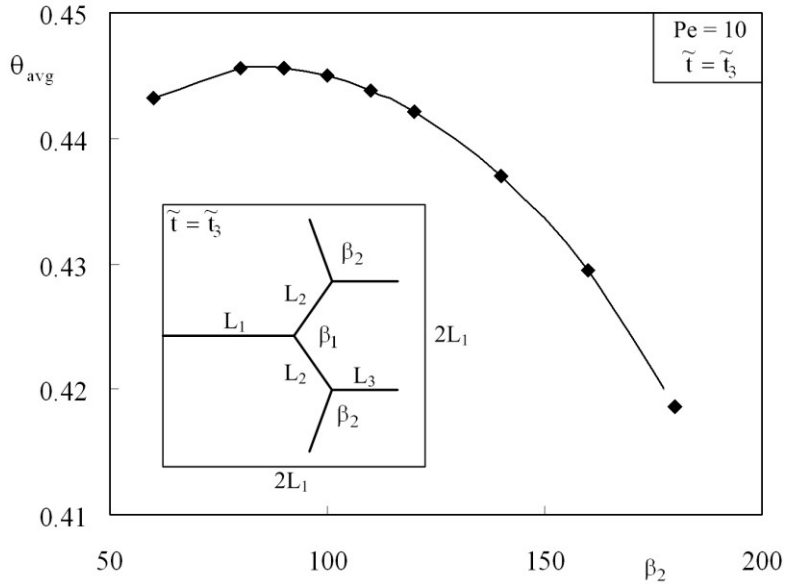

Figure 2.6: Freely varying angle β_2 at $\tilde{t} = \tilde{t}_3$, when Pe and the conducting space are fixed.

2.2 (namely, L_1, $L_2 = L_1/2$, $L_3 = L_1/2$, etc.), on the 10 L_1 × 10 L_1 domain we are free to vary not only the bifurcation angles but also the lengths of all the branches. For simplicity, we adopt the rule

$$\frac{L_{i+1}}{L_i} = 2^{-1/2} \tag{2.7}$$

because it corresponds to the average value of the L_{i+1}/L_i ratios in the designs of in Fig. 2.2.

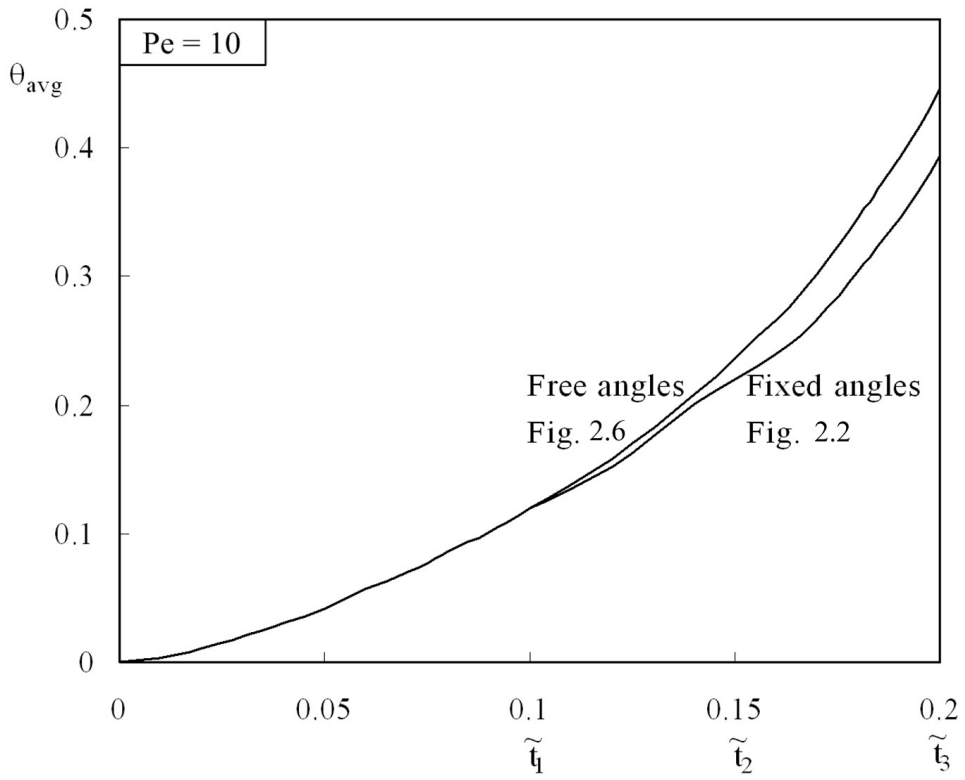

Figure 2.7: The S curve of tree invasion with free angles is steeper (faster) than the S curve of tree invasion with fixed branching angles (Fig. 2.2).

Figure 2.8 shows that the branching angle β_1 for maximum θ_{avg} is $\beta_1 = 100^\circ$. This angle is larger than the one found in Fig. 2.5, and indicates that the value of L_2/L_1 has an effect on the emerging optimal tree shape. To investigate the L_2/L_1 effect more closely, we repeated the work of Fig. 2.8 for the 2 L_1 × 2 L_1 conducting domain used to construct Fig. 2.5. The results are shown in Fig. 2.9, which can be compared directly with Fig. 2.5. In Fig. 2.9 the best β_1 is 100° and the maximum θ_{avg} is 0.3, while in Fig. 2.5 the corresponding values were 90° and 0.24.

We continued with the freely morphing tree on the 10 L_1 × 10 L_1 domain until the full development of the second branches ($\tilde{t} = \tilde{t}_3$), as shown in Fig. 1.10. The β_1 angle

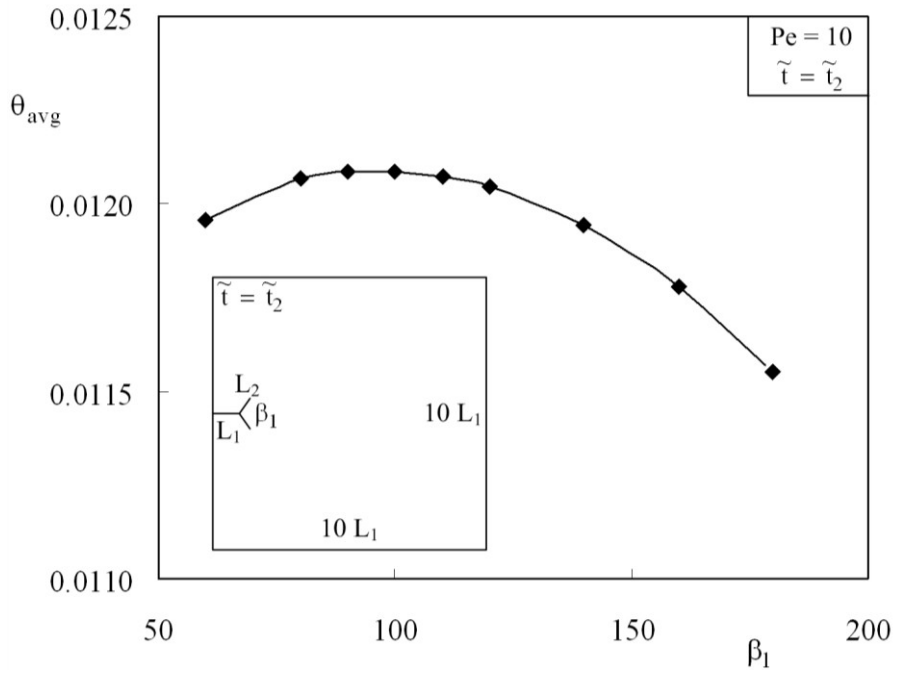

Figure 2.8: The optimization of the bifurcation angle β_2 when the conducting domain size is 10L_1 × 10 L_1.

was fixed at the value obtained at the time $\tilde{t} = \tilde{t}_2$ in Fig. 2.8 (namely, $\beta_1 = 100^\circ$). We found that the best β_2 in this case is 90°.

Finally, we repeated the work of Fig. 2.10 (that is, at $\tilde{t} = \tilde{t}_3$) by adopting the value $\beta_2 = 90^\circ$, and working "backward" on the value of β_1. We found that the best β_1 is 100°. The results found in this backward procedure agree with the results of Fig. 2.8.

2.4 The effect of the number of branching levels

The tree architectures discussed until now had no more than two levels of bifurcation. We examined the effect of the number of levels of bifurcation all the way to

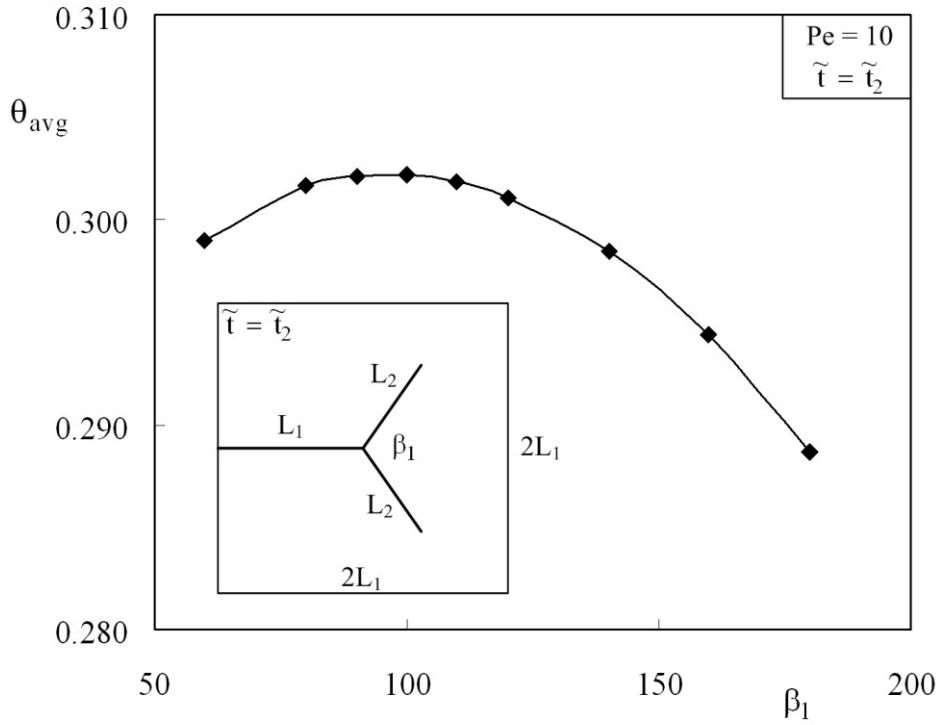

Figure 2.9: The optimization of the bifurcation angle β_1 when the conducting domain size is $2L_1 \times 2L_1$.

n = 4, which corresponds to the time $\tilde{t}_5$ in Fig. 2.2. We analyzed trees with T-shaped bifurcations, and their resulting S-curves are summarized in Fig. 2.11.

The steepest portion of the S-curve lasts longer as n increases, and the curve reaches its plateau region faster. Each new level of bifurcation of the invasion phase adds a segment to the steepest portion of the curve as n increases. The added segments become shorter as n increases, however, their effect on the slope of the curve in log-log representation is minimal (Fig. 2.11b). The slope of the S curve changes from 1 : 1 to 1 : 2, as in Fig. 2.4b. This change holds for all the n values.

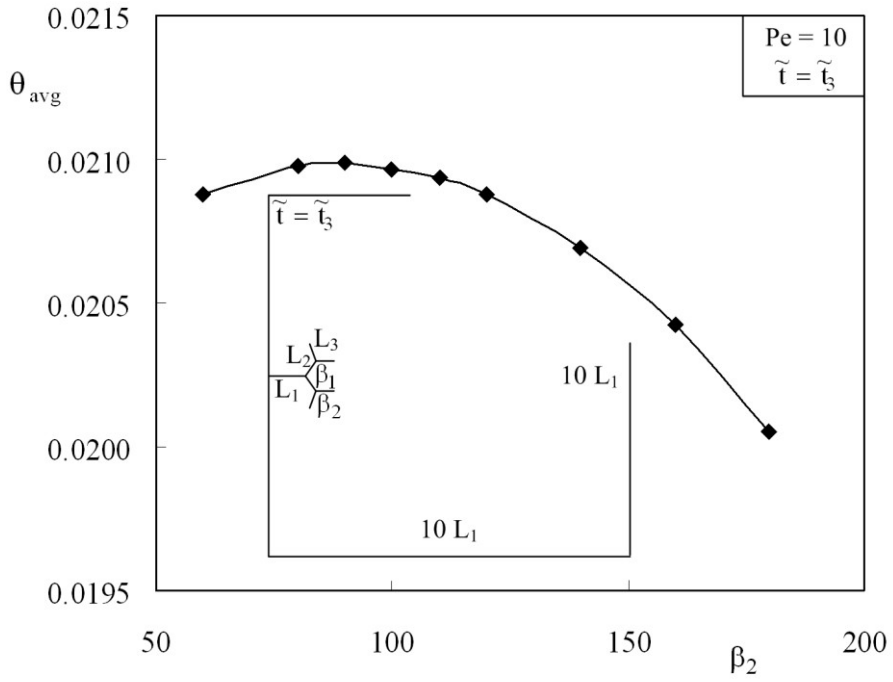

Figure 2.10: The optimization of β_2 when $\beta_1 = 100^\circ$ on the large domain $10L_1 \times 10 L_1$.

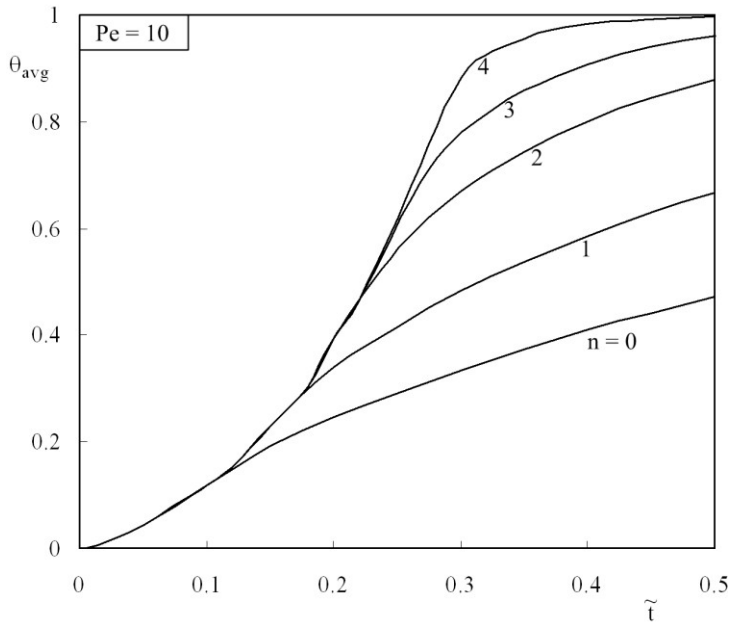

Figure 2.11a: The effect of the number of bifurcation levels on the shape of the S-curve.

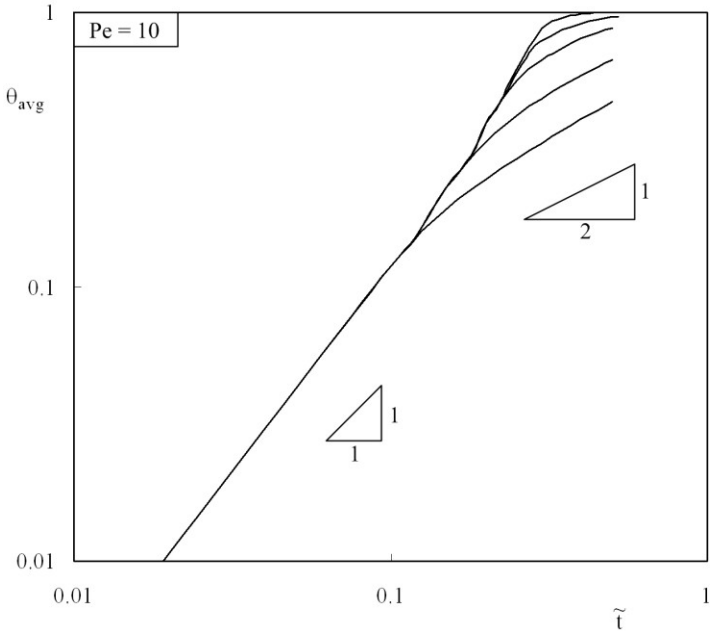

Figure 2.11b: The effect of the number of bifurcation levels on the shape of the S-curve (logarithmic scale).

The main conclusion from Fig. 2.11 is that greater coverage of the available space is achieved when the complexity of the structure of invading lines increases. Once the invasion phase runs its course, the consolidation phase proceeds in the same fashion (by diffusion) across interstices that are smaller and swept faster as n increases.

2.5 Analytical invasion-consolidation curve

In the theoretical scenario [26], the area of the square of the Fig. 2.2 was covered by conduction in two phases, cf. Fig. 2.12. During the invasion phase, the covered area increases as

$$A_i \sim A_{in}\left(\frac{t}{t_{in}}\right)^{3/2} \tag{2.8}$$

where

$$t_{in} \sim 3.4\frac{L_1}{V} \qquad\qquad A_{in} \sim 30\left(\frac{\alpha}{V}\right)^{1/2} L_1^{3/2} \tag{2.9}$$

The 3.4 factor appearing in the t_{in} expression accounts for the fact that the total length traveled at speed V by the tip of one of the invading lines in Fig. 2.2 approaches $3.4\,L_1$ when the number of branching levels is large. The factor 30 in the A_{in} formula emerges after summing up all the areas covered by diffusion in the intermediate vicinity of the invading lines, as shown analytically in Ref. 26.

During the consolidation phase, the area covered by conduction is

$$A_c \sim 4L_1^2\left(\frac{t}{t_{co}}\right)^{1/2} \tag{2.10}$$

where $4L_1^2$ is the total area, and

$$t_{co} \sim \frac{L_1^2}{5\alpha} \tag{2.11}$$

According to Fig. 2.12, the continuous S-curve for A(t) emerges after matching the two portions (A_i and A_c) in value and slope at $t \sim t_{in}$. As shown in the lower part of Fig. 2.12, the matching analysis requires that we shift the curve $A_c(t)$ of Eq. (2.10) by a time interval t_0, which is of order t_{in}; therefore Eq. (2.10) is replaced by

$$A_c \sim 4L_1^2\left(\frac{t - t_0}{t_{co}}\right)^{1/2} \tag{2.12}$$

Matching $A_i(t)$ and $A_c(t)$ in value at $t \sim t_{in}$ yields the first condition

$$\frac{A_{in}}{4L_1^2} \sim \left(\frac{t_{in} - t_0}{t_{co}}\right)^{1/2} \tag{2.13}$$

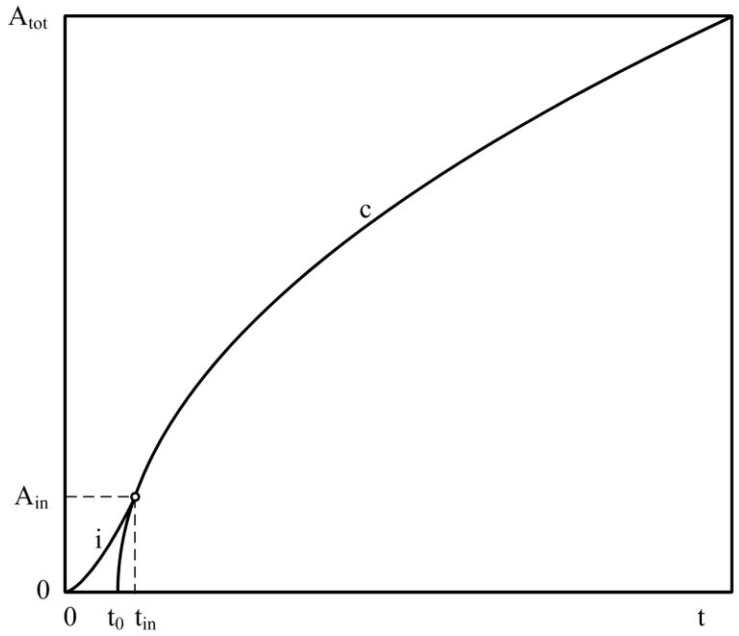

Figure 2.12: The analytical form of the S curve: invasion followed by consolidation.

Matching the slopes of $A_i(t)$ and $A_c(t)$ at $t \sim t_{in}$ yields the second condition

$$3\frac{A_{in}}{4L_1^2} \sim \frac{t_{in}}{\left[t_{co}\left(t_{in} - t_0\right)\right]^{1/2}} \tag{2.14}$$

Combining the two conditions we find that

$$t_0 \sim \frac{2}{3} t_{in} \tag{2.15}$$

$$\frac{A_{in}}{4L_1^2} \sim 2.38\,Pe^{-1/2} \tag{2.16}$$

Noteworthy is that, as expected, t_0 is of order t_{in}, and that Eq. (2.16) agrees with Eq. (2.9) for A_{in} within a factor of order 1, because Eq. (2.9) can be rewritten as $A_{in}/\left(4L_1^2\right) \sim 7.5\,Pe^{-1/2}$. The analysis continues by using Eq. (2.16) in place of Eq. (2.9) for A_{in}.

The analytical S-curve expression consists of $A_i(t)$ of Eq. (2.8) for $0 < t < t_{in}$, and $A_c(t)$ of Eq. (2.12) for > t_{in}. The resulting A(t) curve can be expressed as $\theta_{avg}(\tilde{t})$ as follows. First, if we assign to the area covered by conduction (A_i or A_c) the dimensionless temperature 1, and to the remaining area $\left[4L_1^2 - \left(A_i \text{ or } A_c\right)\right]$ the temperature 0, then the dimensionless average temperature of the $4L_1^2$ square is

$$\theta_{avg} \sim \frac{A_i \text{ or } A_c}{4L_1^2} \tag{2.17}$$

The dimensionless time is

$$\tilde{t} \sim \frac{\alpha t}{L_1^2} \sim \frac{t}{5t_{co}} \tag{2.18}$$

Using Eqs. (2.17) and (2.18), the $A_i(t)$ and $A_c(t)$ expressions become

$$\theta_{avg,\,i} \sim 0.38\,\mathrm{Pe}\,\tilde{t}^{\,3/2} \tag{2.19}$$

$$\theta_{avg,\,c} \sim 5^{1/2}\left(\tilde{t} - 2.27\,\mathrm{Pe}^{-1}\right)^{1/2} \tag{2.20}$$

It can be verified that the curves of Eqs. (2.12) and (2.13) have the same value and slope at $t \sim t_{in}$, which in the current notation means at $\tilde{t} \sim 3.4\,\mathrm{Pe}^{-1}$.

2.6 Discussion

In this chapter we showed that the steepest S curve for spreading by diffusion in a solid corresponds to a tree design that morphs freely. When the tree configuration is fixed, the S curve becomes steeper as the Peclet number increases. By varying the branching angles we found that the tree designs with Y-shaped branching have steeper S curves than the tree designs with T-shaped branching.

The lengths of the invading lines were selected in two ways, as in Fig. 2.2, and based on the rule $L_{i+1}/L_i = 2^{-1/2}$. The optimal bifurcation angles decrease as the number of the bifurcation level increases, however, when the conducting domain is much larger than the tree structure the optimum bifurcation angles become less sensitive to increases in the number of bifurcation levels.

We also found that increasing the number of branching levels makes the steepest section of the S curve longer, and the curve reaches its plateau faster. However, increasing the number of the bifurcation levels does not significantly change the performance of the design because the steep segment added by each new level of bifurcation becomes shorter as the number of bifurcation levels increases, Fig. 2.11a,b.

3. Vascularization for cooling and mechanical strength

Cooling and mechanical strength requirements place limits on the improvement of many advanced technologies, from electronic packages to structures for future air vehicles. Although the strength of the structure can be increased by adding more and stronger material, the challenge is to reduce the volume and weight of the structure. At the same time, the structure must be able to resist the effect of sudden heating, volumetrically or on its envelope. The design challenge is to increase structural strength while decreasing the maximum temperature in the volume, and reducing the volume.

Even though these objectives seem to be in conflict, the “flow of stresses” concept of constructal theory shows how to achieve mechanical strength by morphing the design to meet these two objectives and using less material [34]. The approach is to allow the structure to change freely by placing the material in places where stresses flow with fewer strangulations. This concept is the same as in the constructal design of thermofluid architectures: the design is free to change such that more flow volume is placed where it is needed. The current literature focuses mostly on thermofluid design [32, 35-40] and smart features such as self-cooling and self-healing [41-43], and in a few instances mechanical strength was used as a design objective [44, 45].

In the present study the flow volume houses three types of flows at the same time: stresses, fluid, and heat. We seek architectures that facilitate these three flows at the same time. The emerging designs are "designed porous structures" that consist of radial and tree-shaped cooling channels.

3.1 Hess-Murray's law: Temperature dependence

Dendritic flow structures offer less resistance when bifurcations are accompanied by optimal step-changes in diameters, in accord with the Hess-Murray rule (e.g. Ref. [34]). This design rule applies to isothermal systems, and to fluids with temperature independent properties. Here we review concept by assuming the more general case of temperature dependent properties. Additional generality is provided by the assumption that the mother tube is continued by n identical daughter tubes, and by the fact that the flow regime can be laminar or turbulent. The fluid volume is fixed, and it is used as constraint in the search for the optimal mother/daughter diameter ratios. The pressure drop formula for laminar flow is

$$\Delta P = C\nu_i \dot{m}_i \frac{L_i}{D_i^4} \tag{3.1}$$

where $C = 128/\pi$, and ν_i is the kinematic viscosity corresponding to the mean temperature $T_{me} = \int T dV \Big/ \int dV$. If one tube branches into n identical tubes, the total flow volume and pressure drop are

$$V = \pi \frac{D_1^2}{4} L_1 + n\pi \frac{D_2^2}{4} L_2 \tag{3.2}$$

$$\Delta P = C\nu_1 \dot{m}_1 \frac{L_1}{D_1^4} + C\nu_2 \dot{m}_2 \frac{L_2}{D_2^4} \tag{3.3}$$

where $\dot{m}_2 = \dot{m}_1 / n$. The diameter ratio for minimum ΔP is

$$\frac{D_1}{D_2} = n^{1/3} \left(\frac{\nu_1}{\nu_2} \right)^{1/6} \tag{3.4}$$

The case of fully developed turbulent flow is analyzed similarly. The pressure drop formula for turbulent flow is

$$\Delta P = \frac{C_T \dot{m}_i^2}{\rho_i} \frac{L_i}{D_i^5} \tag{3.5}$$

where $C_T = 32f/\pi^2$, f is the friction factor which is constant in the fully rough regime, and ρ_i is the density of the fluid corresponding to T_{me}. The total fluid volume and pressure drop are

$$V = \pi \frac{D_1^2}{4} L_1 + n\pi \frac{D_2^2}{4} L_2 \tag{3.6}$$

$$\Delta P = \frac{C_T \dot{m}_1^2}{\rho_1} \frac{L_1}{D_1^5} + \frac{C_T \dot{m}_2^2}{\rho_2} \frac{L_2}{D_2^5} \tag{3.7}$$

where $\dot{m}_2 = \dot{m}_1 / n$. The optimal diameter ratio is

$$\frac{D_1}{D_2} = n^{3/7} \left(\frac{\rho_2}{\rho_1} \right)^{1/7} \tag{3.8}$$

In summary, the effect of variable properties is felt through the ratios $(\nu_1/\nu_2)^{1/6}$ and $(\rho_2/\rho_1)^{1/7}$ for laminar flow and turbulent flow, respectively. In the following work, the temperature variations are assumed to be small enough so that at every branching point the ratios $(\nu_1/\nu_2)^{1/6}$ and $(\rho_2/\rho_1)^{1/7}$ are sufficiently close to 1.

3.2 Model

We relied on a numerical model of the thermofluid and mechanical behavior of the circular plate. The diameter and thickness of the plate are D and H, and their ratio is

fixed D/H = 10. The total volume is fixed, and so is the volume of the channels. The plate is subjected to uniformly distributed force and uniform heat flux, both acting from below, Fig. 3.1. Because the plate is thin, the heating from below is also an adequate approximation of situations where the heating is distributed volumetrically. The fluid flow is governed by the mass conservation and momentum equations, which for incompressible and steady flow are:

$$\frac{\partial u}{\partial x} + \frac{\partial v}{\partial y} + \frac{\partial w}{\partial z} = 0 \tag{3.9}$$

$$u\frac{\partial u}{\partial x} + v\frac{\partial u}{\partial y} + w\frac{\partial u}{\partial z} = -\frac{1}{\rho}\frac{\partial P}{\partial x} + \nu\left(\frac{\partial^2 u}{\partial x^2} + \frac{\partial^2 u}{\partial y^2} + \frac{\partial^2 u}{\partial z^2}\right) \tag{3.10}$$

$$u\frac{\partial v}{\partial x} + v\frac{\partial v}{\partial y} + w\frac{\partial v}{\partial z} = -\frac{1}{\rho}\frac{\partial P}{\partial y} + \nu\left(\frac{\partial^2 v}{\partial x^2} + \frac{\partial^2 v}{\partial y^2} + \frac{\partial^2 v}{\partial z^2}\right) \tag{3.11}$$

$$u\frac{\partial w}{\partial x} + v\frac{\partial w}{\partial y} + w\frac{\partial w}{\partial z} = -\frac{1}{\rho}\frac{\partial P}{\partial z} + \nu\left(\frac{\partial^2 w}{\partial x^2} + \frac{\partial^2 w}{\partial y^2} + \frac{\partial^2 w}{\partial z^2}\right) \tag{3.12}$$

Here x, y and z are the coordinates, u, v and w are the velocity components corresponding to these coordinates, and P, ν and ρ are the pressure, kinematic viscosity and fluid density. The temperature distribution is found by solving the energy equation

$$\rho c_P\left(u\frac{\partial T}{\partial x} + v\frac{\partial T}{\partial y} + w\frac{\partial T}{\partial z}\right) = k\left(\frac{\partial^2 T}{\partial x^2} + \frac{\partial^2 T}{\partial y^2} + \frac{\partial^2 T}{\partial z^2}\right) \tag{3.13}$$

where c_P is the specific heat at constant pressure, T is the temperature, and k is the fluid thermal conductivity.

The solid plate is isotropic, and its deformation is elastic and small when compared with the dimensions D and H. In tensor notation, the momentum equation and generalized Hooke's law are

$$\sigma_{ij,i} + f_j = 0 \tag{3.14}$$

$$\sigma_{ij} = C_{ijkl}\varepsilon_{kl} \tag{3.15}$$

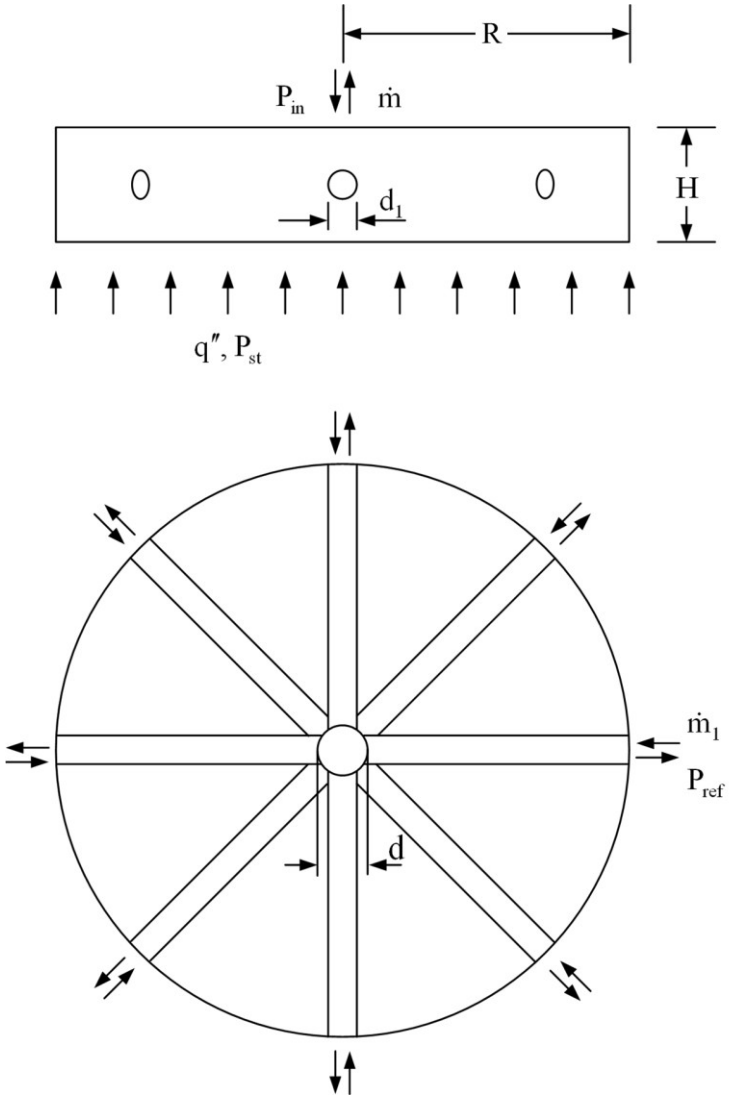

Figure 3.1: Radial cooling duct configuration.

where σ_{ij}, C_{ijkl}, f and ε_{kl} are the stress tensor, elasticity tensor, volume forces and strain tensor, respectively. Volume forces are assumed to be negligible when compared with the surface forces. Equation (3.14) becomes

$$\frac{\partial \sigma_{xx}}{\partial x} + \frac{\partial \tau_{yx}}{\partial y} + \frac{\partial \tau_{zx}}{\partial z} = 0 \tag{3.16}$$

$$\frac{\partial \tau_{xy}}{\partial x} + \frac{\partial \sigma_{yy}}{\partial y} + \frac{\partial \tau_{zy}}{\partial z} = 0 \tag{3.17}$$

$$\frac{\partial \tau_{xz}}{\partial x} + \frac{\partial \tau_{yz}}{\partial y} + \frac{\partial \sigma_{zz}}{\partial z} = 0 \tag{3.18}$$

where σ and τ are the normal and shear stresses. Because the plate is isotropic and elastic, the elasticity tensor has both minor and major symmetries, i.e. $C_{ijkl} = C_{klij}$ and $C_{ijkl} = C_{jikl}$. Because of these symmetries in the fourth order tensor we can simplify the generalized Hooke's law in the form of $\sigma = K\varepsilon$, where σ and ε are vectors, K is a second order tensor, γ is the Poisson ratio, and E is the elasticity modulus.

$$\begin{bmatrix} \sigma_{xx} \\ \sigma_{yy} \\ \sigma_{zz} \\ \tau_{yz} \\ \tau_{zx} \\ \tau_{xy} \end{bmatrix} = \frac{E}{(1+\gamma)(1-2\gamma)} \begin{bmatrix} 1-\gamma & \gamma & \gamma & 0 & 0 & 0 \\ \gamma & 1-\gamma & \gamma & 0 & 0 & 0 \\ \gamma & \gamma & 1-\gamma & 0 & 0 & 0 \\ 0 & 0 & 0 & 1-2\gamma & 0 & 0 \\ 0 & 0 & 0 & 0 & 1-2\gamma & 0 \\ 0 & 0 & 0 & 0 & 0 & 1-2\gamma \end{bmatrix} \begin{bmatrix} \varepsilon_{xx} \\ \varepsilon_{yy} \\ \varepsilon_{zz} \\ \varphi_{yz} \\ \varphi_{zx} \\ \varphi_{xy} \end{bmatrix} \tag{3.19}$$

The strain displacement relations are

$$\varepsilon_{xx} = \frac{\partial r_x}{\partial x}, \qquad \varepsilon_{yy} = \frac{\partial r_y}{\partial y}, \qquad \varepsilon_{zz} = \frac{\partial r_z}{\partial z} \tag{3.20}$$

$$\varphi_{xy} = \varphi_{yx} = \frac{\partial r_x}{\partial y} + \frac{\partial r_y}{\partial x}, \qquad \varphi_{zy} = \varphi_{yz} = \frac{\partial r_z}{\partial y} + \frac{\partial r_y}{\partial z}, \qquad \varphi_{zx} = \varphi_{xz} = \frac{\partial r_z}{\partial x} + \frac{\partial r_x}{\partial z} \tag{3.21}$$

where r_x, r_y and r_z are the displacements in the directions of the coordinates indicated by the subscript.

Equations (3.9) – (3.12) can be nondimensionalized by using D as the length scale and constructing dimensionless velocities in the form of Reynolds numbers

$$\tilde{x}, \tilde{y}, \tilde{z} = (x, y, z)/D, \qquad \tilde{u} = (uD)/\nu, \qquad \tilde{v} = (vD)/\nu, \qquad \tilde{w} = (wD)/\nu \tag{3.22}$$

The dimensionless excess pressure is defined as

$$\tilde{P} = \frac{(P - P_{ref})D^2}{\mu\alpha} \tag{3.23}$$

where P, P_{ref}, μ and α are the local pressure, the reference (outlet) pressure of the fluid, the dynamic viscosity, and the thermal diffusivity. The dimensionless temperature is defined as

$$\tilde{T} = \frac{(T - T_{ref})k}{q''D} \tag{3.24}$$

where T_{ref} is the fluid inlet temperature. The continuity of the heat flux and dimensionless conductivity and heat flux are expressed by

$$q'' = -k_s \frac{\partial T}{\partial n} = -k \frac{\partial T}{\partial n}, \qquad \tilde{k} = \frac{k_s}{k}, \qquad \tilde{q} = \frac{q''}{q''} \tag{3.25}$$

where k_s and k are the thermal conductivities of the solid and the fluid.

Equations (3.16) – (3.19) can also be nondimensionalized by using D as the reference for displacements and coordinates, and P_{st} as the reference for the stresses, elasticity and mechanical load.

$$(\tilde{r}_x, \tilde{r}_y, \tilde{r}_z, \tilde{x}, \tilde{y}, \tilde{z}) = (r_x, r_y, r_z, x, y, z)/D \tag{3.26}$$

$$\tilde{\varepsilon}_{xx} = \frac{\partial \tilde{r}_x}{\partial \tilde{x}}, \qquad \tilde{\varepsilon}_{yy} = \frac{\partial \tilde{r}_y}{\partial \tilde{y}}, \qquad \tilde{\varepsilon}_{zz} = \frac{\partial \tilde{r}_z}{\partial \tilde{z}} \tag{3.27}$$

$$\tilde{\varphi}_{xy} = \tilde{\varphi}_{yx} = \frac{\partial \tilde{r}_x}{\partial \tilde{y}} + \frac{\partial \tilde{r}_y}{\partial \tilde{x}}, \qquad \tilde{\varphi}_{zy} = \tilde{\varphi}_{yz} = \frac{\partial \tilde{r}_z}{\partial \tilde{y}} + \frac{\partial \tilde{r}_y}{\partial \tilde{z}}, \qquad \tilde{\varphi}_{zx} = \tilde{\varphi}_{xz} = \frac{\partial \tilde{r}_z}{\partial \tilde{x}} + \frac{\partial \tilde{r}_x}{\partial \tilde{z}} \tag{3.28}$$

$$(\tilde{E}, \tilde{\sigma}, \tilde{\tau}, \tilde{P}_{st}) = (E, \sigma, \tau, P_{st})/P_{st} \tag{3.29}$$

P_{st} is the mechanical load applied uniformly from the bottom of the plate. The dimensionless equations are

$$\frac{\partial \tilde{u}}{\partial \tilde{x}} + \frac{\partial \tilde{v}}{\partial \tilde{y}} + \frac{\partial \tilde{w}}{\partial \tilde{z}} = 0 \tag{3.30}$$

$$\tilde{u}\frac{\partial \tilde{u}}{\partial \tilde{x}} + \tilde{v}\frac{\partial \tilde{u}}{\partial \tilde{y}} + \tilde{w}\frac{\partial \tilde{u}}{\partial \tilde{z}} = -\frac{1}{Pr}\frac{\partial \tilde{P}}{\partial \tilde{x}} + \left(\frac{\partial^2 \tilde{u}}{\partial \tilde{x}^2} + \frac{\partial^2 \tilde{u}}{\partial \tilde{y}^2} + \frac{\partial^2 \tilde{u}}{\partial \tilde{z}^2}\right) \tag{3.31}$$

$$\tilde{u}\frac{\partial \tilde{v}}{\partial \tilde{x}} + \tilde{v}\frac{\partial \tilde{v}}{\partial \tilde{y}} + \tilde{w}\frac{\partial \tilde{v}}{\partial \tilde{z}} = -\frac{1}{Pr}\frac{\partial \tilde{P}}{\partial \tilde{y}} + \left(\frac{\partial^2 \tilde{v}}{\partial \tilde{x}^2} + \frac{\partial^2 \tilde{v}}{\partial \tilde{y}^2} + \frac{\partial^2 \tilde{v}}{\partial \tilde{z}^2}\right) \tag{3.32}$$

$$\tilde{u}\frac{\partial \tilde{w}}{\partial \tilde{x}} + \tilde{v}\frac{\partial \tilde{w}}{\partial \tilde{y}} + \tilde{w}\frac{\partial \tilde{w}}{\partial \tilde{z}} = -\frac{1}{Pr}\frac{\partial \tilde{P}}{\partial \tilde{y}} + \left(\frac{\partial^2 \tilde{w}}{\partial \tilde{x}^2} + \frac{\partial^2 \tilde{w}}{\partial \tilde{y}^2} + \frac{\partial^2 \tilde{w}}{\partial \tilde{z}^2}\right) \tag{3.33}$$

$$\tilde{u}\frac{\partial \tilde{T}}{\partial \tilde{x}} + \tilde{v}\frac{\partial \tilde{T}}{\partial \tilde{y}} + \tilde{w}\frac{\partial \tilde{T}}{\partial \tilde{z}} = \frac{\partial^2 \tilde{T}}{\partial \tilde{x}^2} + \frac{\partial^2 \tilde{T}}{\partial \tilde{y}^2} + \frac{\partial^2 \tilde{T}}{\partial \tilde{z}^2} \tag{3.34}$$

where Pr is Prandtl number. The energy equation for the domain occupied by the solid structure is

$$\frac{\partial^2 \tilde{T}}{\partial \tilde{x}^2} + \frac{\partial^2 \tilde{T}}{\partial \tilde{y}^2} + \frac{\partial^2 \tilde{T}}{\partial \tilde{z}^2} = 0 \tag{3.35}$$

The dimensionless momentum equation and Hooke's law for the solid domain are

$$\frac{\partial \tilde{\sigma}_{xx}}{\partial \tilde{x}} + \frac{\partial \tilde{\tau}_{yx}}{\partial \tilde{y}} + \frac{\partial \tilde{\tau}_{zx}}{\partial \tilde{z}} = 0 \tag{3.36}$$

$$\frac{\partial \tilde{\tau}_{xy}}{\partial \tilde{x}} + \frac{\partial \tilde{\sigma}_{yy}}{\partial \tilde{y}} + \frac{\partial \tilde{\tau}_{zy}}{\partial \tilde{z}} = 0 \tag{3.37}$$

$$\frac{\partial \tilde{\tau}_{xz}}{\partial \tilde{x}} + \frac{\partial \tilde{\tau}_{yz}}{\partial \tilde{y}} + \frac{\partial \tilde{\sigma}_{zz}}{\partial \tilde{z}} = 0 \tag{3.38}$$

$$\begin{bmatrix} \tilde{\sigma}_{xx} \\ \tilde{\sigma}_{yy} \\ \tilde{\sigma}_{zz} \\ \tilde{\tau}_{yz} \\ \tilde{\tau}_{zx} \\ \tilde{\tau}_{xy} \end{bmatrix} = \frac{\tilde{E}}{(1+\gamma)(1-2\gamma)} \begin{bmatrix} 1-\gamma & \gamma & \gamma & 0 & 0 & 0 \\ \gamma & 1-\gamma & \gamma & 0 & 0 & 0 \\ \gamma & \gamma & 1-\gamma & 0 & 0 & 0 \\ 0 & 0 & 0 & 1-2\gamma & 0 & 0 \\ 0 & 0 & 0 & 0 & 1-2\gamma & 0 \\ 0 & 0 & 0 & 0 & 0 & 1-2\gamma \end{bmatrix} \begin{bmatrix} \tilde{\varepsilon}_{xx} \\ \tilde{\varepsilon}_{yy} \\ \tilde{\varepsilon}_{zz} \\ \tilde{\varphi}_{yz} \\ \tilde{\varphi}_{zx} \\ \tilde{\varphi}_{xy} \end{bmatrix} \tag{3.39}$$

3.3 Radial cooling ducts

We begin with the simpler structure, which consists of radial cooling ducts, Fig. 3.1. The heat flux and mechanical load are fixed. The pressure difference between inlet and outlet is nondimensinalized as [46, 47].

$$\tilde{P}_{max} = \frac{(P_{in} - P_{ref})D^2}{\mu\alpha} \tag{3.40}$$

The value of $\tilde{P}_{max}$ represents the dimensionless overall pressure difference. We used $\tilde{P}_{max}$ values of order 10^7 and 10^8, which correspond to Reynolds numbers smaller than 2000 in every channel, i.e. laminar flow everywhere. The fluid volume is fixed at

5% of the total volume. In addition, we assumed $\widetilde{k} = 20$, $\gamma = 0.33$ and $\widetilde{E} = 2 \times 10^6$. The dimensionless heat flux and mechanical load applied from the bottom are $\widetilde{q} = 1$ and $\widetilde{P}_{st} = 1$. The diameter of the duct placed in the center of the plate is d = 0.05 D. The diameter of the radial ducts varies with the number of the ducts.

The computations were performed in dimensionless form by using a finite element package [29]. In order to confirm whether or not the solution is independent from the size of mesh, the solution was performed with a coarse mesh and then was performed again using finer meshes until the changes in peak temperature, maximum velocity and maximum stress become of order 1%.

Figures 3.2a, b show how the maximum temperature $\widetilde{T}_{max}$ varies with the number of the cooling ducts (n) when $\widetilde{P}_{max}$ is 10^7 and 10^8. The maximum temperature occurs in the middle of the space formed between the two closest cooling ducts of diameter d_1, Fig. 3.3a. The red and blue regions in Fig. 3.3a represent the maximum and minimum temperatures on the mid plane of the circular disc. The configuration with 8 ducts and outlet in the center has a region of low temperature in the center. When the number of cooling ducts is greater than 24, the hottest spot is in the center of the plate if the flow leaves from the center and on the rim if the flow enters through the center.

The distribution of the von Mises stress is similar in the all cases, and it is illustrated for 16 cooling ducts of diameter d_1 in Fig. 3.3b. Red and blue colors indicate the maximum and minimum stresses. The maximum stress occurs in the center of the plate. The minimum is half way between the center and the edge of the plate, on a circle concentric

with the plate center. This stress distribution suggests moving the duct of diameter d from the center of the plate to the blue region.

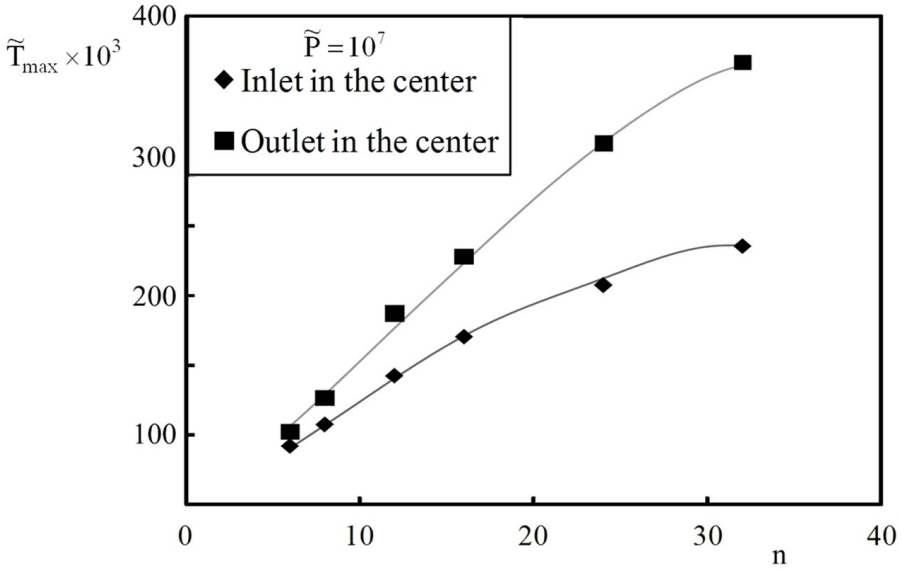

(a)

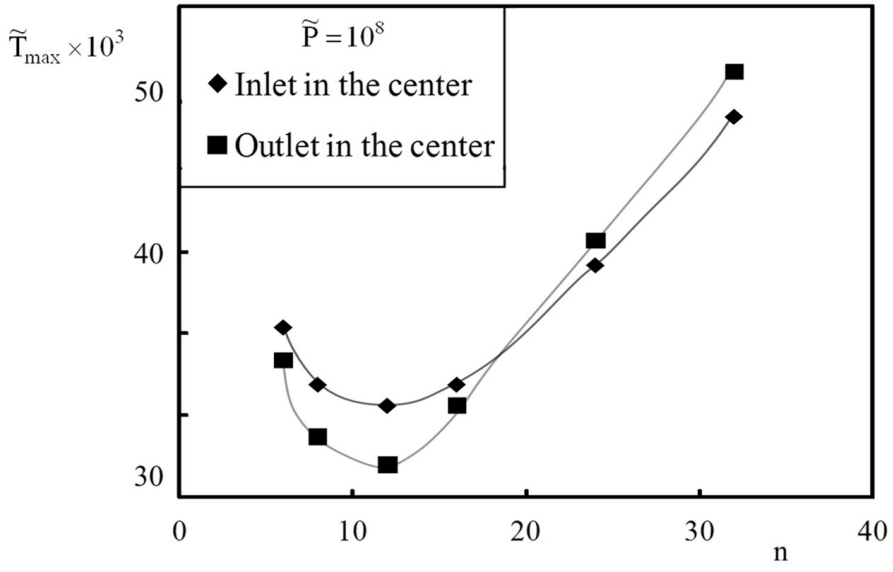

(b)

Figure 3.2: Peak temperature relative to the number of cooling ducts: (a) $\widetilde{P}_{max} = 10^7$**, (b)** $\widetilde{P}_{max} = 10^8$**.**

The purpose of morphing the shape is to decrease the peak temperature and stress. Figures 3.4a, b summarize the relation between the temperature, stress and number of ducts when $\widetilde{P}_{max}$ is 10^7 and 10^8, respectively. When the number of the cooling ducts

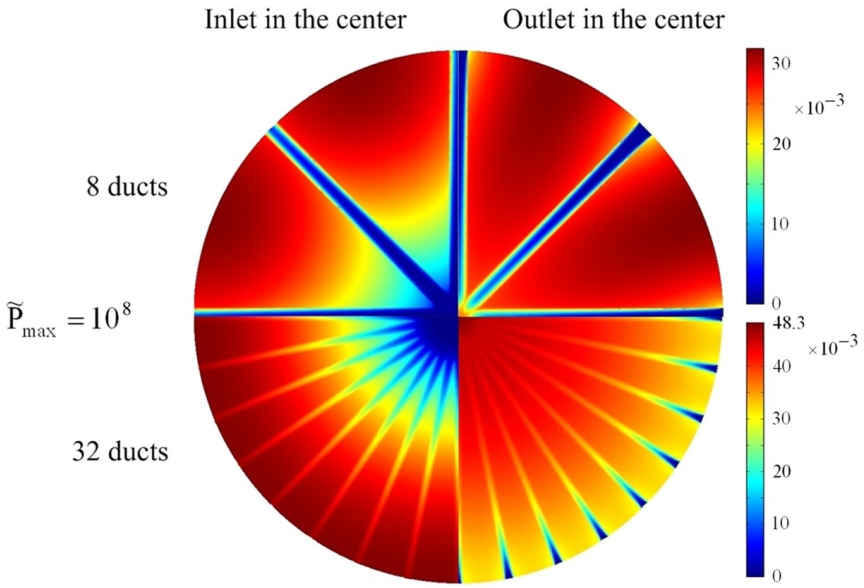

(a)

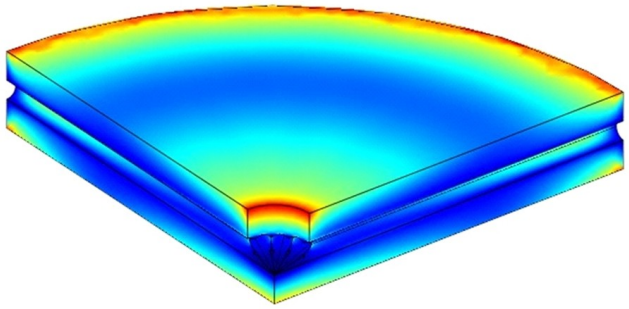

(b)

Figure 3.3: (a) The temperature distribution in the mid plane of the circular disc, red and blue represent the maximum and minimum temperature, respectively, $\widetilde{P}_{max} = 10^8$; (b) The von Mises stress of the circular disc, red and blue represent maximum and minimum stresses, respectively.

increases, the maximum stress decreases from n = 6 to n = 8 and then increases. This is due to the fact that the maximum stress increases in the vicinity of the junctions of the cooling ducts. In the radial configuration, every cooling duct is connected to the center, and the material between two cooling ducts is thinner close to the center and thicker close to the rim. The material thickness between cooling ducts becomes smaller close to the center. When n increases from 24 to 32, the stresses in this region increase rapidly. Even though n = 8 is the design for minimum $\tilde{\sigma}_{max}$, neighboring designs (n = 6 and n = 12) offer minimum peak temperatures for $\tilde{P}_{max} = 10^7$ and 10^8, respectively.

In summary, when $\tilde{P}_{max}$ is specified, it is possible to identify one design (or a group of similar designs) that provides low peak stresses and peak temperatures. Note that Fig. 3.4a is identical to the n > 12 part of Fig. 3.4b, therefore if $\tilde{P}_{max}$ is increased above 10^8, we can expect the design with minimum $\tilde{T}_{max}$ to be a design with n > 12.

3.4 Trees with one pairing level

Consider next a tree shaped construction with one pairing level, Fig. 3.5a. Flow enters through the center of the circular plate and flows in three ducts of length r and diameter d2. Later, the flow is distributed to six ducts of diameter d3. The outlet locations of the d3 ducts are equidistant on the disc perimeter. In this section we determine how the tree pattern affects the mechanical strength of the plate and the temperature distribution. We examined eight r/R ratios: 0, 0.1, ..., 0.8. The flow volume is fixed, and the flow

volume fraction is 0.05. At every pairing junction, the duct diameter increases by the factor $2^{1/3}$, which is the optimal factor for laminar flow (Section 3.2).

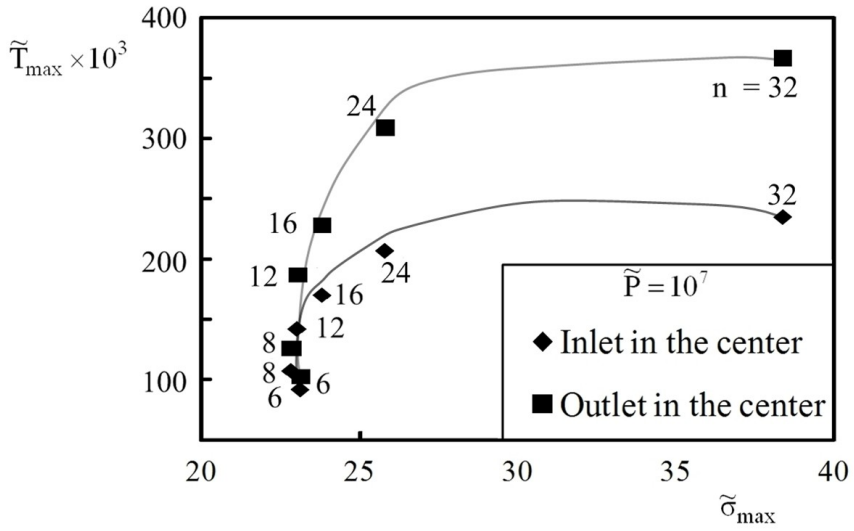

(a)

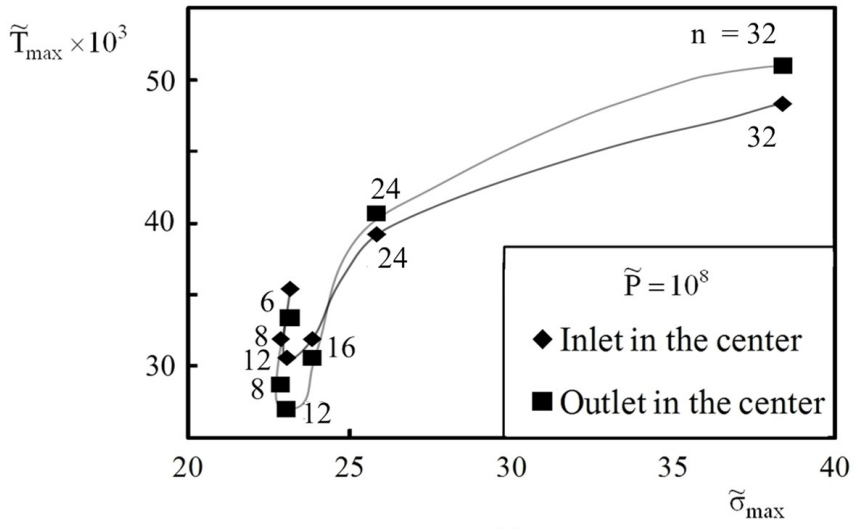

(b)

Figure 3.4: The effect of the number of cooling ducts on the maximum temperature and stress: (a) $\widetilde{P}_{max} = 10^7$; (b) $\widetilde{P}_{max} = 10^8$.

Figure 3.5b shows how the temperature distribution changes on the mid plane of the circular disc when we change the radial position of the pairings (r/R ratio) and inlet direction of the coolant, $\widetilde{P}_{max} = 10^8$.

Figures 3.6a, b show how the maximum stress and temperature of the structure change relative to the r/R ratio. When $\widetilde{P}_{max}$ is 10^7 the maximum temperature occurs on the edge of the circular plate, half way between the ducts of the diameter d_3. If r/R increases from r/R = 0 to 0.2 the maximum temperature decreases, and then it increases. When $\widetilde{P}_{max} = 10^8$ and the coolant fluid enters from the center, the maximum temperature decreases as r/R increases and becomes minimum at r/R = 0.1, and then it increases. If the coolant fluid enters from the rim, $\widetilde{T}_{max}$ increases from r/R = 0 to 0.1, then it decreases from r/R = 0.1 to 0.2, and when r/R > 0.2 $\widetilde{T}_{max}$ increases if r/R increases.

The maximum stress increases as r/R increases, and then it decreases when r/R > 0.4. The maximum stress exhibits a second minimum after r/R = 0 at r/R = 0.6, and after r/R = 0.6, it increases again, Figs. 3.6a, b. The reason why the maximum stress decreases when r/R increases from 0.4 to 0.6 is that the location of the pairing junction is in the minimum stress region, Fig. 3.3b.

3.5 Trees with two pairing levels

The next group of configurations that we explored was tree shaped designs with two pairing levels, Fig. 3.7a. The coolant fluid enters through the center of the circular plate, and flows through three ducts of length r_1 and diameter d_4. It is then distributed to six ducts of diameter d_5, and finally flows through 12 ducts of diameter d_6. The flow rates

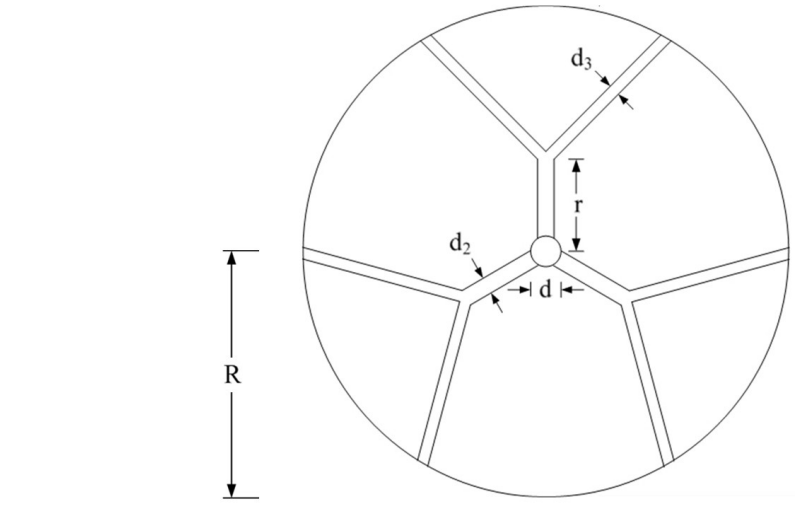

(a)

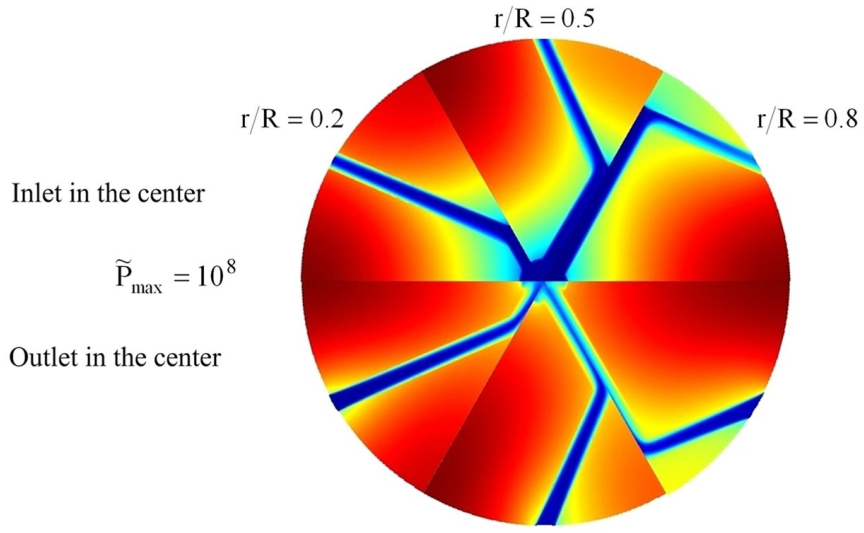

(b)

Figure 3.5: (a) Tree-shaped design with one pairing level; (b) The temperature distribution in the mid plane of the circular disc, $\widetilde{P}_{max} = 10^8$.

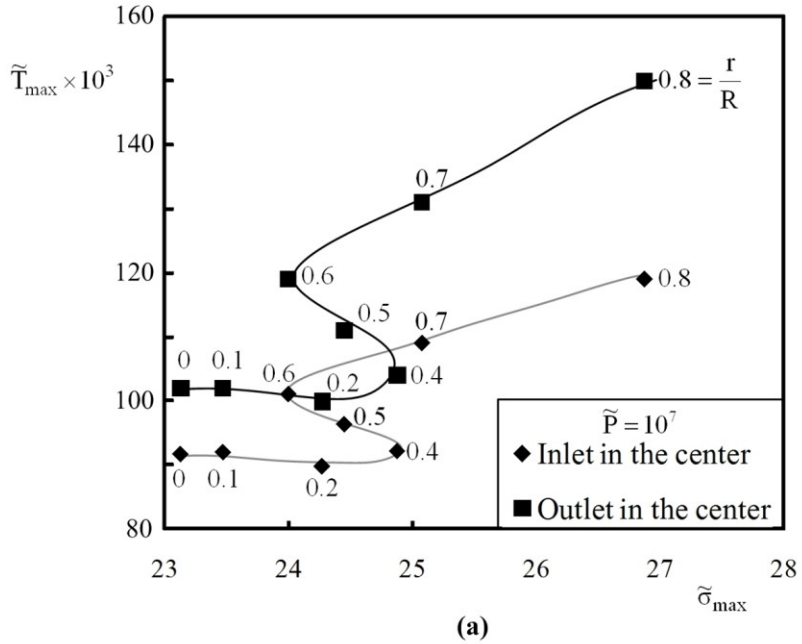

(a)

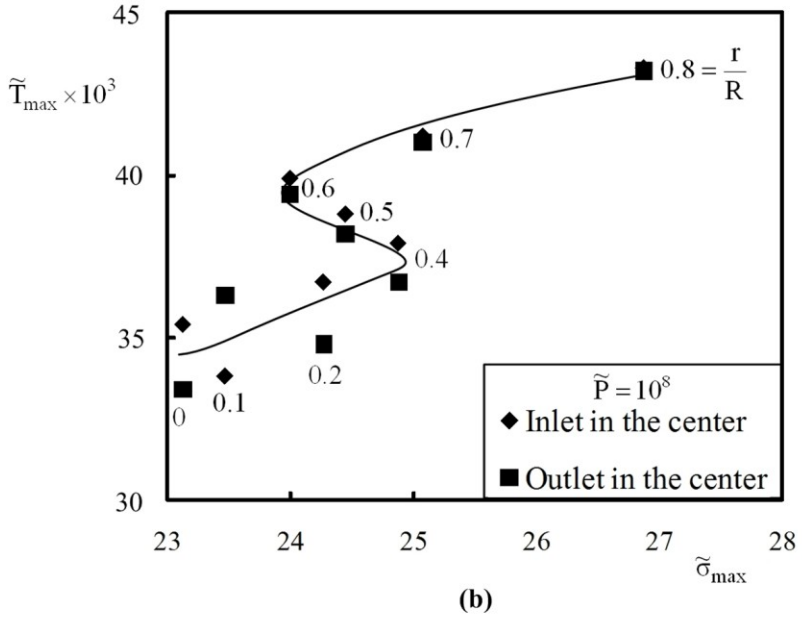

(b)

Figure 3.6: The effect of r/R ratio on the maximum temperature and stress: (a) $\widetilde{P}_{max} = 10^7$**; (b)** $\widetilde{P}_{max} = 10^8$**.**

and the outlet locations of the d_6 ducts are fixed. We determined the changes in mechanical strength and temperature distribution when the r_1/R and r_2/R ratios change.

Figure 3.7b shows how the temperature distribution changes on the mid plane of the circular disc depending on the r_1/R and r_2/R ratios and inlet direction of the coolant, $\widetilde{P}_{max} = 10^8$. Figures 3.8a-d show how the maximum stress and temperature of the structure change according to r_1/R and r_2/R when $\widetilde{P}_{max}$ is 10^7 and 10^8. The maximum stress increases when r_1/R and r_2/R ratios increase, and after the maximum it tends to decrease to a minimum. The maximum temperature occurs on the rim, half way between the ducts of the diameter d_6. When r_1/R is fixed and r_2/R increases, $\widetilde{T}_{max}$ decreases until $r_2/R = 0.3$ or 0.4 depending on r_1/R, and then $\widetilde{T}_{max}$ increases. Similarly, when r_2/R is fixed and r_1/R increases, $\widetilde{T}_{max}$ decreases until $r_1/R = 0.3$ or 0.4 and then it increases. When $\widetilde{P}_{max} = 10^8$ and coolant fluid enters from the rim of the plate, we see that $\widetilde{T}_{max}$ increases when r_1/R or r_2/R increase.

Figure 3.9 shows how $\widetilde{T}_{max}$ changes when r_1/R and r_2/R vary if the coolant fluid enters from the center. This inlet position assures a lower $\widetilde{T}_{max}$ than the outlet in the center. Figure 3.10 shows how the coolant flow rate varies with the geometric configuration; radial, dendrites with one pairing level, and dendrites with two pairing levels. The flow rate $\tilde{m}$ is the volumetric flow rate for the dimensionless velocity,

$$\tilde{m} = \int \widetilde{W} dS \tag{3.41}$$

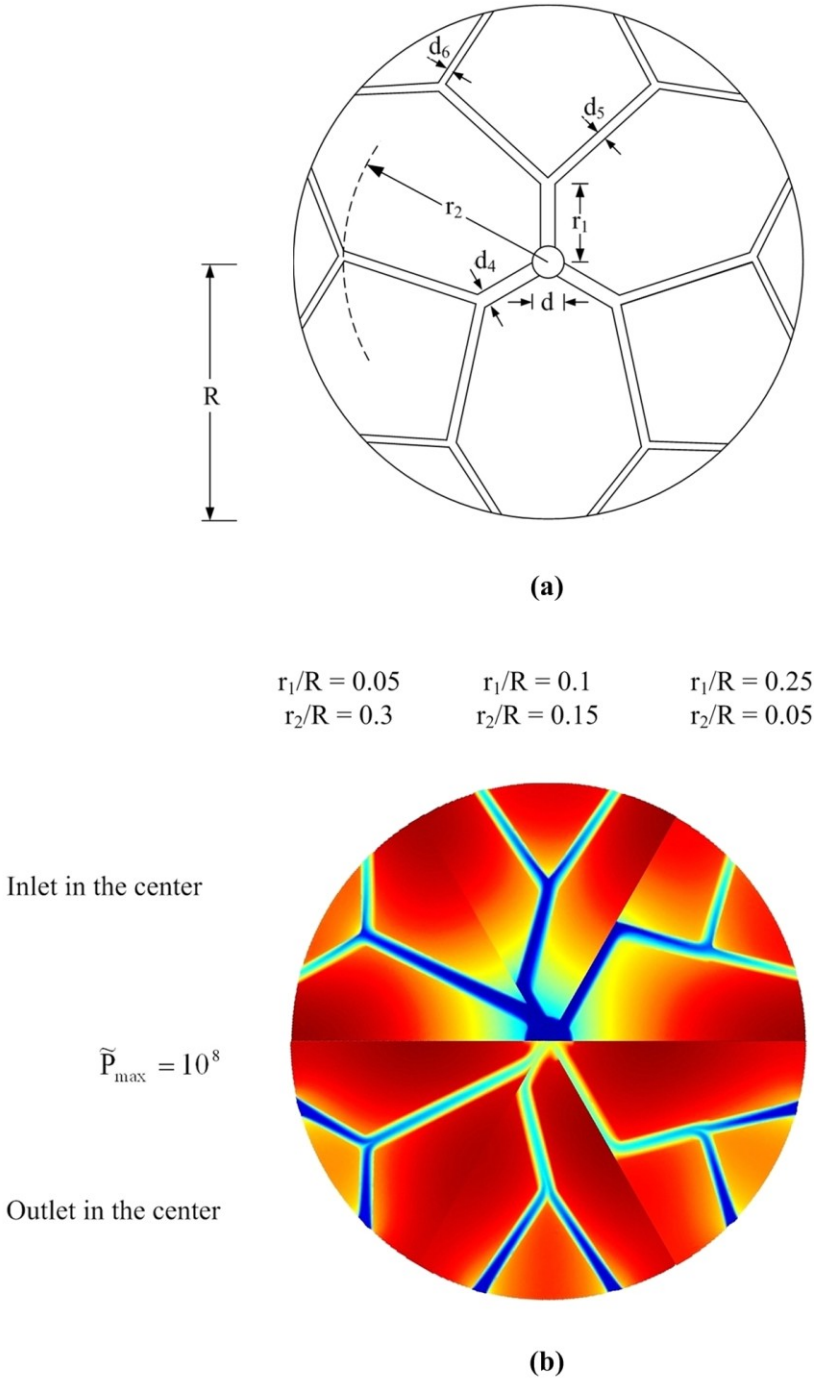

Figure 3.7: (a) Dendritic design with two level of pairing; (b) The temperature distribution in the mid plane of the circular disc, $\widetilde{P}_{max} = 10^8$.

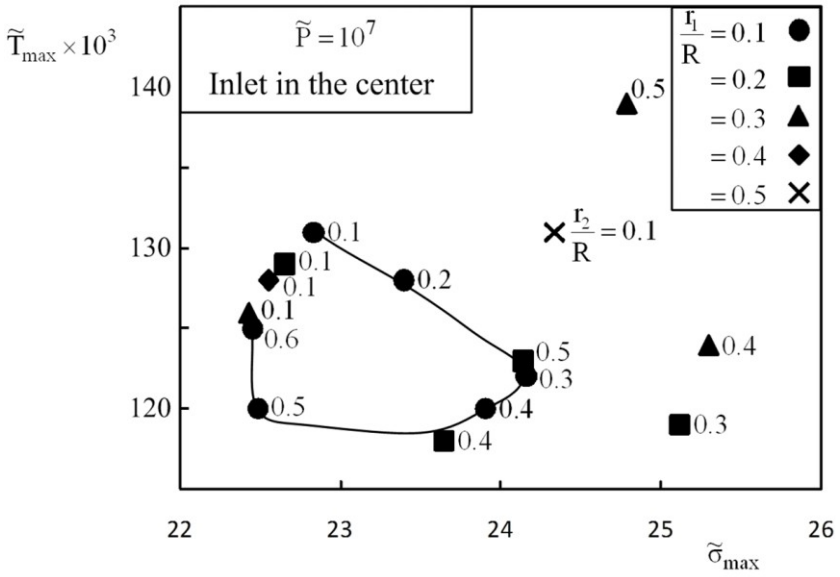

(a)

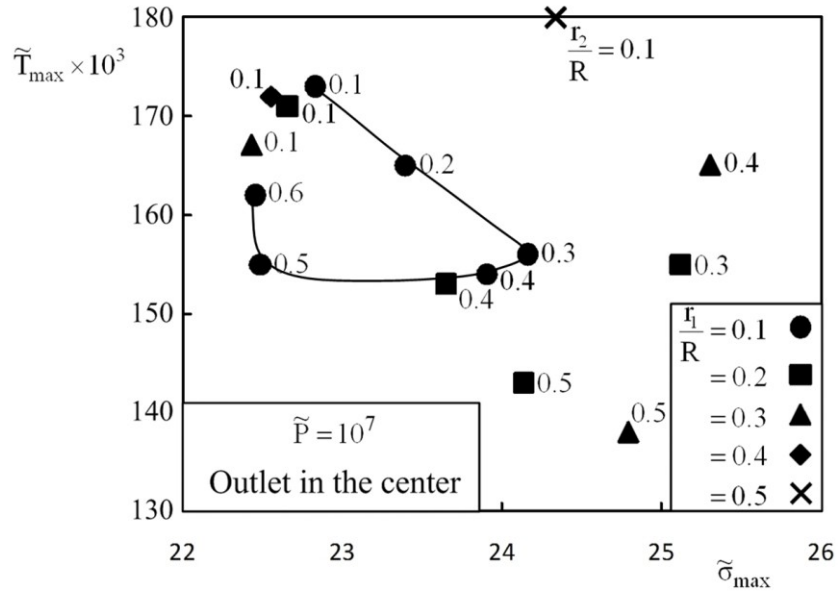

(b)

Figure 3.8 a, b: The effect of r_1/R and r_2/R ratios on the maximum temperature and stress in the configuration of Fig. 2.7, $\widetilde{P}_{max} = 10^7$.

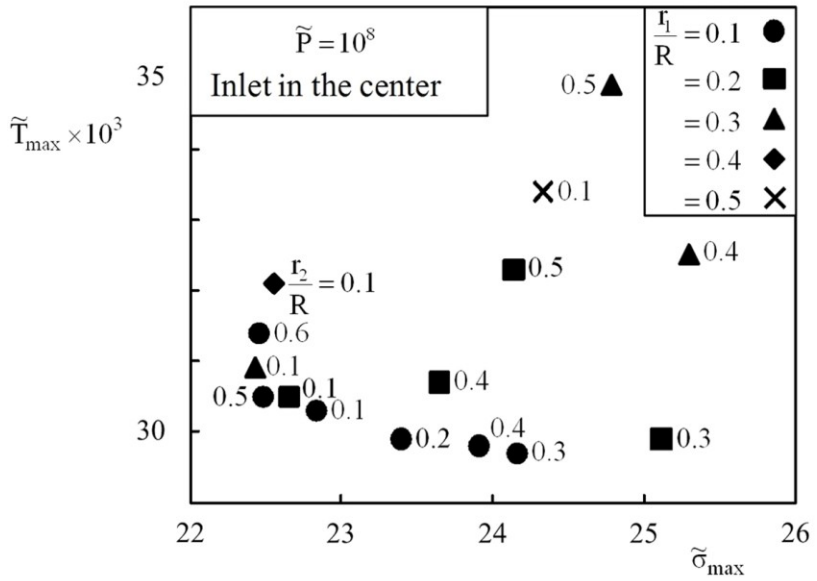

(c)

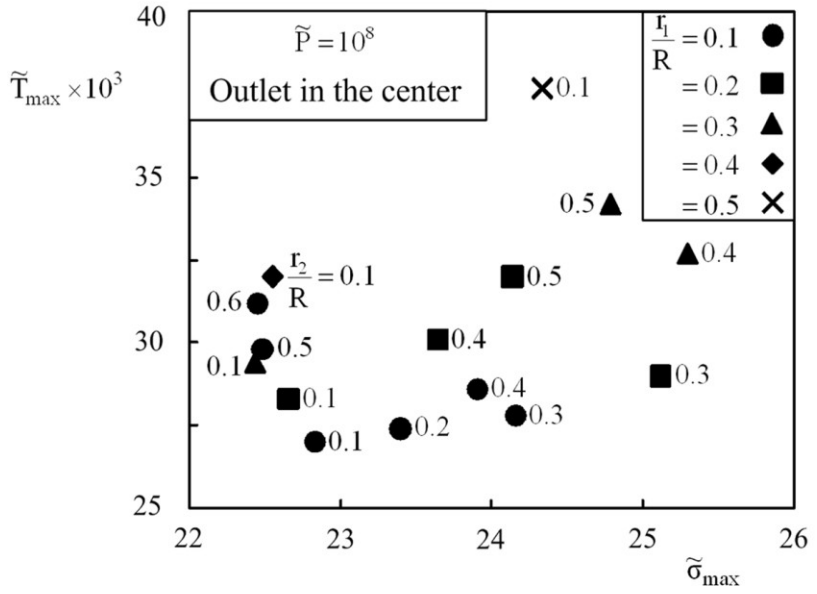

(d)

Figure 3.8 c, d: The effect of r_1/R and r_2/R ratios on the maximum temperature and stress in the configuration of Fig. 2.7, $\widetilde{P}_{max}=10^8$.

where $\widetilde{W}$ is the normal nondimensional velocity of the fluid, and dS is the surface element of the inlet or outlet boundary. The surface integral of $\widetilde{W}$ over the boundary gives the volumetric flow rate for the incompressible flow case, i.e. gases under Mach number 0.3 [48] and liquids. The radial configuration with the six cooling ducts can be seen as one limiting case of the one pairing level configuration. Similarly, the radial configuration with 12 cooling ducts can be seen as one extreme of the configuration with the two pairing levels.

Figure 3.10 shows that when the number of the cooling ducts is 6, the radial configuration ensures higher flow rates than the tree shaped structure. However, the comparison between the radial configuration (n = 12) and the design with two pairing levels shows that tree shaped architectures offer smaller pressure drops than the radial configurations when the number of the cooling ducts is sufficiently high. If the number of the ducts increases, a lower pressure drop can be achieved by changing from the radial configuration to the tree shaped configuration. Noteworthy is that in tree shaped configurations with maximum flow rate the angle between the two branches has values in the range $68^{\circ} - 86^{\circ}$, which confirms the 75-degree-angle found in Ref. [15].

3.6 Discussion

In this chapter we showed that the mechanical strength and cooling performance of a circular plate can be improved simultaneously by changing the flow architecture and the flow direction of the coolant. We explored three configurations: radial, dendrites with

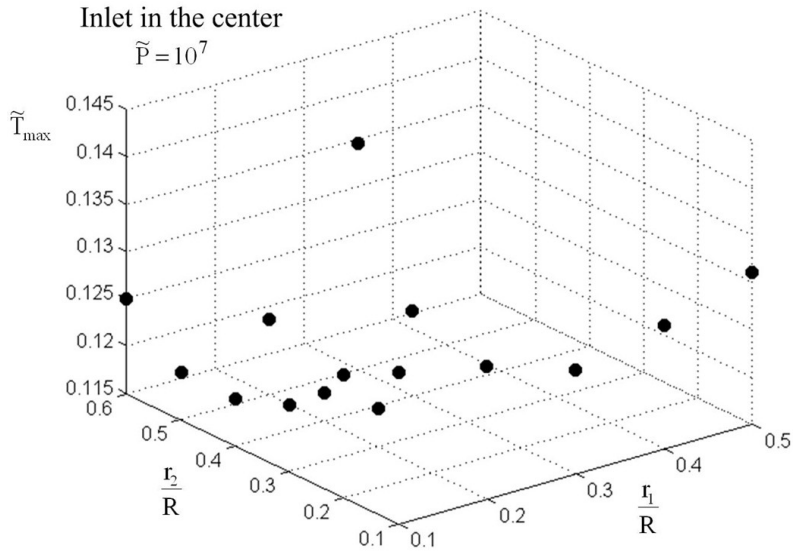

(a)

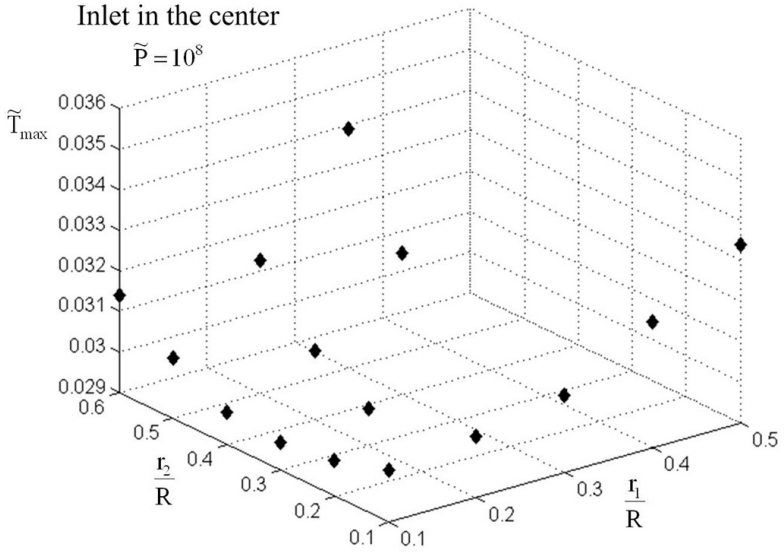

(b)

Figure 3.9: Peak temperature versus r_1/R and r_2/R when the coolant fluid enters from the center of the plate:(a) $\widetilde{P}_{max} = 10^7$; (b) $\widetilde{P}_{max} = 10^8$.

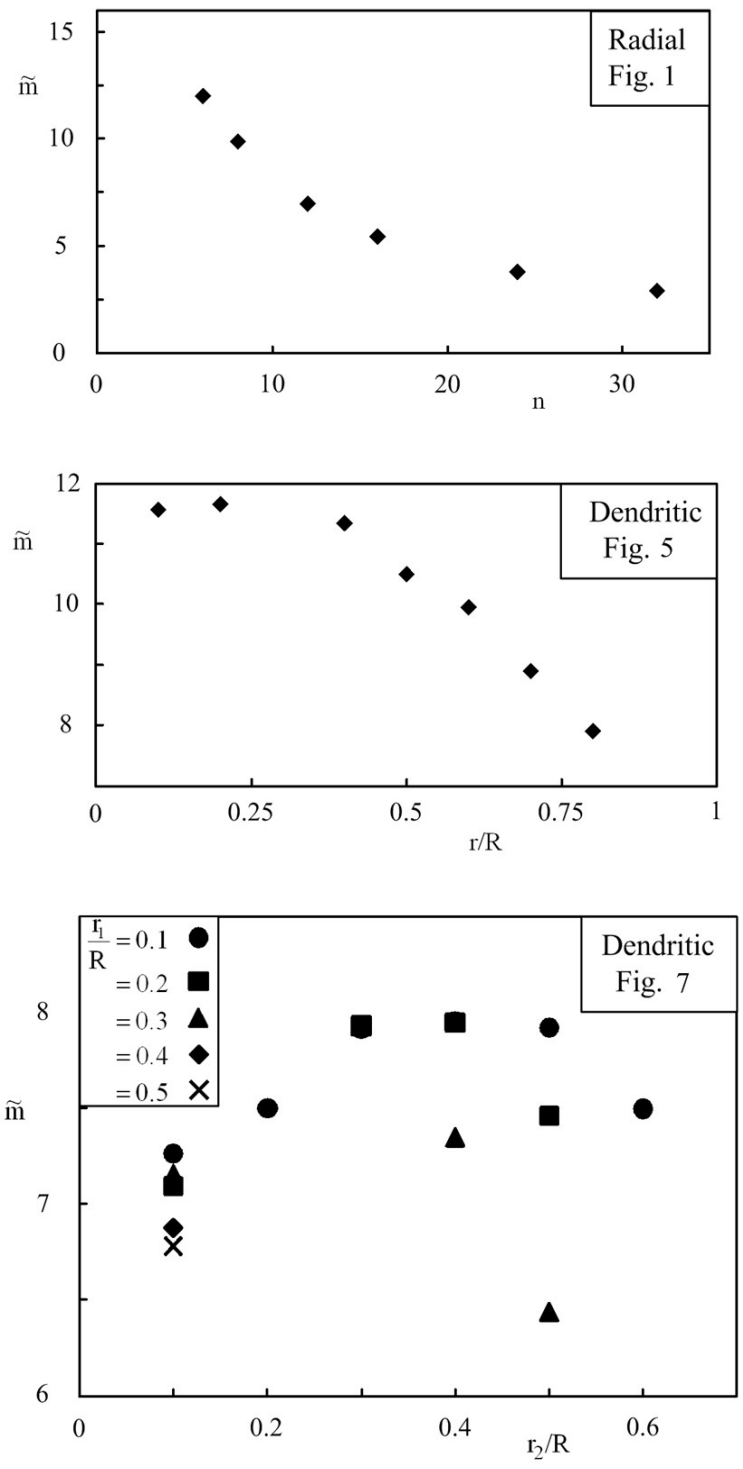

Figure 3.10: The effect of geometry on the total flow rate, $\tilde{P}_{max} = 10^8$.

one pairing level and dendrites with two pairing levels. We found optimal configurations for each given set of design variables. When the size of the system increases, decreases in the pumping power are achieved by changing from radial to dendritic configurations. Similarly, dendritic structures ensure greater mechanical strength when the number of the cooling ducts and the size of the system increase.

The chief conclusion is that the cooling performance and mechanical strength can be increased with embedded vascular channels. An added benefit of using embedded channels is the more uniform temperature field, which increases the yield strength of the structure. The vasculature inhibits the formation of temperature peaks in the material, reduces the differential thermal expansion, and lowers the thermal stresses.

4. Hybrid grid & tree structures for cooling and mechanical strength

Advanced technologies require materials, structures and components that offer multiple functionalities at the same time, for example, volumetric cooling, volumetric self-healing, minimum weight, and mechanical strength [15]. Cooling and self-healing can be achieved by embedding vascular networks of channels in the solid. This feature decreases the mechanical strength of the vascularized body when solid material is removed in order to make room for flow channels. On the other hand, when the volume of solid is fixed, embedding the channels is equivalent to placing the finite solid around the finite flow space. The design opportunity is to allocate the solid where it is needed the most, such that the entire vascular body is as strong as possible.

Vascular design is a growing area in the current literature. Most of this activity is dedicated to the thermal and fluid flow merits of vascularization [35-39, 49-60]. The same design philosophy is now being extended to the design of solid structures to facilitate the flow of stresses [15, 34, 44-45, 61]. In this paper we combine the two methods and consider simultaneously the flow of fluid, heat and stresses.

We explore the merits of a novel "hybrid" architecture consisting of an internal grid connected by radial channels to the perimeter of the vascularized body. Each radial channel serves as the trunk of the tree for which the canopy is the grid. The grid can be viewed as the superposition of the canopies of the trees rooted in the perimeter of the body, Fig. 4.1. The key question in this design is to determine the most advantageous

balance between the volume occupied by the grid and the volume occupied by the radial channels.

4.1 Model

Consider a square plate with length L, thickness H = 0.1L, and embedded cooling channels (Fig. 4.2). The plate is subjected to a uniformly distributed force acting from below, and it is heated uniformly. The volume of the structure and the flow volume are fixed. The flow volume is 5% of the total volume. L_g is the side of the square area in which the grid cooling channels are embedded. The grid channels are connected to the periphery with radial channels. Coolant enters or exits from the center of the grid, and it is driven by the pressure difference maintained between the inlet and outlet. The fluid

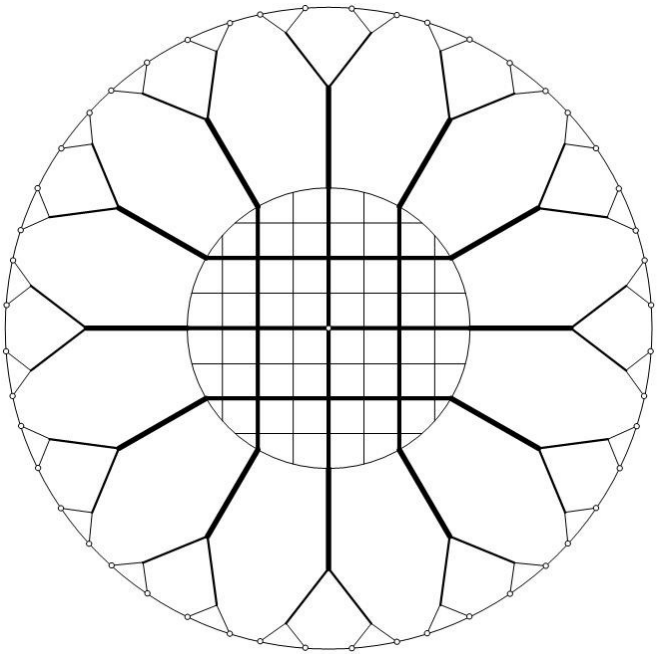

Figure 4.1: Internal grid structure connected to the perimeter with radial channels, hybrid structure of a circular plate.

flow is governed by the mass conservation and momentum equations, which for incompressible and steady flow are

$$\frac{\partial u}{\partial x}+\frac{\partial v}{\partial y}+\frac{\partial w}{\partial z}=0 \tag{4.1}$$

$$u\frac{\partial u}{\partial x}+v\frac{\partial u}{\partial y}+w\frac{\partial u}{\partial z}=-\frac{1}{\rho}\frac{\partial P}{\partial x}+\nu\nabla^2 u \tag{4.2}$$

$$u\frac{\partial v}{\partial x}+v\frac{\partial v}{\partial y}+w\frac{\partial v}{\partial z}=-\frac{1}{\rho}\frac{\partial P}{\partial y}+\nu\nabla^2 v \tag{4.3}$$

$$u\frac{\partial w}{\partial x}+v\frac{\partial w}{\partial y}+w\frac{\partial w}{\partial z}=-\frac{1}{\rho}\frac{\partial P}{\partial z}+\nu\nabla^2 w \tag{4.4}$$

Here $\nabla^2=\partial^2/\partial x^2+\partial^2/\partial y^2+\partial^2/\partial z^2$; furthermore x, y and z are the spatial coordinates, u, v and w are the velocity components corresponding to these coordinates, and P, ν and ρ are the pressure, kinematic viscosity and fluid density. The fluid is single phase with constant properties.

The temperature distribution is found by solving the energy equation in the fluid space and the solid space,

$$\rho c_P\left(u\frac{\partial T}{\partial x}+v\frac{\partial T}{\partial y}+w\frac{\partial T}{\partial z}\right)=k_f\nabla^2 T \tag{4.5}$$

$$q'''=k_s\nabla^2 T \tag{4.6}$$

where c_P is the specific heat at constant pressure of the fluid, T is the temperature, q''' is the volumetric heating rate, and k_f and k_s are the fluid and solid thermal conductivities. The continuity of heat flux between the solid and fluid interfaces requires

$$k_s \frac{\partial T}{\partial n} = k_f \frac{\partial T}{\partial n} \tag{4.7}$$

where n is the vector normal to the fluid-solid interface.

The solid plate is isotropic with elastic deformations that are small when compared with the dimensions L and H. Volumetric forces are assumed to be negligible when compared with the surface forces. With these simplifications in mind, the momentum equations and generalized Hooke's law become

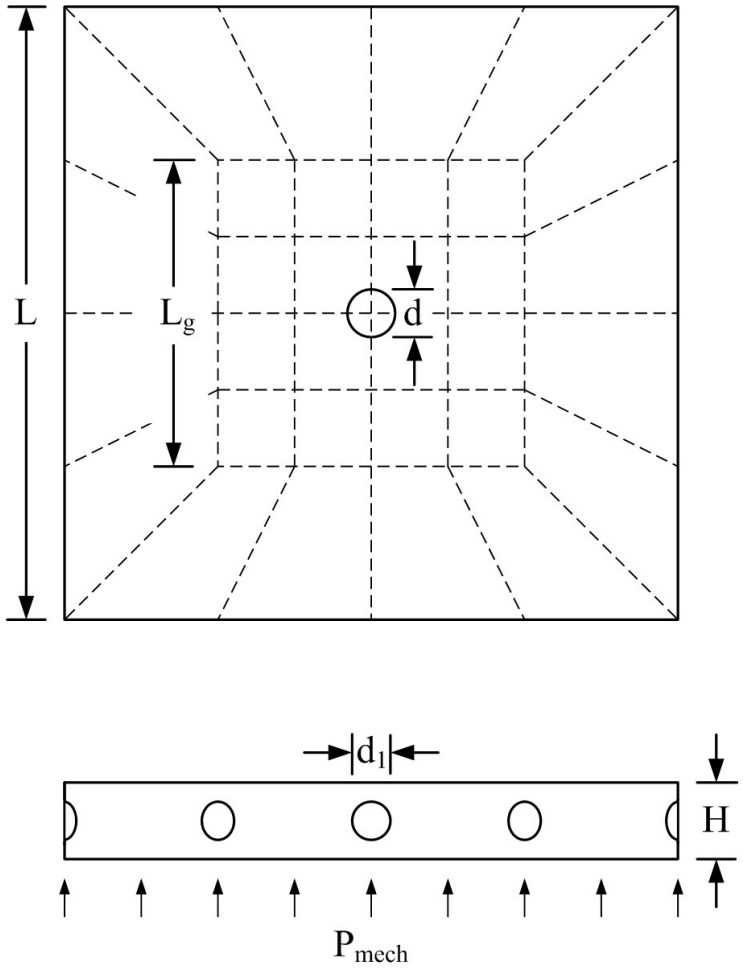

Figure 4.2: Internal grid structure connected to the perimeter with radial channels, hybrid structure of a circular plate.

$$\frac{\partial \sigma_{xx}}{\partial x} + \frac{\partial \tau_{yx}}{\partial y} + \frac{\partial \tau_{zx}}{\partial z} = 0 \tag{4.8}$$

$$\frac{\partial \tau_{xy}}{\partial x} + \frac{\partial \sigma_{yy}}{\partial y} + \frac{\partial \tau_{zy}}{\partial z} = 0 \tag{4.9}$$

$$\frac{\partial \tau_{xz}}{\partial x} + \frac{\partial \tau_{yz}}{\partial y} + \frac{\partial \sigma_{zz}}{\partial z} = 0 \tag{4.10}$$

$$\begin{bmatrix} \sigma_{xx} \\ \sigma_{yy} \\ \sigma_{zz} \\ \tau_{yz} \\ \tau_{zx} \\ \tau_{xy} \end{bmatrix} = \frac{E}{(1+\gamma)(1-2\gamma)} \begin{bmatrix} 1-\gamma & \gamma & \gamma & 0 & 0 & 0 \\ \gamma & 1-\gamma & \gamma & 0 & 0 & 0 \\ \gamma & \gamma & 1-\gamma & 0 & 0 & 0 \\ 0 & 0 & 0 & \frac{(1-2\gamma)}{2} & 0 & 0 \\ 0 & 0 & 0 & 0 & \frac{(1-2\gamma)}{2} & 0 \\ 0 & 0 & 0 & 0 & 0 & \frac{(1-2\gamma)}{2} \end{bmatrix} \begin{bmatrix} \varepsilon_{xx} \\ \varepsilon_{yy} \\ \varepsilon_{zz} \\ \varphi_{yz} \\ \varphi_{zx} \\ \varphi_{xy} \end{bmatrix} \tag{4.11}$$

where γ is the Poisson ratio, and E is the elasticity modulus. The strain displacement relations are

$$\varepsilon_{xx} = \frac{\partial r_x}{\partial x}, \qquad \varepsilon_{yy} = \frac{\partial r_y}{\partial y}, \qquad \varepsilon_{zz} = \frac{\partial r_z}{\partial z} \tag{4.12}$$

$$\varphi_{xy} = \frac{\partial r_x}{\partial y} + \frac{\partial r_y}{\partial x}, \qquad \varphi_{yz} = \frac{\partial r_z}{\partial y} + \frac{\partial r_y}{\partial z}, \qquad \varphi_{zx} = \frac{\partial r_z}{\partial x} + \frac{\partial r_x}{\partial z} \tag{4.13}$$

where r_x, r_y and r_z are the displacements.

Equations (4.1) – (4.4) are nondimensionalized by using L as the length scale, and constructing dimensionless velocities in the form of Reynolds numbers

$$(\tilde{x}, \tilde{y}, \tilde{z}, \tilde{n}) = \frac{(x, y, z, n)}{L}, \qquad \tilde{u} = \frac{uL}{\nu}, \qquad \tilde{v} = \frac{vL}{\nu}, \qquad \tilde{w} = \frac{wL}{\nu} \tag{4.14}$$

The dimensionless pressure difference is defined as [46, 47]

$$\widetilde{P} = \frac{(P - P_{out})L^2}{\mu\alpha} \tag{4.15}$$

where P, P_{out}, μ and α are the local pressure, the outlet pressure, the dynamic viscosity, and the thermal diffusivity of the fluid. The dimensionless temperature and continuity of the heat flux are indicated by

$$\widetilde{T} = \frac{(T - T_{ref})k_f}{q'''L^2} \tag{4.16}$$

$$\widetilde{k}\left.\frac{\partial\widetilde{T}}{\partial\widetilde{n}}\right|_s = \left.\frac{\partial\widetilde{T}}{\partial\widetilde{n}}\right|_f \tag{4.17}$$

where T_{ref} is the fluid inlet temperature and $\widetilde{k} = k_s/k_f$.

Equations (4.8) – (4.11) are nondimensionalized by using L as the length scale for displacements and coordinates, and P_{mech} as the pressure scale for the stresses, elasticity and mechanical load,

$$(\widetilde{r}_x, \widetilde{r}_y, \widetilde{r}_z, \widetilde{x}, \widetilde{y}, \widetilde{z}) = (r_x, r_y, r_z, x, y, z)/L \tag{4.18}$$

$$\widetilde{\varepsilon}_{xx} = \frac{\partial\widetilde{r}_x}{\partial\widetilde{x}}, \qquad \widetilde{\varepsilon}_{yy} = \frac{\partial\widetilde{r}_y}{\partial\widetilde{y}}, \qquad \widetilde{\varepsilon}_{zz} = \frac{\partial\widetilde{r}_z}{\partial\widetilde{z}} \tag{4.19}$$

$$\widetilde{\varphi}_{xy} = \frac{\partial\widetilde{r}_x}{\partial\widetilde{y}} + \frac{\partial\widetilde{r}_y}{\partial\widetilde{x}}, \qquad \widetilde{\varphi}_{yz} = \frac{\partial\widetilde{r}_z}{\partial\widetilde{y}} + \frac{\partial\widetilde{r}_y}{\partial\widetilde{z}}, \qquad \widetilde{\varphi}_{zx} = \frac{\partial\widetilde{r}_z}{\partial\widetilde{x}} + \frac{\partial\widetilde{r}_x}{\partial\widetilde{z}} \tag{4.20}$$

$$(\widetilde{E}, \widetilde{\sigma}, \widetilde{\tau}, \widetilde{P}_{mech}) = (E, \sigma, \tau, P_{mech})/P_{mech} \tag{4.21}$$

where P_{mech} is the pressure applied uniformly from the bottom of the plate. The dimensionless mass conservation and momentum equations are

$$\frac{\partial \tilde{u}}{\partial \tilde{x}} + \frac{\partial \tilde{v}}{\partial \tilde{y}} + \frac{\partial \tilde{w}}{\partial \tilde{z}} = 0 \tag{4.22}$$

$$\tilde{u}\frac{\partial \tilde{u}}{\partial \tilde{x}} + \tilde{v}\frac{\partial \tilde{u}}{\partial \tilde{y}} + \tilde{w}\frac{\partial \tilde{u}}{\partial \tilde{z}} = -\frac{1}{Pr}\frac{\partial \tilde{P}}{\partial \tilde{x}} + \nabla^2 \tilde{u} \tag{4.23}$$

$$\tilde{u}\frac{\partial \tilde{v}}{\partial \tilde{x}} + \tilde{v}\frac{\partial \tilde{v}}{\partial \tilde{y}} + \tilde{w}\frac{\partial \tilde{v}}{\partial \tilde{z}} = -\frac{1}{Pr}\frac{\partial \tilde{P}}{\partial \tilde{y}} + \nabla^2 \tilde{v} \tag{4.24}$$

$$\tilde{u}\frac{\partial \tilde{w}}{\partial \tilde{x}} + \tilde{v}\frac{\partial \tilde{w}}{\partial \tilde{y}} + \tilde{w}\frac{\partial \tilde{w}}{\partial \tilde{z}} = -\frac{1}{Pr}\frac{\partial \tilde{P}}{\partial \tilde{z}} + \nabla^2 \tilde{w} \tag{4.25}$$

where Pr is Prandtl number. The dimensionless energy equation for the fluid and solid domains are

$$Pr\left(\tilde{u}\frac{\partial \tilde{T}}{\partial \tilde{x}} + \tilde{v}\frac{\partial \tilde{T}}{\partial \tilde{y}} + \tilde{w}\frac{\partial \tilde{T}}{\partial \tilde{z}}\right) = \nabla^2 \tilde{T} \tag{4.26}$$

$$\tilde{k}\nabla^2 \tilde{T} = 1 \tag{4.27}$$

The dimensionless momentum equation and Hooke's law for the solid domain are

$$\frac{\partial \tilde{\sigma}_{xx}}{\partial \tilde{x}} + \frac{\partial \tilde{\tau}_{yx}}{\partial \tilde{y}} + \frac{\partial \tilde{\tau}_{zx}}{\partial \tilde{z}} = 0 \tag{4.28}$$

$$\frac{\partial \tilde{\tau}_{xy}}{\partial \tilde{x}} + \frac{\partial \tilde{\sigma}_{yy}}{\partial \tilde{y}} + \frac{\partial \tilde{\tau}_{zy}}{\partial \tilde{z}} = 0 \tag{4.29}$$

$$\frac{\partial \tilde{\tau}_{xz}}{\partial \tilde{x}} + \frac{\partial \tilde{\tau}_{yz}}{\partial \tilde{y}} + \frac{\partial \tilde{\sigma}_{zz}}{\partial \tilde{z}} = 0 \tag{4.30}$$

$$\begin{bmatrix} \tilde{\sigma}_{xx} \\ \tilde{\sigma}_{yy} \\ \tilde{\sigma}_{zz} \\ \tilde{\tau}_{yz} \\ \tilde{\tau}_{zx} \\ \tilde{\tau}_{xy} \end{bmatrix} = \frac{\tilde{E}}{(1+\gamma)(1-2\gamma)} \begin{bmatrix} 1-\gamma & \gamma & \gamma & 0 & 0 & 0 \\ \gamma & 1-\gamma & \gamma & 0 & 0 & 0 \\ \gamma & \gamma & 1-\gamma & 0 & 0 & 0 \\ 0 & 0 & 0 & \frac{(1-2\gamma)}{2} & 0 & 0 \\ 0 & 0 & 0 & 0 & \frac{(1-2\gamma)}{2} & 0 \\ 0 & 0 & 0 & 0 & 0 & \frac{(1-2\gamma)}{2} \end{bmatrix} \begin{bmatrix} \tilde{\varepsilon}_{xx} \\ \tilde{\varepsilon}_{yy} \\ \tilde{\varepsilon}_{zz} \\ \tilde{\varphi}_{yz} \\ \tilde{\varphi}_{zx} \\ \tilde{\varphi}_{xy} \end{bmatrix} \tag{4.31}$$

4.2. Trees with loops: one degree of freedom

Consider the geometry of Fig. 4.2, which has cooling channels of one size (d_1). The pressure difference between the inlet and outlet is defined as [46, 47].

$$P_{max} = \frac{(P_{in} - P_{ref})L^2}{\mu\alpha} \tag{4.32}$$

The outlet pressure (P_{ref}) is 0, while P_{max} is of order 10^7 – 10^8. This P_{max} range corresponds to laminar flow, i.e. Reynolds numbers less than 2000 in all configurations. We also set $\tilde{k} = 20$, Pr = 6, $\gamma = 0.33$ and $\tilde{E} = 2\times10^6$.

The dimensionless mass, momentum and energy equations were solved by using a finite element software [29]. The mesh was refined after each solution, and the problem was solved again to see whether the solution is mesh dependent. This was repeated by increasing in steps of 50% the number of mesh elements until the solution changed by less than 1%.

Figure 4.3 shows how the flow resistance changes when the relative grid size L_g/L varies ($P_{max} = 10^8$). Six hybrid configurations were simulated, with L_g / L values in the

range 0 – 0.75. Because of the incompressible flow model, the volumetric flow rate is equivalent to the mass flow rate,

$$\dot{m} = \rho \int_S \tilde{V} dS \tag{4.33}$$

where S is the the cross section of the opening in the center of the grid through which the fluid enters to the vascular network or leaves from it, and $\tilde{V}$ is the normal nondimensional velocity of the fluid. Figure 4.3 shows that the flow resistance increases as L_g/L increases. In conclusion, if the sole objective is to decrease the pressure drop or the pumping power requirement, the radial configuration is the better design for the given design parameters. Figure 4.3 also shows that changing the flow direction has an effect on the overall flow resistance: the lower resistance is when the inlet in the center. This effect becomes less pronounced as L_g/L increases.

Figures 4.4a,b show the evolution of the peak temperature of the square slab when L_g/L varies ($P_{max} = 10^7$ and 10^8). The radial configuration ($L_g/L = 0$) with the inlet in the center offers the smallest peak temperature. In both figures, the effect of the fluid flow direction decreases as P_{max} increases.

Figure 4.5 is a cross-plot of Figs. 4.3b and 4.4b, which shows how the peak temperature changes and the flow resistance respond to changes in the relative size of the grid, L_g/L. Both T_{peak} and $P_{max}/\dot{m}$ decrease toward the radial design in the lower-left corner.

Figure 4.6 shows the temperature distribution in the mid plane of the square slab; red and blue represent the maximum and minimum temperatures. Six different cases are shown: L_g/L = 0, 0.25 and 0.5 with inlet and outlet in the center. When the fluid enters through the center of the slab, the hot spots are located at the corners of the square slab. When the coolant enters from the edge, the hot spot is in the center of the square slab.

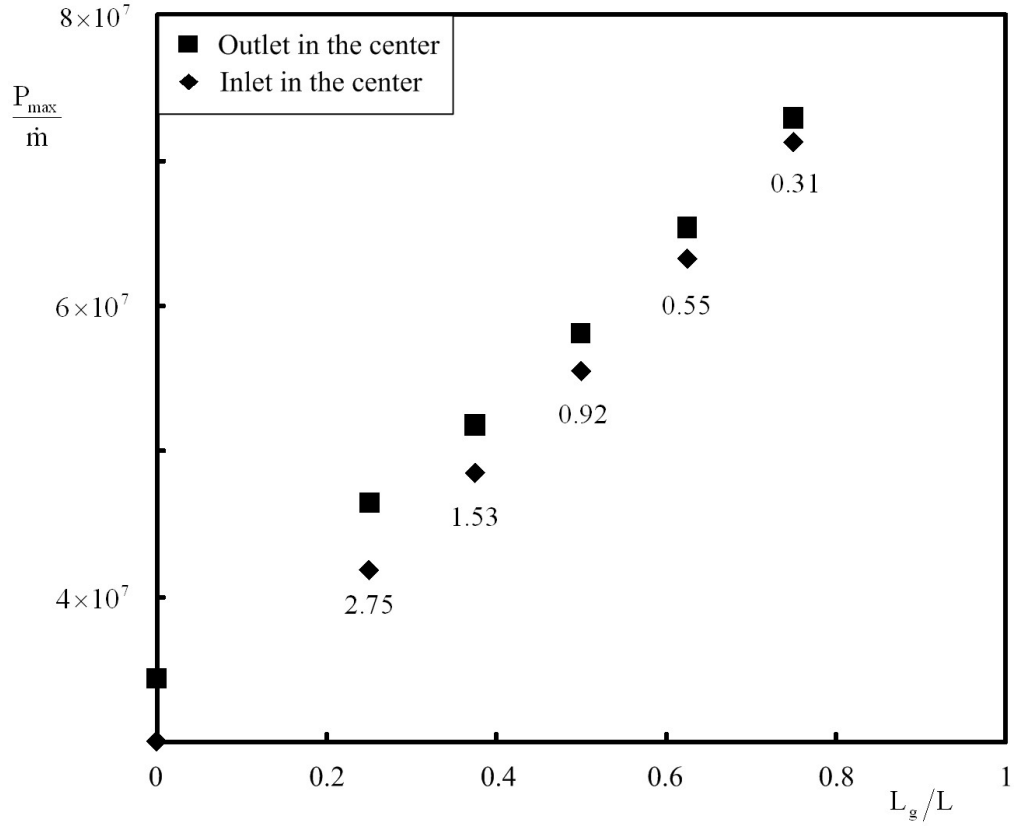

Figure 4.3: Flow resistance of the hybrid structure relative to L_g/L, $P_{max} = 10^8$.

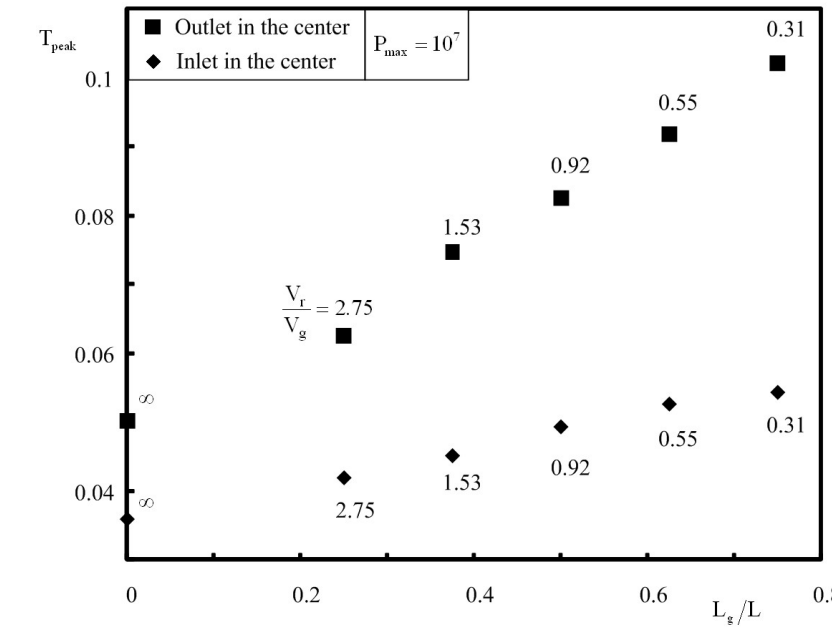

(a)

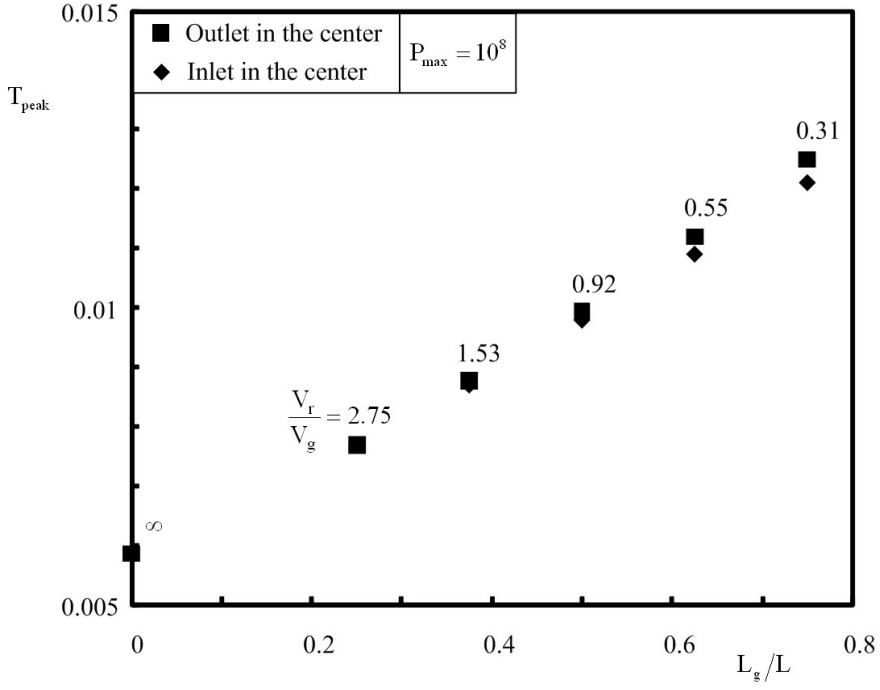

(b)

Figure 4.4: Peak temperature relative to L_g/L: (a) $P_{max} = 10^7$, (b) $P_{max} = 10^8$.

The evolution of stresses is shown in Figs. 4.7a,b, alongside the evolution of the peak temperatures. The peak stresses are the lowest when the configuration is a hybrid grid & tree structure.

4.3. Trees with loops: two degree of freedom

Consider next the impact of a new degree of freedom: the ratio of the fluid volume occupied by the radial part divided by the grid part of the fluid volume, V_r/V_g. The dimensionless mass, momentum, and energy equations were solved for several V_r/V_g values. The fluid volume ($V_r + V_g$) is 5% of the total volume.

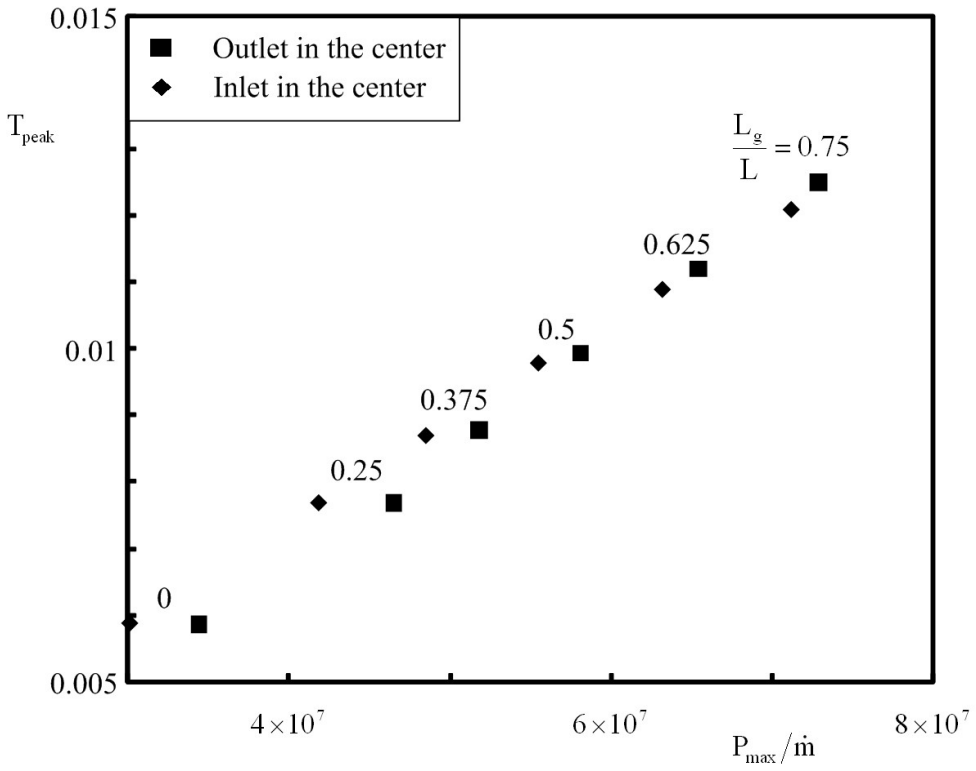

Figure 4.5: Peak temperature relative to the flow resistance, $P_{max} = 10^8$.

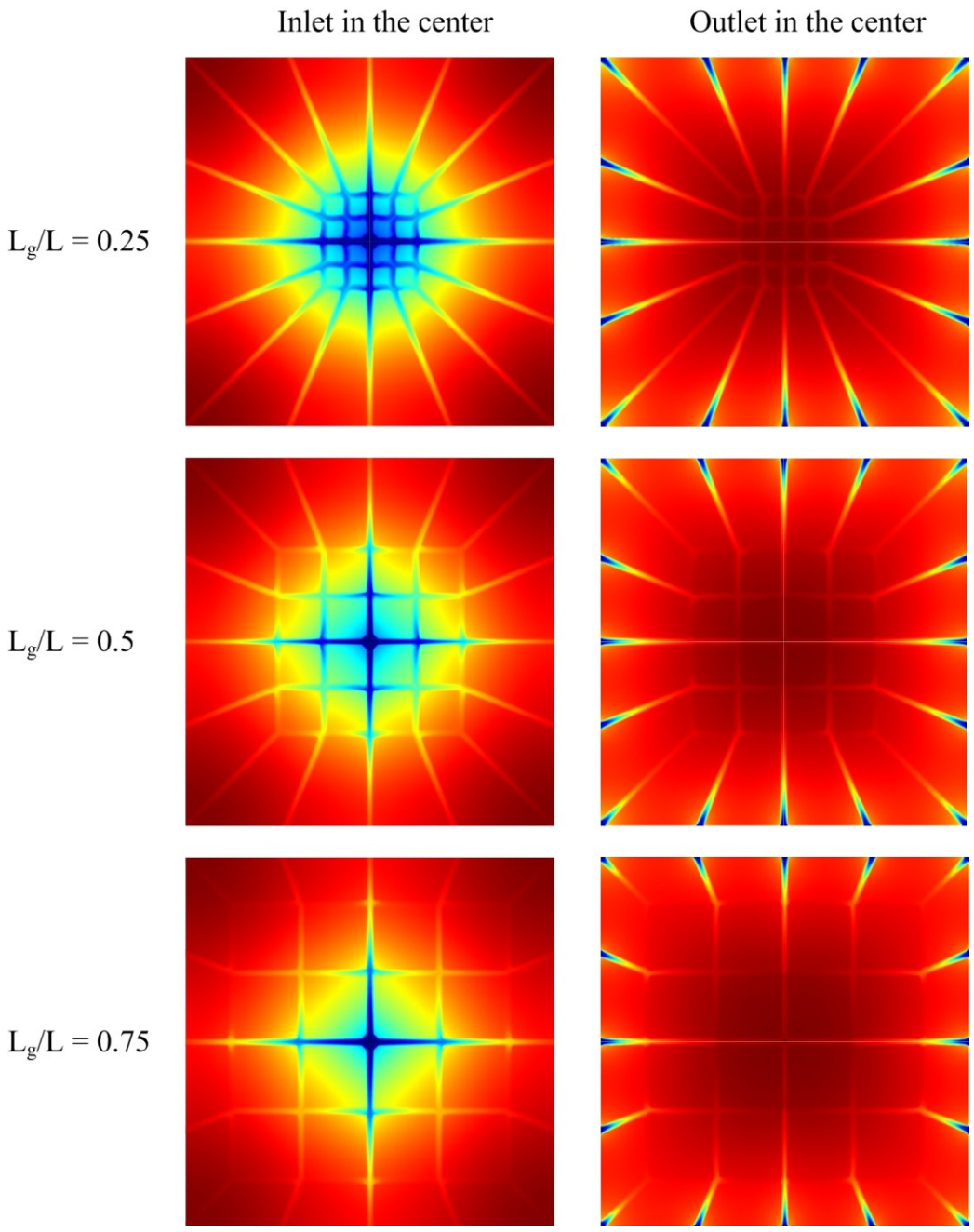

Figure 4.6: The temperature distribution in the mid plane of the square plate, red and blue represent the maximum and minimum temperature, respectively, $P_{max} = 10^8$: (b) L_g/L = 0.25, 0.5 and 0.75.

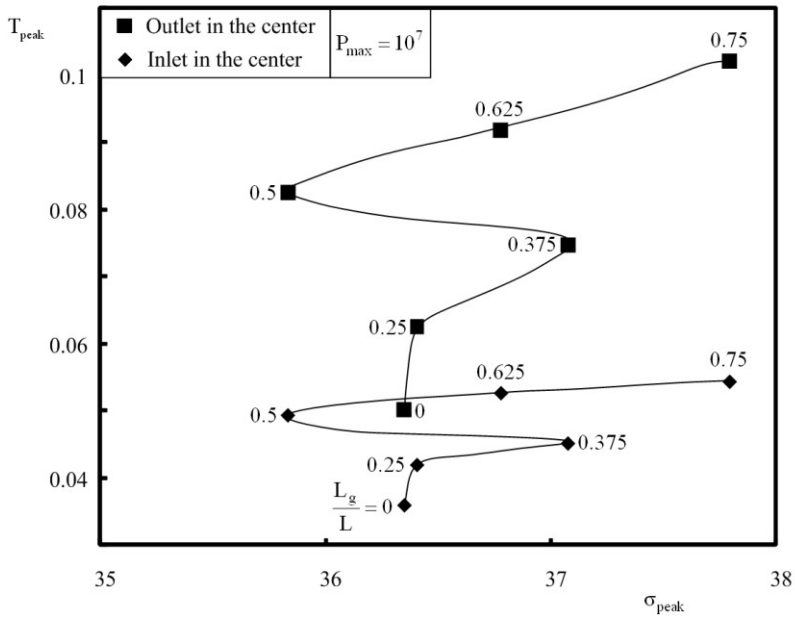

(a)

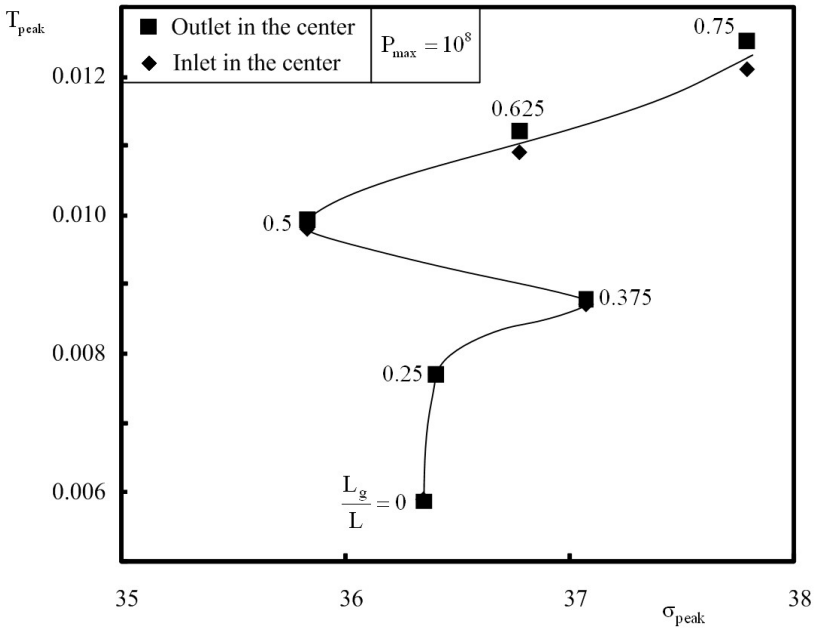

(b)

Figure 4.7: Peak temperature relative to the peak stress: (a) $P_{max} = 10^7$**, (b)** $P_{max} = 10^8$**.**

Figures 4.8a, b show how the peak temperature varies relative to the L_g/L and V_r/V_g ratios. The flow inlet is in the center. When $V_r/V_g > 1$, the peak temperature increases as L_g/L increases. However, when $V_r/V_g < 1$, the peak temperature exhibits a minimum as L_g/L increases. In conclusion, there is a hybrid configuration (L_g/L, V_r/V_g) that offers the smallest T_{peak} when $V_r/V_g < 1$. In Figs. 4.8a,b, the smallest T_{peak} occurs at $L_g/L = 0.25$ when $V_r/V_g = 0.7/0.3$.

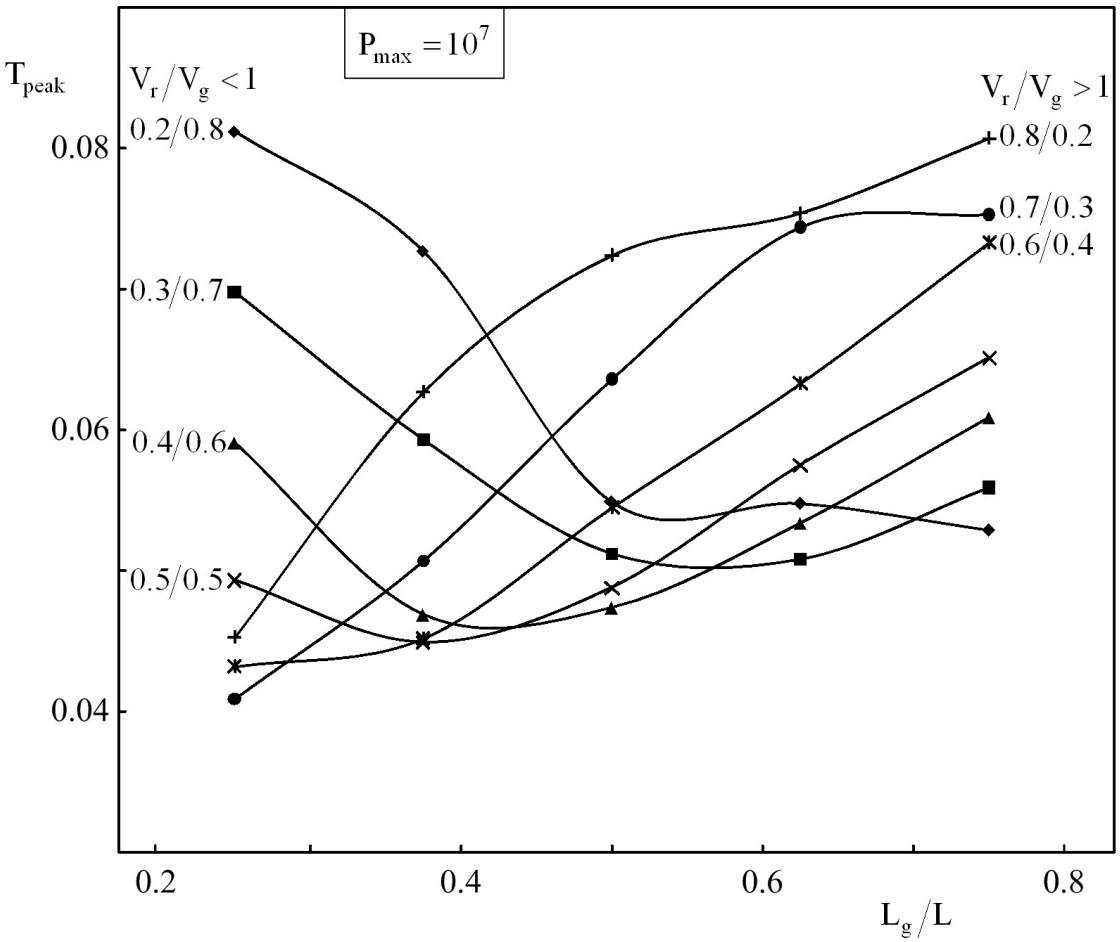

Figure 4.8a: Peak temperatures of the family of V_r/V_g curves relative to L_g/L: $P_{max} = 10^7$.

Figure 4.9 shows the minimum peak temperatures of the Fig. 4.8b plotted against the peak stresses in the same configurations. The effect of the flow direction is weak. The smaller T_{peak} and σ_{peak} values occur when $L_g/L < 0.25$. Optimizing the V_r/V_g value decreases T_{peak} and σ_{peak}, cf. Figs. 4.7b and 4.9. The changes in V_r/V_g affect the peak stress significantly.

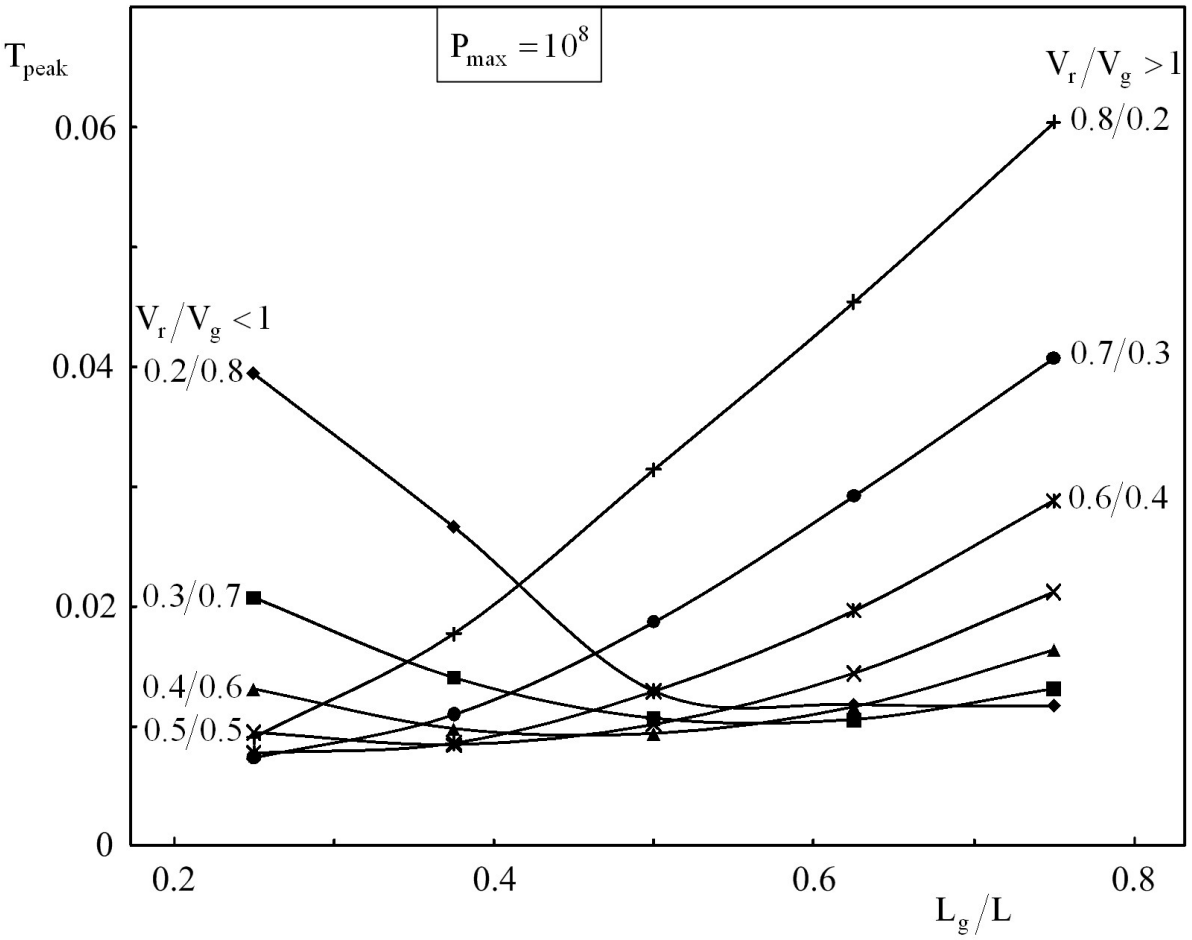

Figure 4.8b: Peak temperatures of the family of V_r/V_g curves relative to L_g/L: $P_{max} = 10^8$.

Figure 4.10 is a montage of six different cases showing the temperature distribution in the mid plane of the square slab. When the flow enters through the center of the slab, the hot spots occur in the corners of the slab. When the flow enters from the edge, the hot spot is in the center of the slab. Figure 4.10 shows that the design with $L_g/L = 0.25$ has a more uniform temperature field with a smaller peak temperature when $V_r/V_g = 0.8/0.2$. The ratio $L_g/L = 0.75$ is the best when $V_r/V_g = 0.2/0.8$.

In Fig. 3.11a, the minimum peak temperatures of Fig. 3.8b are combined with Fig. 3.4b in order to determine how the solution is affected by the second degree of freedom, V_r/V_g. We see that by exploiting this degree of freedom we can decrease the peak temperature while L_g/L is fixed. The effect of the V_r/V_g on the peak temperature increases as L_g/L increases. The peak temperature is smaller when the flow inlet is in the

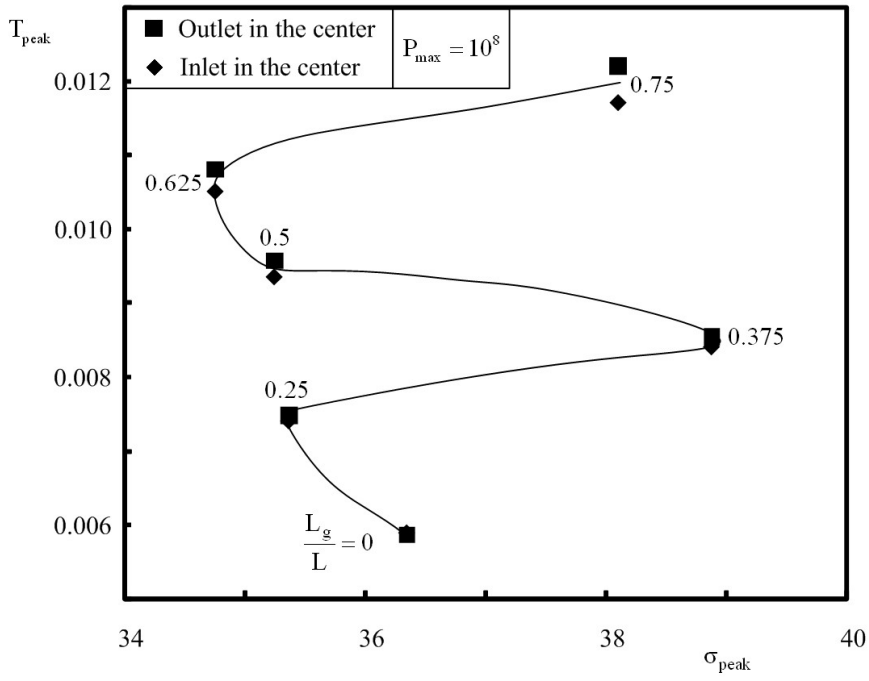

Figure 4.9: Minimum peak temperatures of Fig. 3.8b relative to their peak stresses, $P_{max} = 10^8$.

center.

Figure 4.11b is a combination of Figs. 4.7b and 4.9. It shows that trees with loops have the effect of increasing the strength of the structure. Even though introducing a second degree of freedom (V_r/V_g) does not affect the peak temperature significantly, it affects the peak stresses.

4.4. Concentrated heat generation

An important aspect to consider is the degree of concentration of deposition of heat in the vascularized solid. Until now the heat generation effect was assumed to be uniform. Here we document the effect of concentrating the heat generation in a small area that moves over the solid surface. The area of the heated spot is 1/16 of the square area of length L_g. The heating rate of the concentrated heat generation is fixed.

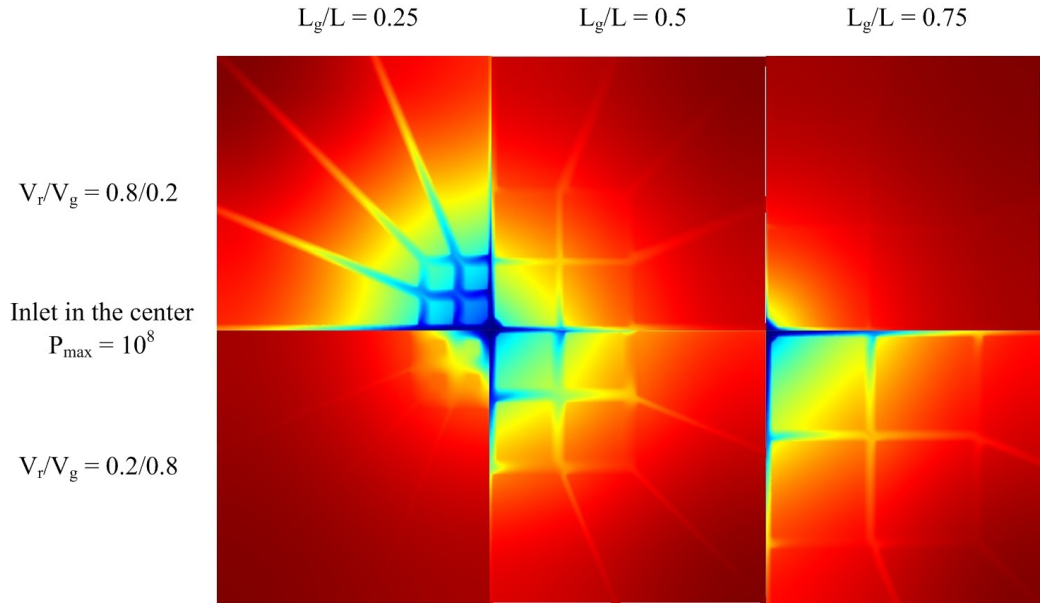

Figure 4.10: The temperature distribution in the mid plane of the square plate when V_r/V_g = 0.8/0.2 and 0.2/0.8, $P_{max} = 10^8$ and L_g/L = 0.25, 0.5 and 0.75.

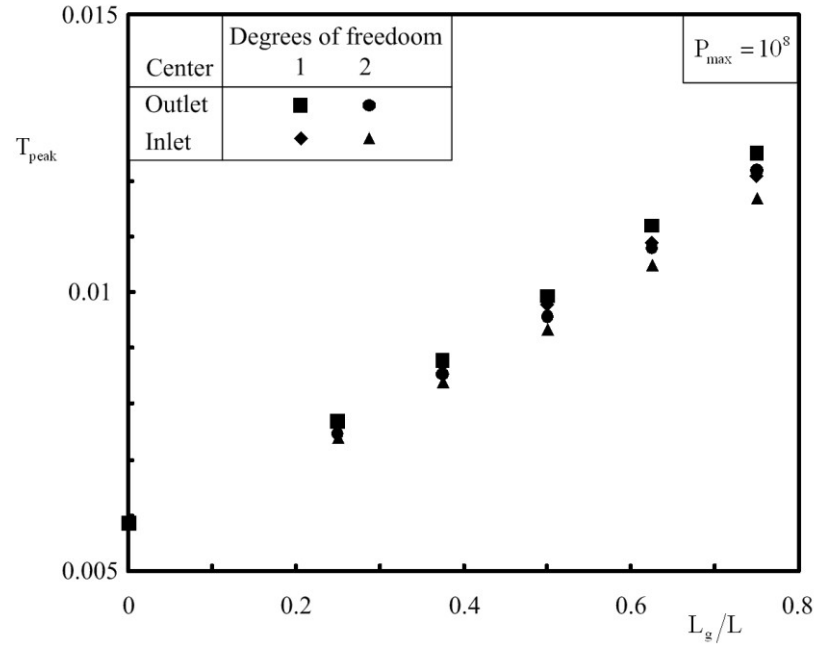

Figure 4.11a: Combination of Fig. 4.4b and the minimum peak temperatures of Fig. 4.8b relative to L_g/L, $P_{max} = 10^8$.

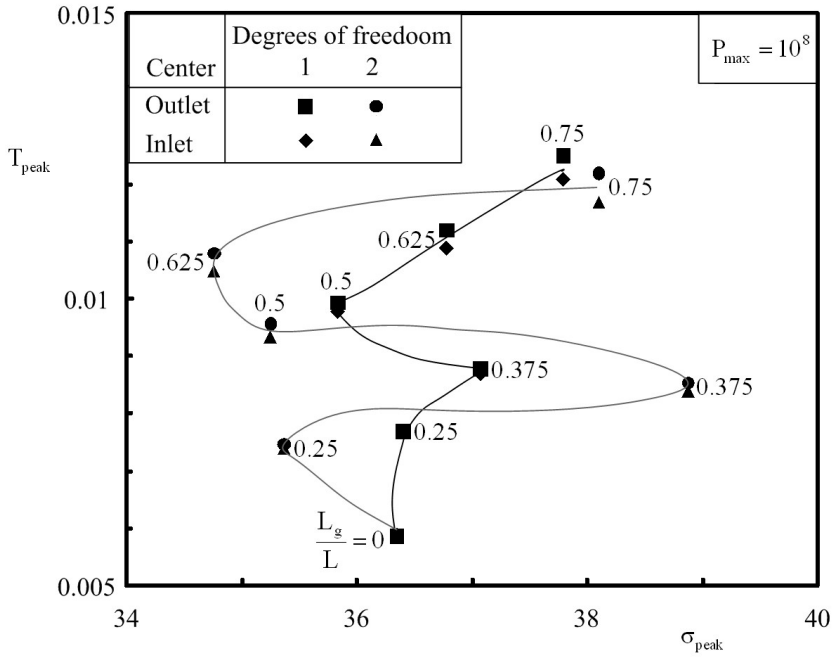

Figure 4.11b: Combination of Figs. 4.7b and 4.9, $P_{max} = 10^8$.

In Fig. 4.12 we show the temperature distribution when the heat generation is concentrated in the center of the slab. Two designs are illustrated, $L_g/L = 0.25$ and 0.5. The flow direction changes from inlet in the center to outlet in the center. The flow direction with inlet in the center offers a more uniform temperature distribution and a smaller peak temperature than the direction with outlet in the center. In addition, as L_g/L increases, the peak temperature decreases and the temperature distribution becomes more uniform.

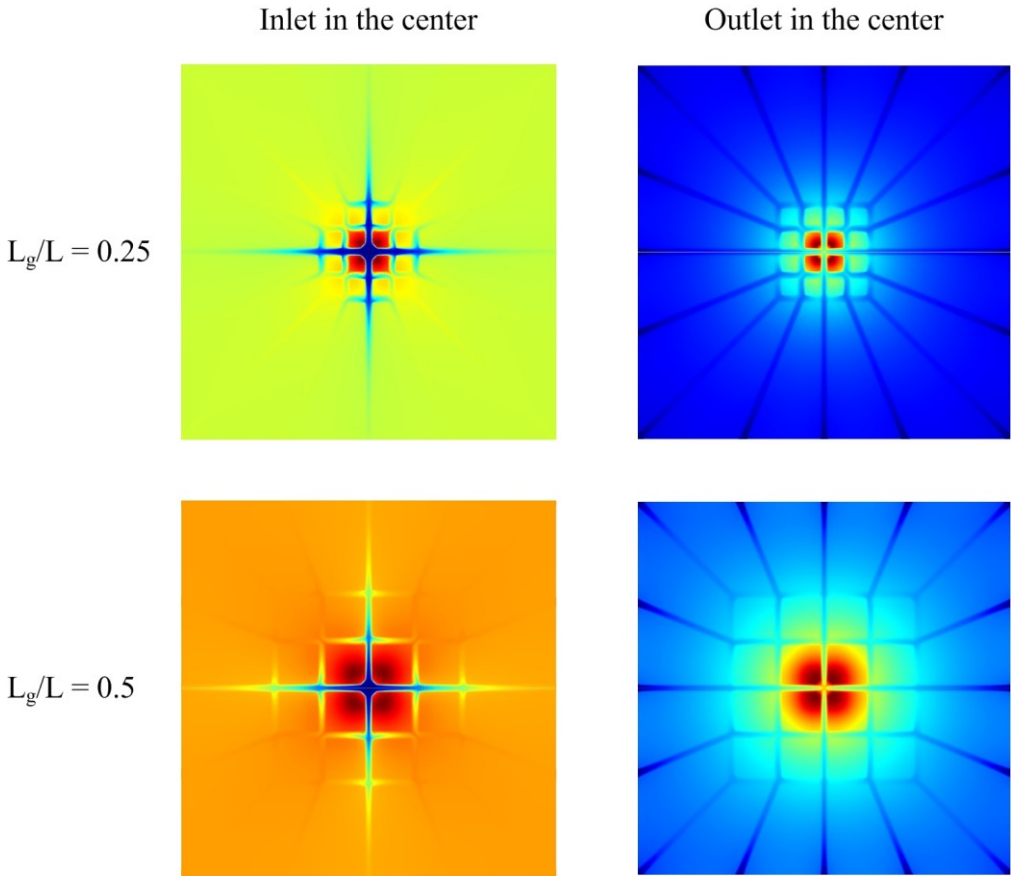

Figure 4.12: The temperature distribution in the mid plane of the square slab when the heat generation is concentrated in the center and $P_{max} = 10^8$.

Figure 4.13 shows what happens when the heat generation rate is concentrated in the lower right corner of the square grid that occupies the center of the design. In Fig. 4.13, the peak temperatures are greater than in Fig. 4.12. The temperature distribution is less uniform in Fig. 4.13 than in Fig. 4.12. These effects are due to the fact that the cold solid volume around the concentrated heated area decreases as L_g/L increases.

Figure 4.14 shows the evolution of the peak temperature as L_g/L increases. When the concentrated heating is located in the center of the slab, T_{peak} decreases as L_g/L

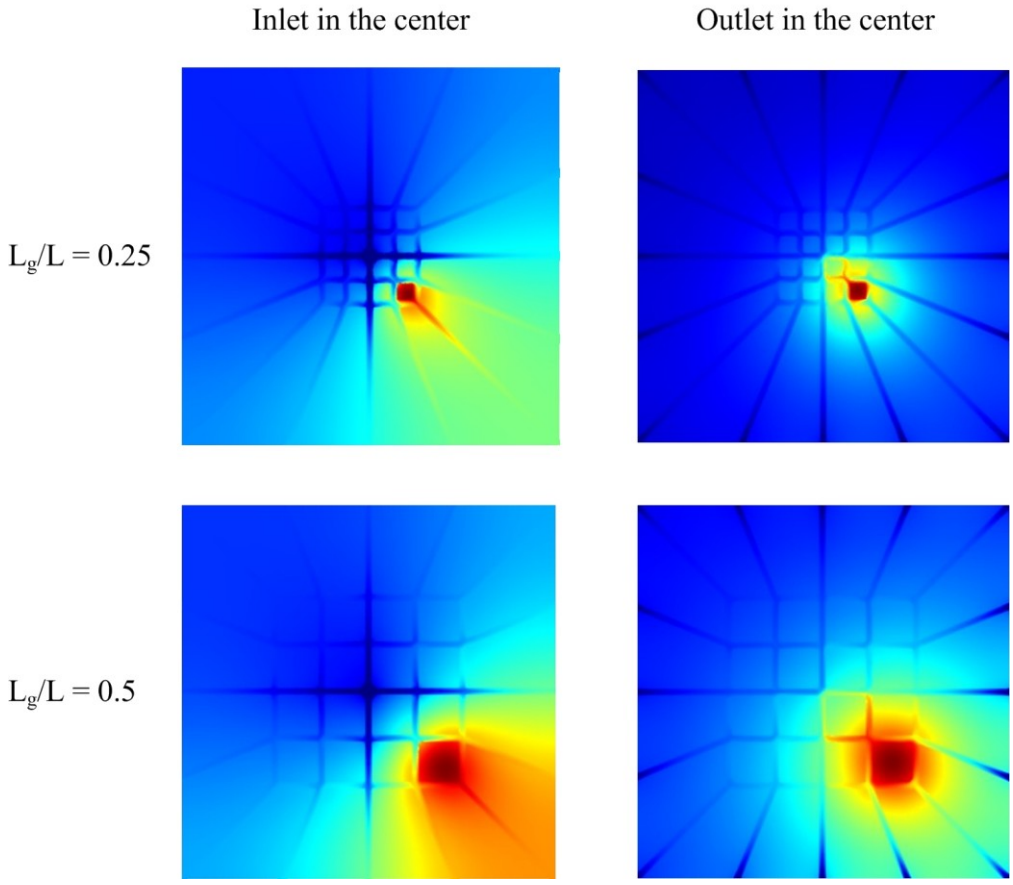

Figure 4.13: The temperature distribution in the mid plane of the square slab when the heat generation is concentrated in the lower right corner of the square grid and $P_{max} = 10^8$.

increases. However, increasing L_g/L has almost no effect on T_{peak} when $L_g/L > 0.375$. When the concentrated heating is located in the corner of the grid, T_{peak} increases as L_g/L increases. The T_{peak} value is the lowest with $L_g/L = 0.25$ when the concentrated heating is in the corner, and with $L_g/L = 0.625$ when the concentrated heating is in the center. In addition, when $L_g/L = 0.375$ the peak temperature becomes almost as low as the lowest peak temperature obtained when the concentrated heating is located in the center or in the corner, Fig. 4.14.

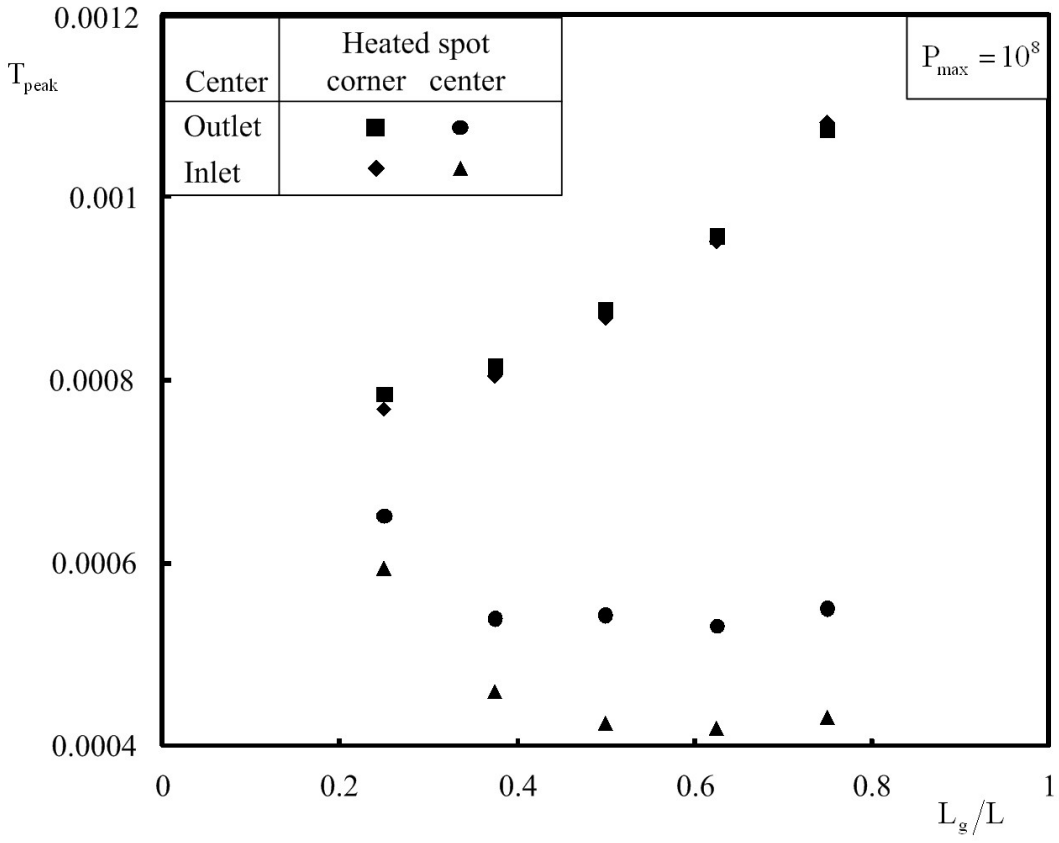

Figure 4.14: Peak temperature relative to L_g/L when the flow direction and the concentrated heat generation location change, $P_{max} = 10^8$.

4.5. Discussion

In this chapter we showed that a square slab can be cooled to an allowable peak temperature and can be strengthen by embedding in it a vascular cooling structure. The peak temperature and flow resistance are smaller in the radial configuration than in hybrid structures when other design parameters are fixed (size, pressure difference that drives the flow, the flow direction of the coolant). In addition, the peak stress is smaller in hybrid structures than in radial structures. The value of T_{peak} is smaller when the flow inlet is in the center. There is one L_g/L ratio for each V_r/V_g (when $V_r/V_g < 1$) that offers the lowest values of peak temperature and stress.

We also documented the performance of the hybrid design when the heating is concentrated in a small area. When the concentrated heating is located in the center T_{peak} decreases as L_g/L increases. On the other hand, when the concentrated heating is located in the corner T_{peak} decreases as L_g/L decreases. The peak temperature is smaller when the concentrated heating is closer to the center of the slab. When the concentrated heating is located in the center the applied heat flux decreases as L_g/L increases. Furthermore, when the concentrated heating is located in the center, the trade off between the decrease in heat flux and the decrease in the heat transfer area when L_g/L increases yields the results shown in Fig. 4.14.

We also found that by using a hybrid structure we can make the cooling process inside the grid part more robust. If one channel of the grid is damaged, the volume filled by the grid continues to be cooled because of the presence of loops. On the other hand, when a radial channel is damaged, the coolant does not flow through the damaged radial

channels. In sum, the grid & tree structures are more robust than purely dendritic structures.

5. Vascularization for cooling a plate heated by a randomly moving source

New technologies for compact high density functionalities require effective cooling capabilities. The cooling requirements are of two kinds: deterministic and random. The deterministic are due to heat sources that are known; for example, the heating caused by installed electronics in a package. Random cooling requirements are unsteady and highly diverse.

In this chapter, we focus on random cooling requirements, and document the heating of a plate by a randomly moving beam of energy. The plate is cooled by a vascular design of channels. The cooling structure is robust, yet the material performance could be endangered by the fact that the heat source is moving unpredictably. Maintaining the plate cool is the design challenge. We show that vascular structures are capable of bathing the entire volume, which is why they are being used for novel functionalities such as volumetric cooling and volumetric self-healing [38, 41-42, 56, 62-68]. Here we rely on vascular designs to control the heating effect of randomly varying and moving energy beams.

5.1 Model

Consider a square plate of width and length L, and with thickness of H = 0.1L. A structure of cooling channels is embedded in this plate to keep it under its maximum allowable temperature while the plate is heated with a concentrated and moving heat flux spot generated by an energy beam that intercepts the plate, Fig. 5.1. The length scale of the square footprint of the heating spot is 0.1L. The volume of the solid structure is fixed,

and so is the volume of the coolant fluid. The volume fraction of the fluid volume relative to the total volume is $\varphi = 0.05$. Coolant enters or exits from the center of the square slab while the pressure difference between the entrance and exit boundaries is fixed. The flow is incompressible with constant properties and it is time dependent. The governing equations for fluid flow are

$$\frac{\partial u}{\partial x} + \frac{\partial v}{\partial y} + \frac{\partial w}{\partial z} = 0 \tag{5.1}$$

$$\frac{\partial u}{\partial t} + u\frac{\partial u}{\partial x} + v\frac{\partial u}{\partial y} + w\frac{\partial u}{\partial z} = -\frac{1}{\rho}\frac{\partial P}{\partial x} + \nu\nabla^2 u \tag{5.2}$$

$$\frac{\partial v}{\partial t} + u\frac{\partial v}{\partial x} + v\frac{\partial v}{\partial y} + w\frac{\partial v}{\partial z} = -\frac{1}{\rho}\frac{\partial P}{\partial y} + \nu\nabla^2 v \tag{5.3}$$

$$\frac{\partial w}{\partial t} + u\frac{\partial w}{\partial x} + v\frac{\partial w}{\partial y} + w\frac{\partial w}{\partial z} = -\frac{1}{\rho}\frac{\partial P}{\partial z} + \nu\nabla^2 w \tag{5.4}$$

where $\nabla^2 = \partial^2/\partial x^2 + \partial^2/\partial y^2 + \partial^2/\partial z^2$; x, y and z are the spatial coordinates; u, v and w are the velocity components corresponding to the coordinates of x, y and z, respectively; P, ν, t and ρ are the pressure, kinematic viscosity, time and fluid density. The fluid is single phase with constant properties.

The temperature distribution is found by solving the energy equation in the fluid and solid domains,

$$\frac{\partial T}{\partial t} + u\frac{\partial T}{\partial x} + v\frac{\partial T}{\partial y} + w\frac{\partial T}{\partial z} = \frac{k_f}{\rho c_P}\nabla^2 T \tag{5.5}$$

$$\frac{\partial T}{\partial t} = \frac{k_s}{\rho_s c_{Ps}}\nabla^2 T \tag{5.6}$$

where c_P is the specific heat at constant pressure of the fluid, T is the temperature, the subscript s indicates the solid, and k_f and k_s are the fluid and solid thermal conductivities. The continuity of heat flux requires

$$k_s \frac{\partial T}{\partial n} = k_f \frac{\partial T}{\partial n} \tag{5.7}$$

where n is the vector normal to the fluid-solid interface. The preceding equations are nondimensionalized by using L as length scale, and constructing dimensionless velocities

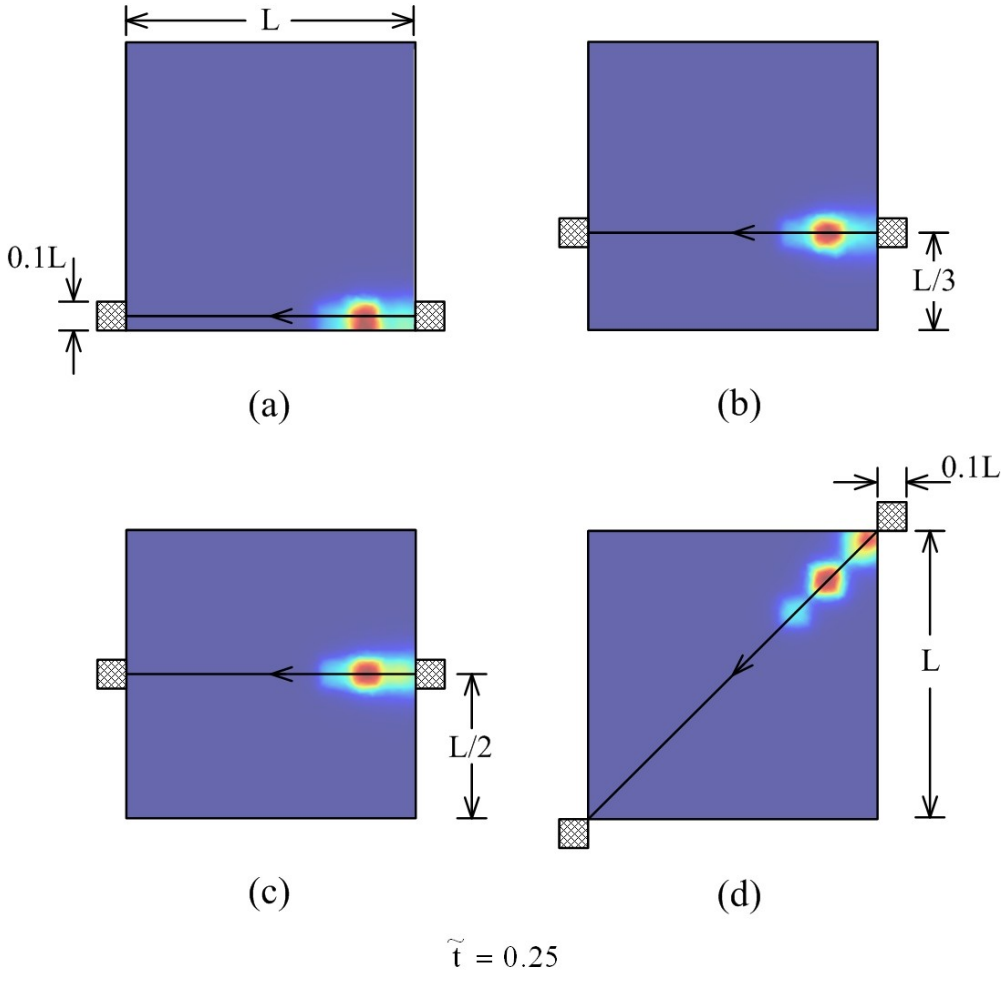

Figure 5.1: The paths of the moving beam and the temperature distribution on the bottom surface when $\tilde{t} = 0.25$.

as Reynolds numbers

$$(\tilde{x}, \tilde{y}, \tilde{z}, \tilde{n}) = \frac{(x, y, z, n)}{L}, \qquad \tilde{u} = \frac{uL}{\nu}, \qquad \tilde{v} = \frac{vL}{\nu}, \qquad \tilde{w} = \frac{wL}{\nu} \tag{5.8}$$

The dimensionless time and the dimensionless pressure difference are defined as

$$\tilde{t} = \frac{\nu t}{L^2}, \qquad \tilde{P} = \frac{(P - P_{out})L^2}{\mu\alpha} \tag{5.9}$$

where P, P_{out}, μ and α are the local pressure, the outlet pressure, the dynamic viscosity, and the thermal diffusivity of the fluid. The dimensionless temperature and continuity of the heat flux are indicated by

$$\tilde{T} = \frac{(T - T_{ref})k_f}{q''L} \tag{5.10}$$

$$\tilde{k}\left.\frac{\partial \tilde{T}}{\partial \tilde{n}}\right|_s = \left.\frac{\partial \tilde{T}}{\partial \tilde{n}}\right|_f \tag{5.11}$$

where T_{ref} and q'' are the fluid inlet temperature and the heat flux applied on the boundary, and $\tilde{k} = k_s / k_f$. The dimensionless mass conservation and momentum equations are

$$\frac{\partial \tilde{u}}{\partial \tilde{x}} + \frac{\partial \tilde{v}}{\partial \tilde{y}} + \frac{\partial \tilde{w}}{\partial \tilde{z}} = 0 \tag{5.12}$$

$$\frac{\partial \tilde{u}}{\partial \tilde{t}} + \tilde{u}\frac{\partial \tilde{u}}{\partial \tilde{x}} + \tilde{v}\frac{\partial \tilde{u}}{\partial \tilde{y}} + \tilde{w}\frac{\partial \tilde{u}}{\partial \tilde{z}} = -\frac{1}{Pr}\frac{\partial \tilde{P}}{\partial \tilde{x}} + \tilde{\nabla}^2\tilde{u} \tag{5.13}$$

$$\frac{\partial \tilde{v}}{\partial \tilde{t}} + \tilde{u}\frac{\partial \tilde{v}}{\partial \tilde{x}} + \tilde{v}\frac{\partial \tilde{v}}{\partial \tilde{y}} + \tilde{w}\frac{\partial \tilde{v}}{\partial \tilde{z}} = -\frac{1}{Pr}\frac{\partial \tilde{P}}{\partial \tilde{y}} + \tilde{\nabla}^2\tilde{v} \tag{5.14}$$

$$\frac{\partial \tilde{w}}{\partial \tilde{t}} + \tilde{u}\frac{\partial \tilde{w}}{\partial \tilde{x}} + \tilde{v}\frac{\partial \tilde{w}}{\partial \tilde{y}} + \tilde{w}\frac{\partial \tilde{w}}{\partial \tilde{z}} = -\frac{1}{Pr}\frac{\partial \tilde{P}}{\partial \tilde{z}} + \tilde{\nabla}^2\tilde{w} \tag{5.15}$$

where $\tilde{\nabla}^2 = \partial^2/\partial\tilde{x}^2 + \partial^2/\partial\tilde{y}^2 + \partial^2/\partial\tilde{z}^2$ and Pr is Prandtl number. The dimensionless energy equation for the fluid and solid domains are

$$\mathrm{Pr}\left(\frac{\partial\tilde{T}}{\partial\tilde{t}} + \tilde{u}\frac{\partial\tilde{T}}{\partial\tilde{x}} + \tilde{v}\frac{\partial\tilde{T}}{\partial\tilde{y}} + \tilde{w}\frac{\partial\tilde{T}}{\partial\tilde{z}}\right) = \tilde{\nabla}^2\tilde{T} \tag{5.16}$$

$$\mathrm{Pr}_s\frac{\partial\tilde{T}}{\partial\tilde{t}} = \tilde{\nabla}^2\tilde{T} \tag{5.17}$$

where Pr is the fluid Prandtl number, and Pr_s is defined as the kinematic viscosity of the fluid divided by the thermal diffusivity of the solid material. Boundary and initial conditions will be specified later case by case.

5.2 Radial channels

Consider the radial cooling channels of Fig. 5.2, where the diameters are d_1. The channels are connected to a main distribution channel of diameter d, which has a length L_d much smaller than L, namely $L_d = 0.06$ L. The relation between the d and d_1 is [15]

$$d = n_c^{1/3} d_1 \tag{5.18}$$

where n_c is the number of the channels of diameter d_1 connected to the channel of diameter d. The pressure difference between the inlet and outlet is nondimensionalized as [46, 47].

$$P_{max} = \frac{(P_{in} - P_{ref})L^2}{\mu\alpha} \tag{5.19}$$

The outlet pressure is $P_{ref} = 0$, while $P_{max} = 10^8$, which corresponds to laminar flow, i.e. the range Re < 2000. The surfaces between solid and fluid are impermeable

with no slip. The initial temperature of the plate and the fluid inside the cooling channels are T_{ref}. We set $\tilde{k} = 20, T_{ref} = 0$, q"= 1, Pr = 6 and Pr_s = 100. The heat flux spot caused by the moving beam enters from one edge and leaves from another edge as shown in Fig. 5.1. The swept length is 1.1 L when the length scale of the spot is 0.1 L. The beam sweeps the plate during the time $\tilde{t} = 1.1$ while its speed is V. The paths of the moving beam are shown in Fig. 5.1; (a) horizontal on the edge, (b) horizontal on $L/3$, (c) horizontal on $L/2$, and (d) diagonal. Figure 5.1 also shows the temperature distribution of the bottom surfaces at $\tilde{t} = 0.25$.

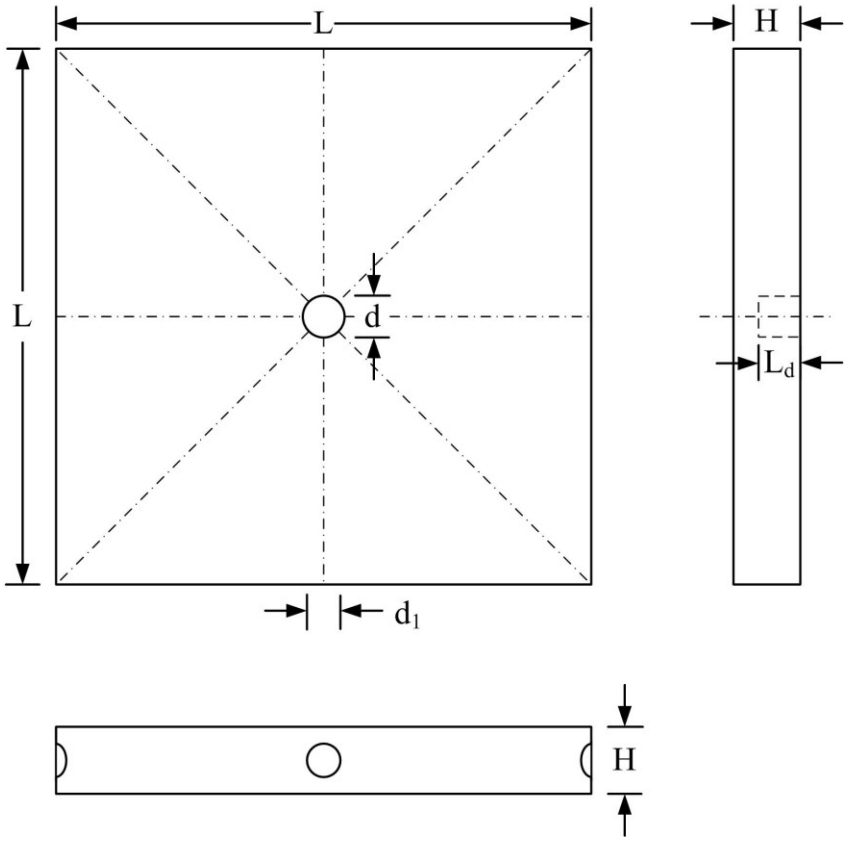

Figure 5.2: Radial cooling design on a square plate.

The dimensionless equations of section 5.2 were solved by using a finite element software [29]. The mesh of the domain was refined by increasing the number of mesh elements by 50% until the velocity field and the peak temperature solutions change by less than 1%, i.e. until the solution is mesh independent. The time step was also decreased in steps of 50% to discover whether the solution is affected by the selected time step: $\Delta t = 0.01$ was chosen because it does not affect the solution, and because it yields a data set accurate enough to see the fluctuations of the maximum allowable temperature.

Figure 5.3 shows how the maximum temperature varies in time. The inlet of the coolant was switched from the center (Fig. 5.3a) to the edge (Fig. 5.3b) to uncover how the fluid direction affects the maximum temperature in the square plate. The flow with inlet in the center provides a smaller $\widetilde{T}_{max}$ than the flow with the outlet in the center. For both flow directions, the moving path of Fig. 5.1a has the greatest $\widetilde{T}_{max}$ value.

The peak temperature is also affected by the size and the speed of the moving beam. Until now, the length scale of the square beam was set at $L_b = 0.1$ L, and the beam speed (V) was such that the beam sweeps the plate during $\widetilde{t} = 1.1$. Figures 4.4a-d show how the peak temperature changes as the length scale varies from 0.05 L to 0.2 L and beam speed varies from 0.5 V to 2 V while the path of the beam as in Fig. 4.1a. The peak temperature increases as the beam speed decreases, i.e. the sweeping time increases.

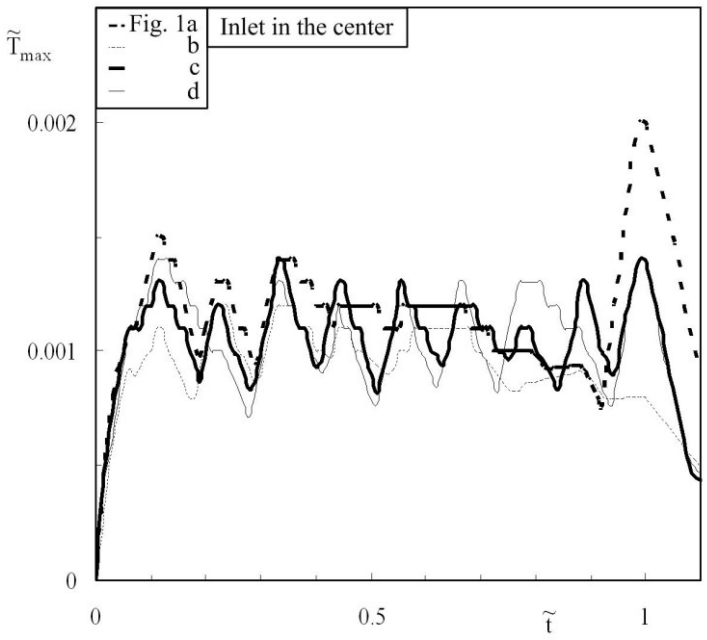

Figure 5.3a: The effect of flow direction on the peak temperatures, inlet in the center.

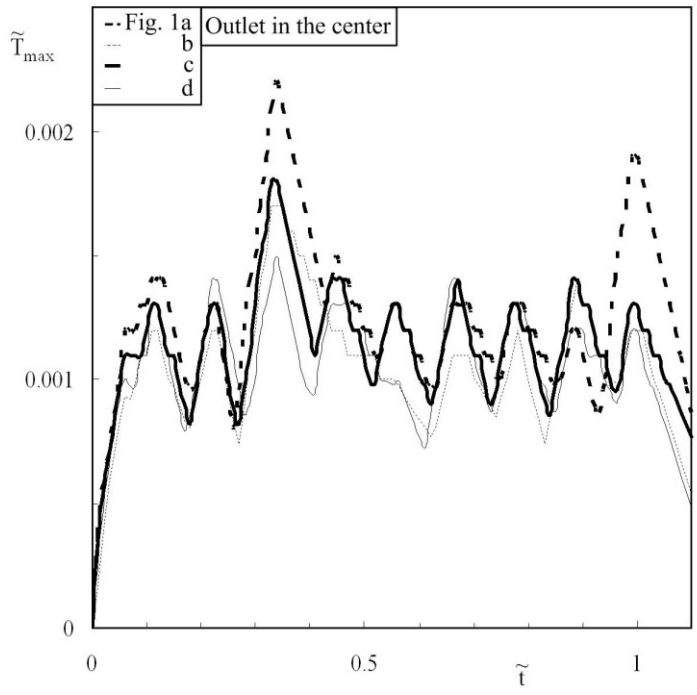

Figure 5.3b: The effect of flow direction on the peak temperatures, outlet in the center.

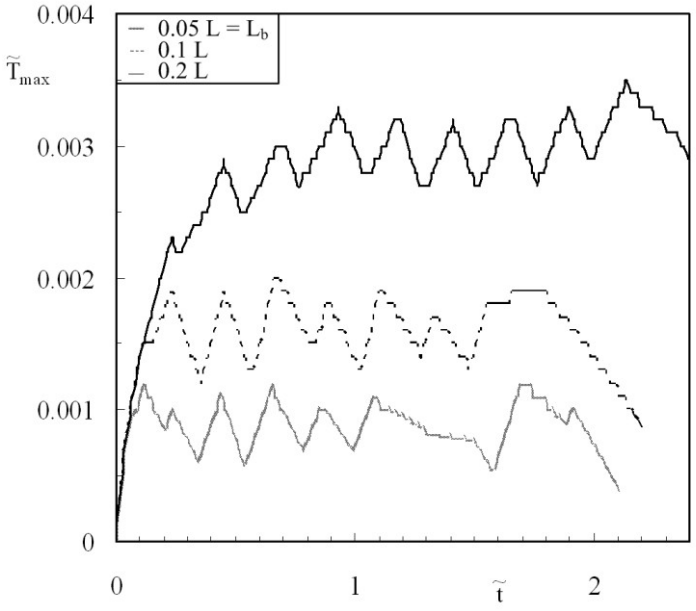

(a)

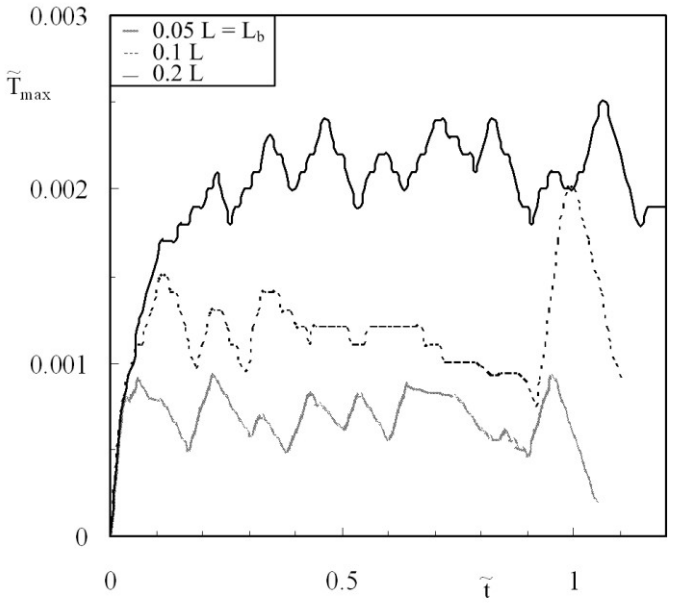

(b)

Figure 5.4a,b: The effect of beam size and speed on the peak temperatures. The inlet is in the center, and beam path is as in Fig. 5.1a. The speed of the beam is fixed and its length scale varies.

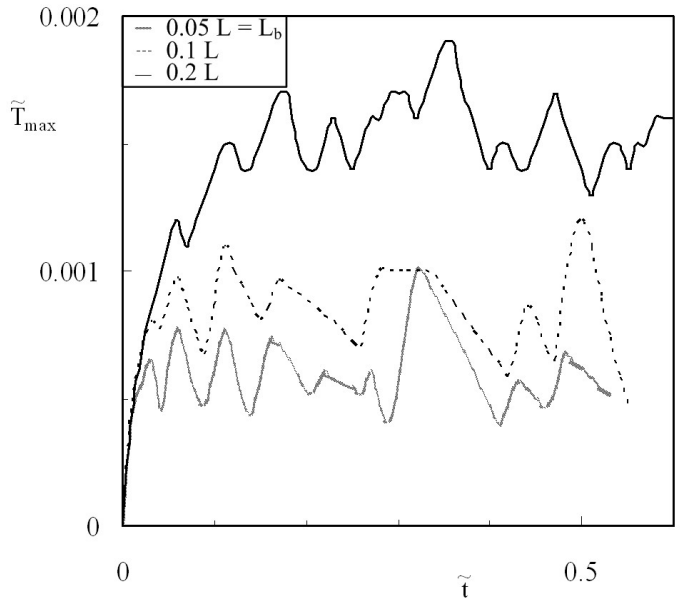

(c)

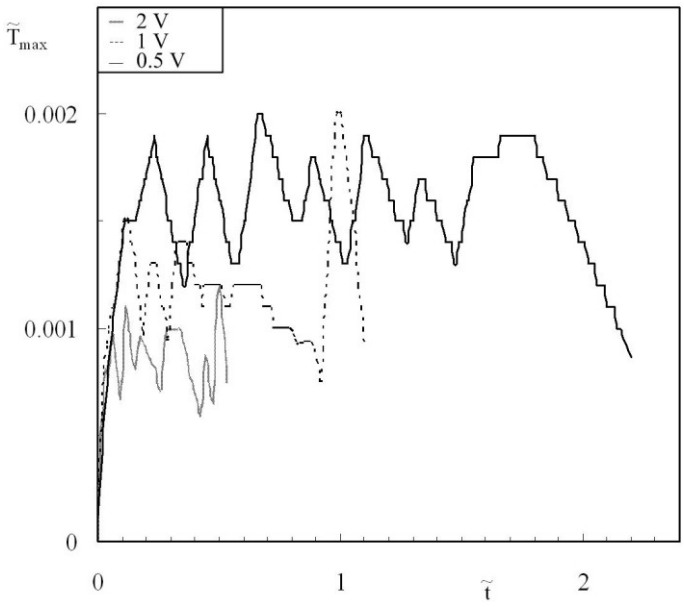

(d)

Figure 5.4c,d: The effect of beam size and speed on the peak temperatures. The inlet is in the center, and beam path is as in Fig. 4.1a. (c) The speed of the beam is fixed and its length scale varies and (d) The length scale of the beam is fixed and its speed varies.

Figure 5.4 also shows that increasing the size of the beam increases the peak temperature. However, the difference between the peak temperatures with the beam length scale of 0.05 and 0.1 is smaller than the difference between the peak temperatures with the beam length of 0.1 and 0.2 because the total heat transferred is proportional to the area of the beam, which is L_b^2.

5.3 One channel diameter versus one flow resistance

The d_1 channels presented in Fig. 5.2 do not have the same length because the outlet (or inlet) ports on the edge of the plate are equidistant. The flow resistances of two neighboring channels are not the same even though their diameters are the same. For this reason, instead of using the one diameter constraint we also studied radial designs where the flow resistance was the same in every channel. In the latter, the channel diameters where sized in proportion with their lengths raised to the power $1/4$ [15].

Figure 5.5 shows the evolution of $\tilde{T}_{max}$ versus $\tilde{t}$ for the constraints of uniform diameter (d_1) and uniform flow resistance when the inlet is in the center and the beam path is as in Fig 5.1a. The diameter of the main distribution duct (d) is the same in both designs. Uniform flow resistance provides a smaller $\tilde{T}_{max}$ than uniform diameter, Fig. 5.5. The difference between these two designs is small. Therefore, in the following results we used one diameter size for all the channels.

5.4 Grid versus radial channels

An alternative flow design is the grid of cooling channels shown in Fig. 4.6a. The grid design has 12 outlet ports and the length scale of one of the grids is L/4. The

volumes of the solid structure and the cooling fluid are fixed. The heating beam moves horizontally or diagonally as shown in Figs. 5.1a, d. The length scale of the moving square beam is 0.1 L and it sweeps the plate during the time $\tilde{t} = 1.1$. The coolant enters from the center. The grid design is compared with the radial configuration, Fig. 5.6b. The additional benefit that the grid design brings is its robustness [51]. Because the grid designs have loops, even when one cooling channel is damaged the entire volume

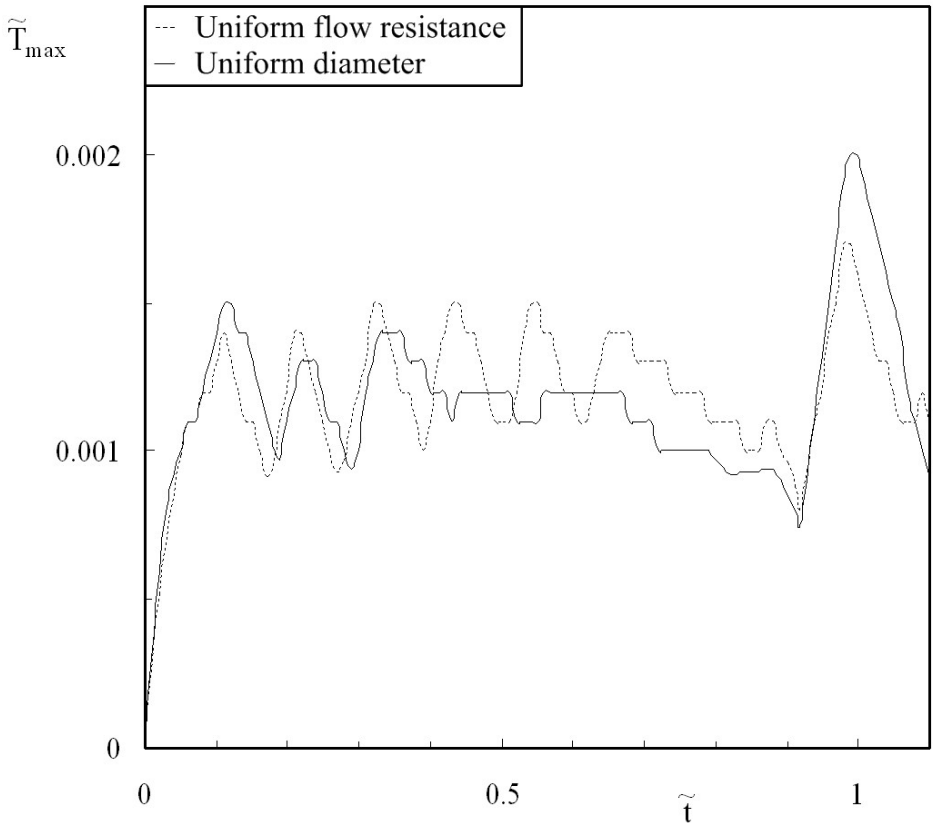

Figure 5.5: Peak temperatures when the flow direction is inlet in the center and beam path is as in Fig. 5.1a for uniform channel diameter and uniform flow resistance.

continues to be bathed by coolant. Grid designs are robust but their flow resistances are greater than in radial designs.

Figures 5.7a,b show how the peak temperature varies in the grid and radial designs of Fig. 5.6. The grid design provides a smaller $\widetilde{T}_{max}$ than the radial design when the beam moves horizontally. However, the radial design provides the smaller $\widetilde{T}_{max}$ when the beam moves diagonally.

The weakness of the designs of Figs. 5.6a,b is that there is no cooling channel along the diagonals of the plate. This weakness can be eliminated by adding four additional outlet ports near the corners of the plate while the fluid volume is constant. This is the hybrid design proposed in Fig. 5.8a.

Figure 5.9 shows the relation between the peak temperature and the dimensionless time when the cooling channel configurations are as in Figs. 5.8a, b and the beam path is as in Fig. 5.1a and 5.1d. The hybrid configuration performs almost the same as the radial configuration when the path is as in Fig. 5.1a, d. Furthermore, increasing the number of

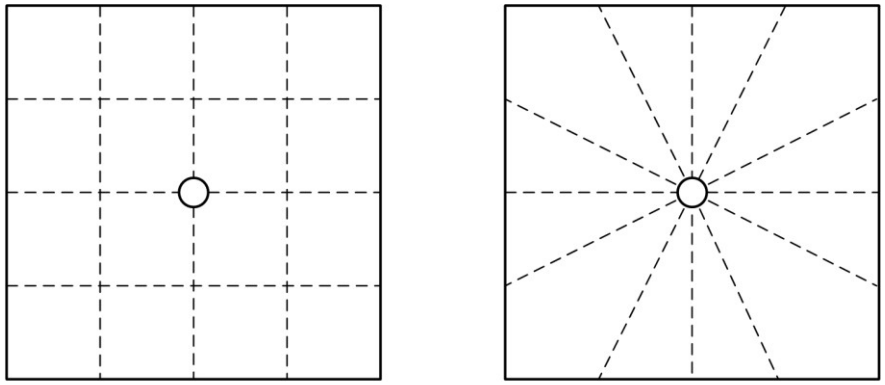

Figure 5.6: Grid and radial designs with 12 ports on the perimeter.

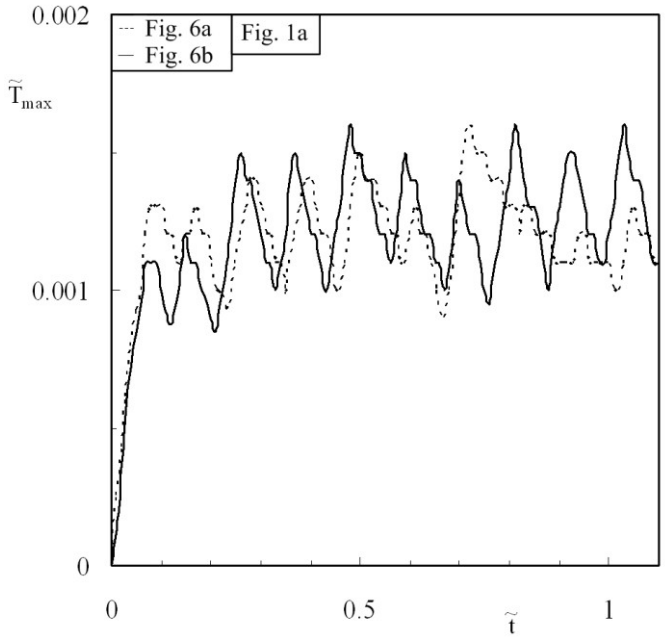

Figure 5.7a: Peak temperatures when the flow enters from the center in the configurations of Figs. 5.6a, b. The path of the beam is as in Fig. 5.1a.

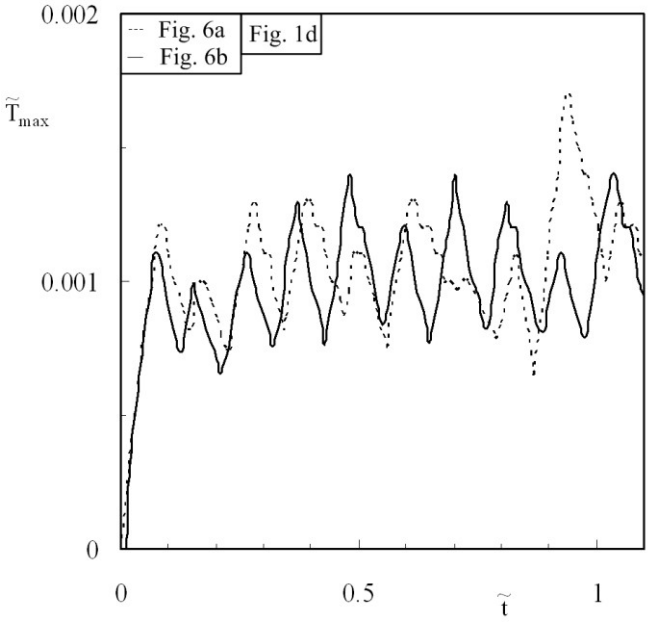

Figure 5.7b: Peak temperatures when the flow enters from the center in the configurations of Figs. 5.6a, b. The path of the beam is as in Fig. 5.1d.

the cooling channels from 12 to 16 does not change the order of magnitude of the peak temperature, cf. Figs. 5.7a, b and Fig. 5.9a, b.

Figure 5.10 shows how the imposed pressure difference affects the peak temperature in the designs of Figs. 4.8a, b and the beam path of Fig. 5.1a. Increasing the pressure difference from 10^7 to 10^9 does not change significantly the cooling performance of the radial design. However, increasing P_{max} from 10^7 to 10^8 decreases the peak temperature when the design is hybrid, as in Fig. 5.8a. Increasing P_{max} from 10^8 to 10^9 does not change the order of the peak temperature with the design of Fig. 5.8b. These results mean that when P_{max} is smaller than 10^8 for the hybrid design, the rate of the coolant. When P_{max} exceeds 10^8 the conduction mechanism in the solid domain becomes the dominant heat transfer mechanism. Therefore increasing P_{max} does not affect the order of the peak temperature.

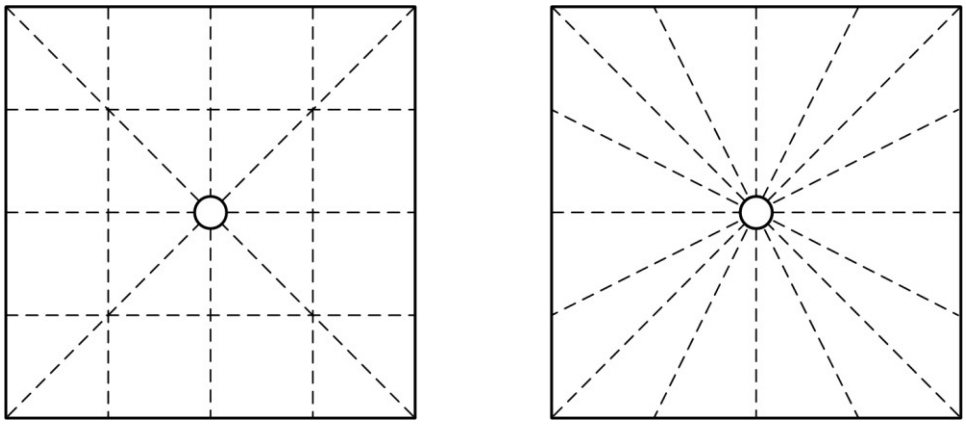

Figure 5.8: Designs with 16 ports on the perimeter: (a) hybrid; (b) radial.

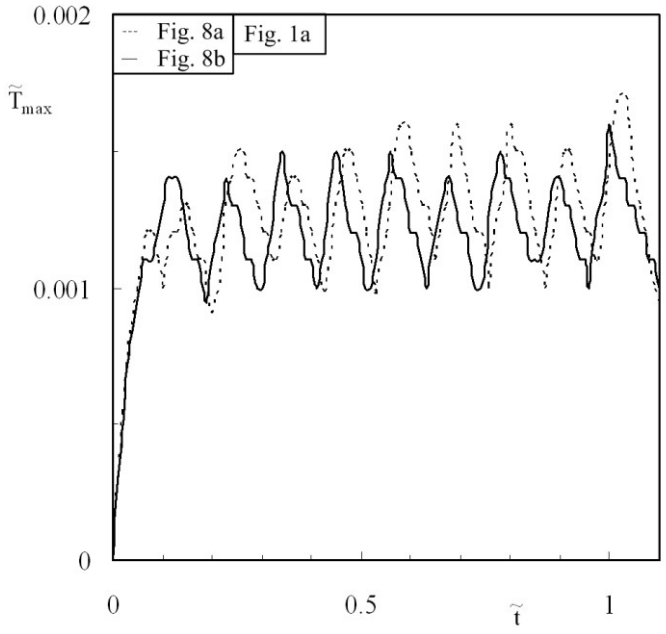

Figure 5.9a: Peak temperatures relative when the flow enters from the center in the configurations of Figs. 5.8a, b. The path of the beam is as in Fig. 5.1a.

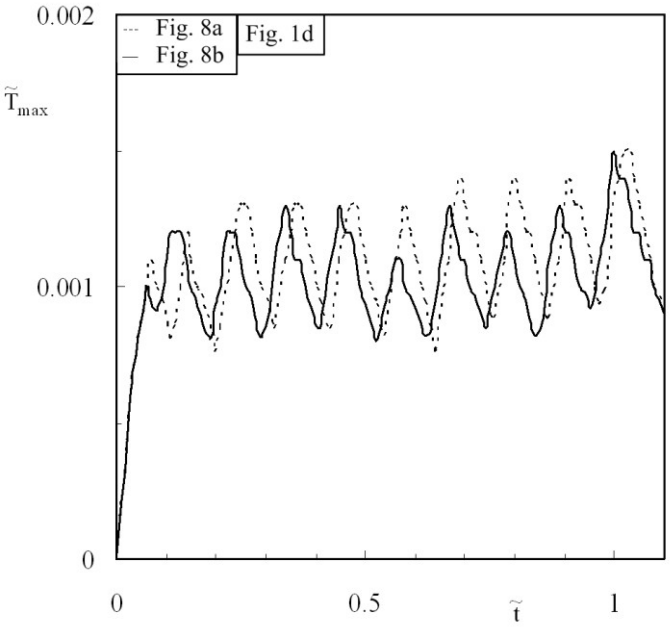

Figure 5.9b: Peak temperatures relative when the flow enters from the center in the configurations of Figs. 5.8a, b. The path of the beam is as in Fig. 5.1d.

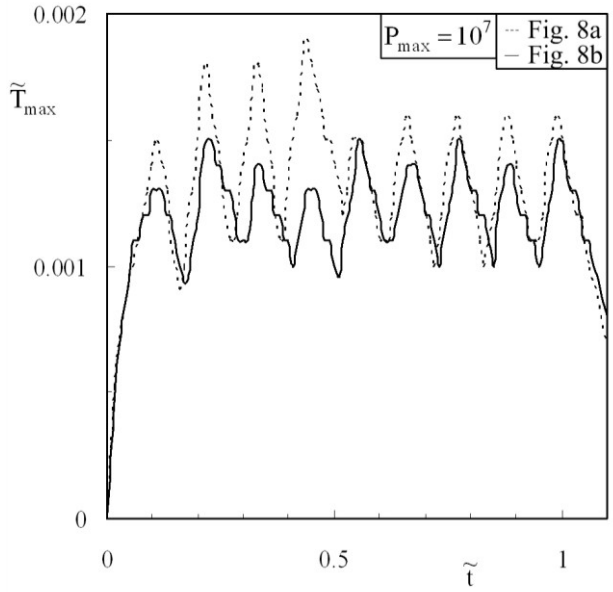

Figure 5.10a: Peak temperatures when the flow enters from the center in the configurations of Figs. 4.8a,b, and the path of the beam is as in Fig. 4.1a, $P_{max} = 10^7$.

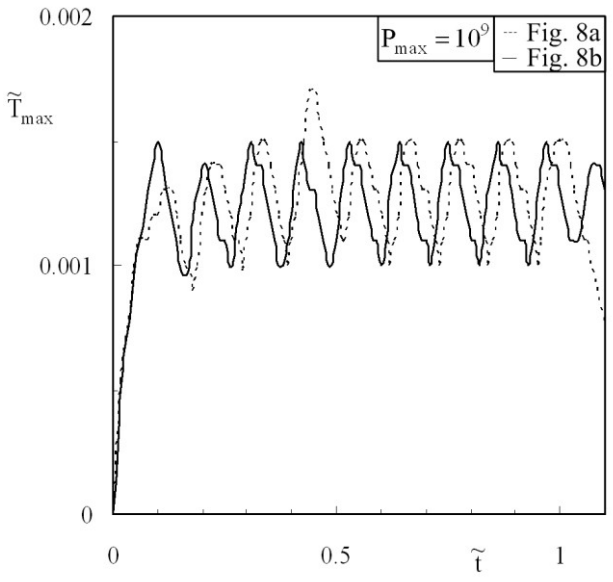

Figure 5.10b: Peak temperatures when the flow enters from the center in the configurations of Figs. 5.8a,b, and the path of the beam is as in Fig. 5.1a, $P_{max} = 10^9$.

5.5 Multiscale grid channels

Next, we considered a multiscale grid design of Fig. 5.11a, where there is an additional degree of freedom: the channel diameter ratio d_2/d_1. Varying this ratio shows that the order of magnitude of the peak temperature does not change for the beam paths of Figs. 5.1 a, d. However, at a specified time, every d_2/d_1 ratio provides a peak temperature smaller than the other d_2/d_1 ratios. The reason is that for a given d_2/d_1, some channels have smaller flow resistances than the other channels. Varying d_2/d_1 changes the flow resistance of all the channels, in such a way that the small flow resistance increases and the large resistances decrease. The objective is not only the design with the lowest overall resistance (greatest flow rate) but also the uniform distribution of flow resistance in all the channels. This second objective is especially important because the beam path is unknown, and the structure must be robust against this uncertainty.

Figure 5.12 shows a multiscale grid design with four channel diameters: d_1, d_2, d_3 and d_4. In this design, there are three degrees of freedom: d_1/d_2, d_2/d_3 and d_3/d_4. We varied each degree of freedom by fixing the other two, and as shown in Fig. 5.12 the grid design with $d_1/d_2 = 1.8$, $d_2/d_3 = 1$ and $d_3/d_4 = 1.1$ provides the greatest flow rate, $\tilde{Q}$. Figure 5.12c shows that $d_3/d_4 = 0.9$ is slightly better than $d_3/d_4 = 1.1$; however, when $d_3/d_4 = 0.9$ the channel flow rates are not as uniform as when $d_3/d_4 = 1.1$, and this makes $d_3/d_4 = 1.1$ more advantageous because it meets two objective at the same time.

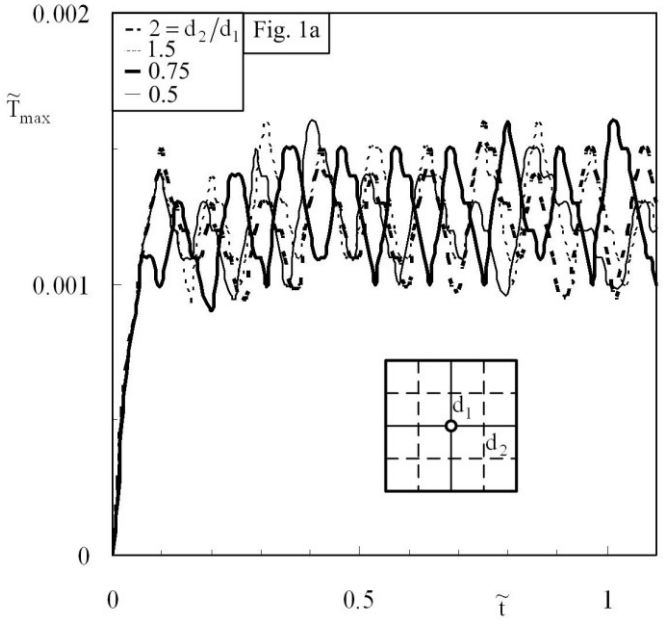

Figure 5.11a: Peak temperatures when the flow enters from the center for the multiscale grid design of Fig. 5.6a. The path of the beam is as in Fig. 5.1a.

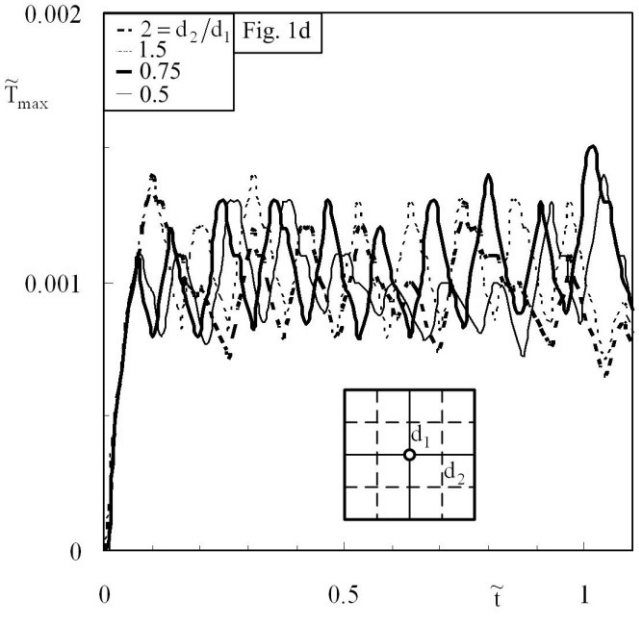

Figure 5.11b: Peak temperatures when the flow enters from the center for the multiscale grid design of Fig. 5.6a. The path of the beam is as in Fig. 5.1d.

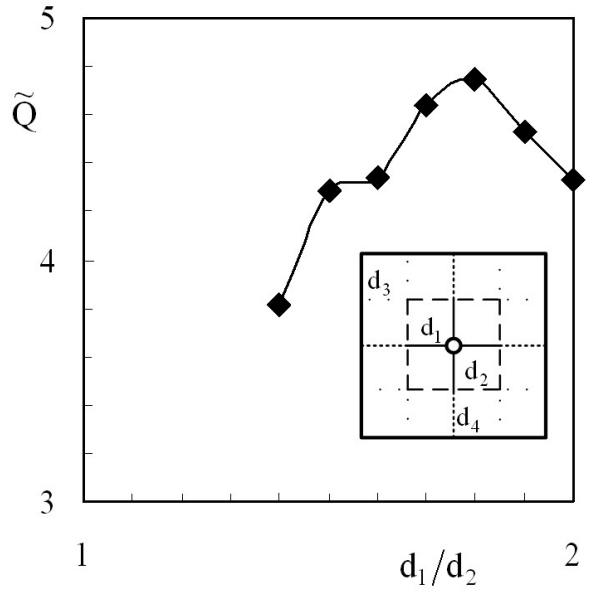

Figure 5.12a: The effect of diameter ratios on the dimensionless volumetric flow rate.

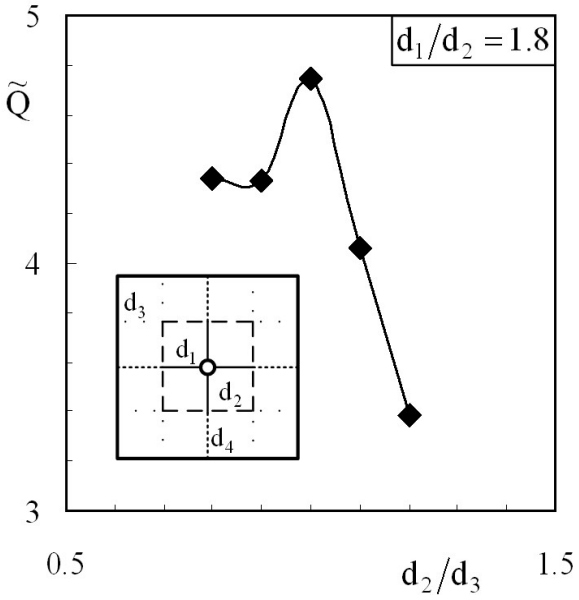

Figure 5.12b: The effect of diameter ratios on the dimensionless volumetric flow rate.

An alternative to determining the grid design with the highest flow rate is by using the Hess-Murray rule, Eq. (5.18). Consider the grid design of Fig. 5.12. The channels of diameter d_2 are connected to the channels of diameter d_3 and their numbers are the same, i.e. 8 for the grid design of Fig. 5.12a. Therefore, we can assume that the fluid inside one of the channels of diameter d_2 would be flowing through one of the channels of diameter d_3, i.e. one mother channel is connected to one daughter channel. Therefore $d_2/d_3 = 1$ and this ratio agrees with the result of Fig. 5.12b. Uniform distribution of flow resistance in all the channels exists for a specific d_3/d_4 ratio. The flow resistance of one channel of diameter d_4 should be equal to the sum of two flow resistances, namely the resistance of one channel of diameter d_2 and the resistance of one channel of diameter d_3. The flow resistance of a channel with laminar flow is [15]

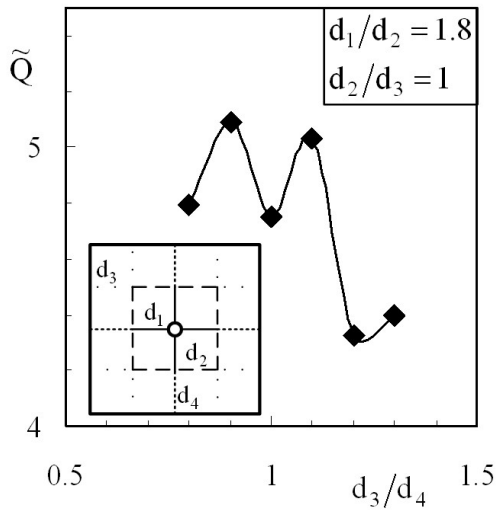

Figure 5.12c: The effect of diameter ratios on the dimensionless volumetric flow rate.

$$\frac{\Delta P}{\dot{m}} = C\frac{L}{D^4} \tag{5.20}$$

where L and D is the length and diameter of the channel and $C = 128\nu/\pi$ is the constant. By using Eq. (5.21) the flow resistances of the channels become

$$\frac{\Delta P_1}{C\dot{m}_1} = \frac{1}{d_2^4} + \frac{1}{d_3^4} \tag{5.21}$$

$$\frac{\Delta P_2}{C\dot{m}_2} = \frac{1}{d_4^4} \tag{5.22}$$

In addition, $\Delta P_1 = \Delta P_2$ and $d_2/d_3 = 1$ are known, and our objective is $\dot{m}_1 = \dot{m}_2$. By using these relations we find that $d_3/d_4 \cong 2^{1/4} \cong 1.18$, and this result is similar what is shown in Fig. 5.12c, $d_3/d_4 = 1.1$. Finally, one channel of diameter d_1 has three daughter channels: two d_2 channels and one d_4 channel. d_2/d_4 becomes 1.18 by using the optimized diameter ratios of d_3/d_4 and d_2/d_3. From Eq. (5.18), we find that $d_1/d_2 \cong 2.85^{1/3} \cong 1.42$. This ratio is 1.8 in Fig. 5.12a. The difference in the results of $d_1/d_2 \cong 1.42$ and Fig. 5.12a comes from the assumption of using the same diameter d in grid designs as in radial designs.

Figure 5.13 shows how the peak temperature varies in time when the cooling structure is a grid design with the optimized diameter ratios of Fig. 5.12. The temperature distribution in the plate is similar for the beam paths of Figs. 5.1a, d. Figure 5.14 shows the average peak temperature in four competing designs. The error bars indicate the maximum and minimum peak temperatures when the dimensionless time is greater than

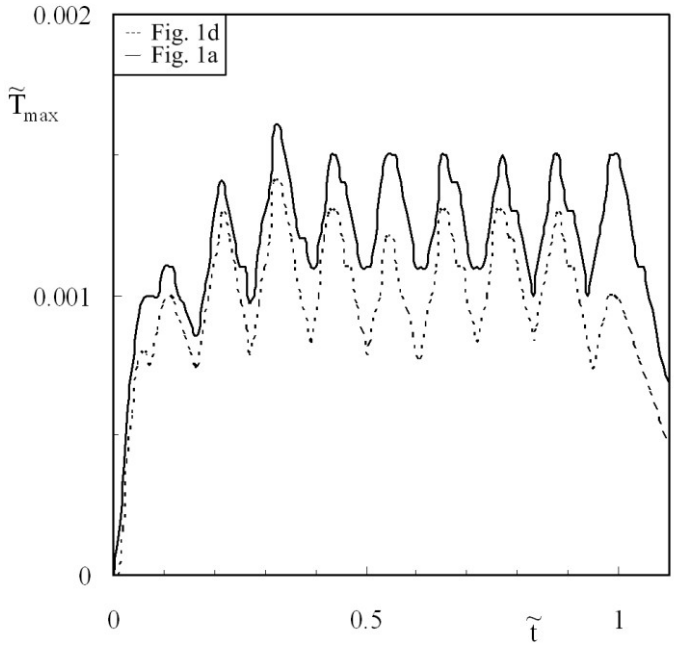

Figure 5.13: Peak temperatures in the grid design with the optimized diameter ratios of Fig. 5.12.

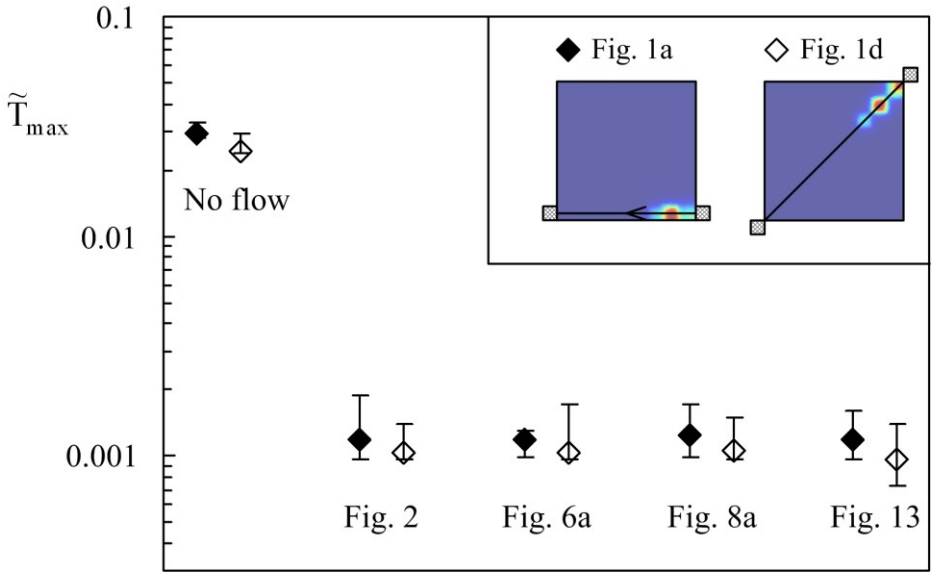

Figure 5.14: The average peak temperature in four competing designs. The path of the beam is: (a) Fig. 5.1a; (b) Fig. 5.1d. The error bars indicate the maximum and minimum peak temperatures when the dimensionless time is greater than 0.1, i.e. after the entire beam enters the plate surface.

0.1, i.e. after the entire beam enters the plate surface. The effect of changing from no cooling to vascular cooling is dramatic.

5.6 Discussion

In this chapter, we showed that a plate heated by a moving beam can be maintained under a desired temperature ceiling. We documented the peak temperatures for four different possible beam paths. The horizontal beam path when it is located on the edge of the plate provides the greatest peak temperature. Decreasing the velocity of the moving beam and increasing the size of the beam increase the peak temperature. We also showed that the assumption of uniform diameter leads to designs that are as good as the designs based on the assumption of uniform flow resistance, i.e. same flow rate in all the channels.

We documented the evolution of peak temperatures versus dimensionless time for radial designs and grid and hybrid designs. The grid and hybrid designs are robust because of the presence of loops. Unlike in radial designs, their cooling performance is not affected if one of the cooling channels is damaged [51]. We showed that the grid designs perform as well as the radial designs but they require greater pressure differences. The cooling performance of grid designs is better than the performance of radial designs when the beam moves horizontally. However, when the beam moves diagonally the peak temperature is smaller for radial designs. Because the grid and hybrid designs are robust, they are well suited for countering the effects of the unpredictable heat sources.

In addition, multiscale grid channels were studied and the diameter ratios that provide the greatest flow rate are documented. The peak temperature decreases dramatically changing from no cooling to vascular cooling.

6. Conclusions

The main conclusion of this dissertation is that the cooling performance and mechanical strength of a system which is heated and loaded with a distributed force can be increased by embedding vascular structures into it. The embedded vascular structure can be designed such that its cooling performance and mechanical strength is the greatest for the given conditions (i.e., boundary conditions, objectives and assumptions). However, there is no design that is optimal for all the conditions. This conclusion is in accord with the constructal law. The performance is the greatest when the design is the evolved design for the known time (i.e., given conditions). If the given conditions change, the design also should be changed to the new phase of the constructal design. The chapters 2, 3, 4 and 5 show that the design is not static (it is live, dynamic) and must be free to vary for the greatest performance throughout the life of the system.

Chapter 2 shows how the S curve history of spreading and collecting flows becomes steeper if the tree design is allowed to morph freely. In addition to the freedom of the design, the effect of varying the Peclet number, number of bifurcation levels, mother and daughter channel length ratio and the size of the domain are documented.

Chapter 3 shows that the cooling performance and mechanical strength of a circular plate which is heated and uniformly loaded with a distributed force can be increased with vascular channels embedded in it. The performance of radial channels and dendrites with one bifurcation level and dendrites with two bifurcation level structures is documented.

Chapter 4 shows that a square plate can be cooled and strengthened by embedding a vascular structure in it. The structure is a hybrid of grid and tree design. In addition to the uniform heating, the cooling performance of vascular structures is documented in the case of concentrated heating.

Chapter 5 shows that a plate heated by a randomly moving beam can be cooled under the allowable limit. The cooling performance of radial, grid and hybrid designs is documented. In addition, multiscale grid channels are introduced, and their performance is also documented.

The discussed vascular structures in this dissertation enable the capabilities required by the advanced technologies such as self-cooling and self-healing by simultaneously increasing the durability and robustness of the structure. These new discoveries in the design parameters of vascular structures will improve the performance and the lifespan of the systems work under great temperatures and loads such as turbine blades, nuclear cores and even the military and firefighter vehicles subjected to heating. The future improvement may include the increase in the robustness of the vascular structures by using a porous (permeable) structure instead of the solid (impermeable) section discussed in this dissertation. Usage of the porous structure should decrease the not bathed volume by the fluid in the case of one or more channels are damaged.

References

[1] A. Bejan, S. Lorente and K.-M. Wang, Networks of channels for self-healing composite materials, *J. Appl. Phys.*, Vol. 100 (2006) 033528.

[2] K.-M. Wang, S. Lorente and A. Bejan, Vascularized networks with two optimized channels sizes, *J. Phys. D: Appl. Phys.*, Vol. 39 (2006) pp. 3086–3096.

[3] S. Kim, S. Lorente and A. Bejan, Vascularized materials: tree-shaped flow architectures matched canopy to canopy, *J. Appl. Phys.*, Vol. 100 (2006) 063525.

[4] A.M. Aragon, R. Saksena, B.D. Kozola, P.H. Geubelle, K.T. Christiansen and S.R. White, Multi-physics optimization of three-dimensional microvascular polymeric components, *J. Computational Phys.*, Vol. 231 (2012) In press.

[5] S. Soghrati, P.R. Thakre, S.R. White, N.R. Sottos and P.H. Geubelle, Computational modeling and design of actively-cooled microvascular materials, *Int. J. Heat Mass Transfer*, Vol. 55 (2012) pp. 5309–5321.

[6] A. Bejan,Constructal-theory network of conducting paths for cooling a heat generating volume, *Int. J. Heat Mass Transfer*, Vol. 40 (1997) pp. 799–816.

[7] A. Bejan, *Advanced Engineering Thermodynamics*, Second Edition, Wiley, New York, 1997.

[8] A. Bejan, *Shape and Structure from Engineering to Nature*, Cambridge University Press, Cambridge,U.K., 2000.

[9] A.H. Reis, Constructal theory: from engineering to physics, and how flow systems develop shape and structure, *Appl. Mech. Review*, Vol. 59 (2006) pp. 269–282.

[10] G. Hernandez, J.K. Allen and F. Mistree, Platform design for customizable products as a problem of access in a geometric space, *Eng. Optimiz.*, Vol. 35 (2003) pp. 229–254.

[11] A.H. Reis, A.F. Miguel and M. Aydin, Constructal theory of flow architecture of the lungs, *J. Med. Phys.*, Vol. 31 (2004) pp. 1135–1140.

[12] A. Bejan and J.H. Marden, Unifying constructal theory for scale effects in running, swimming and flying, *J. Exp. Biol.*, Vol. 209 (2006) pp. 238–248.

[13] J.D. Charles and A. Bejan, The evolution of speed, size and shape in modern athletics, *J. Exp. Biol.*, Vol. 212 (2009) pp. 2419–2425.

[14] S. Lorente, E. Cetkin, T. Bello-Ochende, J.P. Meyer and A. Bejan, The constructal-law physics of why swimmers must spread their fingers and toes, *J. Theor. Biol.*, Vol. 308 (2012) pp. 141–146.

[15] A. Bejan and S. Lorente, *Design with Constructal Theory*, Wiley, Hoboken, 2008.

[16] R. Pearl, Growth of populations, *Q. Rev. Biol.*, Vol. 51 (1976) pp. 6–24.

[17] S.E. Kingsland, *Modeling Nature: Episodes in the History of Population Ecology*, University of Chicago Press, Chicago, 1995.

[18] M. Nishioka, C.K. Law, and T. Takeno, *Combust. Flame*, Vol. 104 (1996) pp. 328–342.

[19] J.W. Lu and P.W. Beamish, International diversification and firm performance: The S-CURVE hypothesis, *The Acad. Manage. J.*, Vol. 47 (2004) pp. 598–609.

[20] P. Asthana, Jumping the technology S-Curve, *IEEE Spectrum*, Vol. 32 (1995) pp. 49–54.

[21] A. Grubler, *The Rise and Fall of Infrastructures: Dynamics of Evolution and Technological Change in Transport*, Physica, Heidelberg, 1990.

[22] W. Easterly, *The White Man's Burden*, Penguin Books, London, 2006.

[23] M.K. Hubbert, Energy from fossil fuels, *Science*, Vol. 109 (1949) pp. 103–109.

[24] A.R. Brandt, Testing Hubbert, *Energy Policy*,Vol. 35 (2007) pp. 3074–3088.

[25] T.W. Patzek and G.D. Croft, A global coal production forecast with multi-Hubbert cycle analysis, *Energy*, Vol. 35 (2010) pp. 3109–3122.

[26] A. Bejan and S. Lorente, The constructal law origin of the logistics S curve, *J. Appl. Phys.*, Vol. 110 (2011) 024901.

[27] A. Bejan, Constructal-theory network of conducting paths for cooling a heat generating volume, *Int. J. Heat Mass Transfer*, Vol. 40 (1997) pp. 799–816.

[28] A. Bejan and S. Lorente, Constructal theory of generation of configuration in nature and engineering, *J. Appl. Phys.*, Vol. 100 (2006) 041301.

[29] See www.comsol.com for information about comsol multiphysics.

[30] A. Bejan, *Convection Heat Transfer*, Third Edition, Wiley, Hoboken, 2004.

[31] W. Wechsatol, J.C. Ordonez and S. Kosaraju, Constructal dendritic geometry and the existence of asymmetric bifurcation, *J. Appl. Phys.*, Vol. 100 (2006) 113514.

[32] X. Daguenet-Frick, J. Bonjour, and R. Revellin, Constructal microchannel network for flow boiling in a disc-shaped body, *IEEE Trans. Compon. Packag. Technol.*, Vol. 33 (2010) pp. 115–126.

[33] J. Fan, L. Wang, Constructal design of nanofluids, *Int. J. Heat Mass Transfer*, Vol. 53 (2010) pp. 4238–4247.

[34] S. Lorente, J. Lee, and A. Bejan, The "flow of stresses" concept: The analogy between mechanical strength and heat convection, *Int. J. Heat Mass Transfer*, Vol. 53 (2010) pp. 2963−2968.

[35] X.-Q. Wang, C. Yap, and A.S. Mujumdar, Laminar heat transfer in constructal microchannel networks with loops, *J. Electron. Pack.*, Vol. 128 (2006) pp. 273−280.

[36] J. Yue, R. Boichot, L. Luo, Y. Gonthier, G. Chen, and Q. Yuan, Flow distribution and mass transfer in a parallel microchannel contactor integrated with constructal distributors, *AIChE J.*, Vol. 56 (2010) pp. 298−317.

[37] L. Gosselin, Fitting the flow regime in the internal structure of heat transfer systems, *Int. Comm. Heat Mass Transfer*, Vol. 33 (2006) pp. 30−38.

[38] K.-H. Cho, J. Lee, H.S. Ahn, A. Bejan, and M.H. Kim, Fluid flow and heat transfer in vascularized cooling plates, *Int. J. Heat Mass Transfer*, Vol. 53 (2010) pp. 3607−3614.

[39] Y. Chen, C. Zhang, M. Shi, and Y. Yang, Thermal and hydrodynamic characteristics of constructal tree-shaped minichannel heat sink, *AIChE J.*, Vol. 56 (2010) pp. 2018−2029.

[40] A.K da Silva and L. Gosselin, Volumetric maximization of coolant usage in closed self-driven circuits, *Int. J. Heat Mass Transfer*, Vol. 53 (2010) pp. 3969−3976.

[41] B.D. Kozola, L.A. Shipton, V.K. Natrajan, K.T. Christensen, and S.R. White, Characterization of active cooling and flow distribution in microvascular polymers, *J. Intel. Mat. Sys. & Struct.*, Vol. 21 (2010) pp. 1147−1156.

[42] C.J. Hansen, W. Wu, K.S. Toohey, N.R. Sottos, S.R. White, and J.A. Lewis, Self-healing materials with interpenetrating microvascular networks, *Adv. Mater.*, Vol. 21 (2009) pp. 4143−4147.

[43] K.S. Toohey, N.R. Sottos, J.A. Lewis, J.F. Moore, and S.R. White, Self-healing materials with microvascular networks, *Nat. Mater.*, Vol. 6 (2007) pp. 581−585.

[44] S. Lorente and A. Bejan, Combined "flow and strength" geometric optimization: Internal structure in a vertical insulating wall with air cavities and prescribed strength, *Int. J. Heat Mass Transfer*, Vol. 45 (2002) pp. 3313−3320.

[45] L. Gosselin, A. Bejan, and S. Lorente, Combined 'heat flow and strength' optimization of geometry: mechanical structures most resistant to thermal attack, *Int. J. Heat Mass Transfer*, Vol. 47 (2004) pp. 3477−3489.

[46] S. Bhattacharje and W.L. Grosshandler, The formation of a wall jet near a high temperature wall under microgravity environment, *ASME HTD*, Vol. 96 (1988) pp. 711−716.

[47] S. Petrescu, Comments on the optimal spacing of parallel plates cooled by forced convection, *Int. J. Heat Mass Transfer*, Vol. 37 (1994) p. 1283.

[48] J.D. Anderson, *Fundamentals of Aerodynamics*, McGraw-Hill, New York, 2001.

[49] K.-M. Wang, S. Lorente, and A. Bejan, Vascularization with grids of channels: multiple scales, loops and body shapes, *J. Phys. D: Appl. Phys.*, Vol. 40 (2007) pp. 4740−4749.

[50] P. Xu, X.Q. Wang, A.S. Mujumdar, C. Yap, and B.M. Yu, Thermal characteristics of tree-shaped microchannel nets with/without loops, *Int. J. Therm. Sci.*, Vol. 48 (2009) pp. 2139−2147.

[51] W. Wechsatol, S. Lorente, and A. Bejan, Tree-shaped networks with loops, *Int. J. Heat Mass Transfer,* Vol. 48 (2005) pp. 573−583.

[52] L.A.O. Rocha, S. Lorente, and A. Bejan, Conduction tree networks with loops for cooling a heat generating volume, *Int. J. Heat Mass Transfer*, Vol. 49 (2006) pp. 2626−2635.

[53] A. Bejan, S. Lorente, and K.-M. Wang, Networks of channels for self-healing composite materials, *J. Appl. Phys.*, Vol. 100 (2006) 033528.

[54] H. Zhang, S. Lorente, and A. Bejan, Vascularization with line-to-line trees in counterflow heat exchange, *Int. J. Heat Mass Transfer*, Vol. 52 (2009) pp. 4327−4342.

[55] Y.S. Muzychka, Constructal design of forced convection cooled microchannel heat sinks and heat exchangers, *Int. J. Heat Mass Transfer*, Vol. 48 (2005) pp. 3119−3127.

[56] L.A.O. Rocha, S. Lorente, A. Bejan, Tree-shaped vascular wall designs for localized intense cooling, *Int. J. Heat Mass Transfer*, Vol. 52 (2009) pp. 4535−4544.

[57] Y. Chen and P. Cheng, Heat transfer and pressure drop in fractal tree-like microchannel nets, *Int. J. Heat Mass Transfer*, Vol. 45 (2002) pp. 2643−2648.

[58] Y.S. Muzychka, Constructal multi-scale design of compact micro-tube heat sinks and heat exchangers, *Int. J. Therm. Sci.*, Vol. 46 (2007) pp. 245−252.

[59] W. Wechsatol, S. Lorente, and A. Bejan, Dendritic heat convection on a disc, *Int. J. Heat Mass Transfer*, Vol. 46 (2003) pp. 4381−4391.

[60] C. Zhang, Y. Chen, R. Wu, and M. Shi, Flow boiling in constructal tree-shaped minichannel network, *Int. J. Heat Mass Transfer,* Vol. 54 (2011) pp. 202−209.

[61] A. Bejan, S. Lorente, and J. Lee, Unifying constructal theory of tree roots, canopies, and forests, *J. Theor. Biol.,* Vol. 254 (2008) pp. 529−540.

[62] S. Lorente and A.Bejan, Heterogeneous porous media as multiscale structures for maximum flow access, *J. Appl. Phys.* Vol. 100 (2006) 114909.

[63] A.H. Reis, A.F. Miguel, and A. Bejan, Constructal theory of particle agglomeration and design of air-cleaning devices, *J. Phys. D: Appl. Phys.*, Vol. 39 (2006) pp. 2311–2318.

[64] D. Lim, Y. Kamotani, B. Cho, J. Mazumder, and S. Takayama, Fabrication of microfluidic mixers and artificial vasculatures using a high-brightness diode-pumped Nd: YAG laser direct write method, *Lab Chip*, Vol. 3 (2003) pp. 318–323.

[65] K.H. Cho, and C.W. Choi, Hydraulic thermal performance of vascularized cooling plates with semi-circular cross-section, *Appl. Therm. Eng.*, Vol. 33-34 (2012) pp. 157–166.

[66] S. Kim, S. Lorente, and A. Bejan, Transient behavior of vascularized walls exposed to sudden heating, *Int. J. Therm. Sci.*, Vol. 48 (2009) pp. 2046–2052.

[67] K.M. Wang, S. Lorente, and A. Bejan, The transient response of vascular composites cooled with grids and radial channels, *Int. J. Heat Mass Trans.*, Vol. 52 (2009) pp. 4175–4183.

[68] E. Cetkin, S. Lorente, and A. Bejan, Hybrid grid and tree structures for cooling and mechanical strength, *J. Appl. Phys.*, Vol. 110 (2011) 064910.

Biography

Erdal Cetkin was born in 1985 in Kocaeli, Turkey. He received his BS degree from Kocaeli University in 2007, Turkey. After his graduation, he received a scholarship for graduate study abroad from Turkish Ministry of Education. Erdal Cetkin attended the English institute of the University of Alabama in 2008, and he received his MS degree from Duke University in 2010. His publications include:

1. E. Cetkin, S. Lorente, and A. Bejan, Natural constructal emergence of vascular design with turbulent flow, *J. Appl. Phys.*, Vol. 107 (2010) 114901.

2. E. Cetkin, S. Lorente, and A. Bejan, Vascularization for cooling and mechanical strength, *Int. J. Heat Mass Transfer*, Vol. 54 (2011) pp. 2774–2781.

3. E. Cetkin, S. Lorente, and A. Bejan, Hybrid grid and tree structures for cooling and mechanical strength, *J. Appl. Phys.*, Vol. 110 (2011) 064910.

4. E. Cetkin, S. Lorente, and A. Bejan, The steepest S curve of spreading and collecting flows: Discovering the invading tree, not assuming it, *J. Appl. Phys.*, Vol. 111 (2012) 114903.

5. E. Cetkin, S. Lorente, and A. Bejan, Vascularization for cooling a plate heated by a randomly moving source, *J. Appl. Phys.*, Vol. 112 (2012) 084906.

6. S. Lorente, E. Cetkin, T. Bello-Ochende, J.P. Meyer and A. Bejan, The constructal-law physics of why swimmers must spread their fingers and toes, *J. Theor. Biol.*, Vol. 308 (2012) pp. 141–146.